Evaluation of Eclipse© Monte Carlo dose calculation for clinical electron beams using heterogeneous phantoms

Gérard Lagmago Kamta

Master of Science

Medical Physics Unit

McGill University
Montréal, Québec, Canada
March, 2009

A thesis submitted to the Faculty of Graduate Studies and Research of McGill University in partial fulfillment of the requirements of the degree of Master of Science in Medical Radiation Physics

DEDICATION

To very special people in my life: my spouse **Edwige**, and my children **Laurence**, **Rostand** and **Jason**. Thank you for your patience and support during the past two years.

ACKNOWLEDGMENTS

I would like to express my gratitude to my supervisor Dr. Brigitte Reniers. I truly appreciate her continuous guidance and helpful advice on many aspects of this project.

I wish to thank Dr. Ervin Podgorsak for his teaching and support, and for providing me with the opportunity to study medical physics at McGill University.

I would also like acknowledge the support, patience and understanding of my collaborator and supervisor, Pr. André Dieter Bandrauk of the University of Sherbrooke, during my last two years as a medical physics student at McGill University.

I am also thankful to Dr. Slobodan Devic for his help with handling EBT Gafchromic© films, Michael Evans for his assistance with percent depth dose measurements, Dr. Wamied Abdel Rahman and Dr. Francois Deblois for their help with computer-related problems.

Many thanks to Emily Poon for her help with film calibration, and for allowing me to use her BrachyGUI program. I would like to acknowledge fruitful discussions with Dr. Christophe Furtoss, Krum Asiev, Magdalena Bazalova and Jurgen Last.

My gratitude also goes to all the instructors, staff, clinical physicists, engineers, radiation therapists and dosimetrists of the medical physics unit at the Montreal General Hospital for their teachings, help and smiles. Finally, I am thankful to all students of the McGill Medical Physics Unit for fruitful discussions and interactions.

ABSTRACT

Accurate dose calculations of photon and electron transport in tissue materials are an important step in the appropriate delivery of cancer radiotherapy. Various commercial treatment planning systems used in radiotherapy provide algorithms for fast dose calculations. It is the responsibility of medical physicists to commission and evaluates these algorithms. In this work, we have evaluated the electron Monte Carlo (MC) algorithm in Eclipse© using solid water phantoms with various tissue heterogeneities (water, lung, cortical bone, air) embedded, and using CT data from a real patient. For heterogeneous phantoms, the evaluation is done by comparing dose profiles and percent depth doses (PDDs) calculated on Eclipse with measurements, and with MC simulations using DOSXYZnrc©. Measurements of dose profiles and PDDs are taken using EBT Gafchromic© films, and we have developed a piece of software in Matlab© for extracting dose from EBT Gafchromic© films. For the real patient case, we use DOSXYZnrc© results as a benchmark against which Eclipse is evaluated. Although Eclipse© has been evaluated previously, the originality of the present work lays on the use of digitally reproduced phantom copies on Eclipse and DOSXYZnrc© instead of CT scanned phantoms, the use of absolute dose for all comparisons, and the consideration of a real clinical patient. In addition, we have developed a tool for extracting absolute dose profiles and PDDs from EBT Gafchromic© films. Our results indicate that, MC results agree in general better with measurements (within 5% or less) than Eclipse MC, whose discrepancies with measurements can be as high as 15% for physical phantoms used and as high as 10% in the case of real patient CT data. Largest discrepancies between measurement (or MC) and Eclipse© MC occur at depths near and below tissue heterogeneities with relatively sharp density gradients. The slightly better performance of Eclipse© for the real patient case is related to the smoother changes in heterogeneities densities in the human body as compared to sharp changes in our physical phantoms.

ABRÉGÉ

Les calculs précis de dose déposée dans les tissus par les photons et les électrons constituent une étape préliminaire cruciale dans tout approche de thérapie de cancer par la radiation. Plusieurs entreprises commerciales offrent de nos jours des programmes de planification des thérapies qui incluent des algorithmes de calcul de dose dans les tissus. Il est de la responsabilité du physicien médical de vérifier que ces algorithmes effectuent les calculs de dose avec une précision acceptables selon les standards actuels de radiothérapie. Dans ce mémoire, nous avons effectué une évaluation de l'algorithme Monte Carlo (MC) de calcul de dose (pour les faisceaux d'électrons) du programme de planification en radiothérapie connu sous le nom d'Eclipse©. Dans cette évaluation, nous avons utilisé des fantômes solides contenant des tissue de densités diverses (eau, poumon, os, air) ainsi que des images scanner d'un patient réel (humain). Pour les fantômes solides notre évaluation a été faite en comparant les calculs d'Eclipse© à des mesures expérimentales utilisant des films EBT Gafchromic© d'une part, et d'autre part à des calculs MC plus rigoureux utilisant DOSXYZnrc©. Pour le cas d'un patient, nous évaluons Eclipse© en le comparant aux résultats MC obtenu via DOSXYZnrc©, parce que nous ne pouvons placer un dosimètre à l'intérieur du patient. Nos résultats indiquent que les résultats MC sont plus proches des mesures expérimentales (écarts de l'ordre de 5% ou moins) que ceux d'Eclipse©, lesquels ont un écart pouvant atteindre a peu près 15% par rapport aux mesures dans le cas des fantômes et 10% par rapport aux résultats MC pour le cas du patient réel. Les pires imprécisions d'Eclipse© MC se retrouvent dans les tissus au voisinage des régions où il y a de fortes hetérogénéités et où les gradients de densités sont importants. En effet, les résultats obtenus par d'Eclipse© MC pour le cas d'un patient réel sont un peu meilleurs que ceux obtenus par les fantômes parce que les gradient de densités sont plus importants dans les fantômes utilises que dans le patient en question.

TABLE OF CONTENTS

LIST OF TABLES

LIST OF FIGURES

Chapter 1: Introduction and presentation

1.1 Generalities

Cancer or tumour is a malignant growth caused by an abnormal and uncontrolled cell division. Cancer expands locally by invasion and systemically by metastasis. The term “cancer” is used as a generic term for a group of more than 100 diseases that can affect any part of the body. Cancer has become a leading cause of death worldwide, as about 13% of all deaths in the world in 2005 are due to various types of cancer [1]. In Canada in particular, Cancer is second to cardiovascular disease as the leading cause of death [2], with an estimated 166,400 new cases and 73,800 deaths from cancer expected to occur in 2008 [3]. 40% of Canadian women and almost 45% of men will develop cancer during their lifetimes.

Surgery, chemotherapy and radiotherapy are the three main treatment modalities used for cancer therapy. Often, these modalities are combined for better patient outcome. Surgery refers to an invasive procedure by which the tumour is localized and removed by means of a surgical procedure. Chemotherapy involves the use of chemicals to kill cancer cells and is essentially used for non-localized cancers (i.e., tumours that could or have already spread to various parts of the body). In Radiotherapy (or radiation therapy), the cancer tumour is localized and treated with various types of radiation. The goal of radiotherapy is to give a high enough dose of radiation into the body to kill cancer cells while sparing the surrounding healthy tissue from damage. Radiotherapy is the cancer treatment modality in which the involvement of medical physicists is the heaviest.

1.2 Treatment modalities for external beam radiotherapy

Radiotherapy procedures can be grouped in two main categories: brachytherapy and external beam radiotherapy. In brachytherapy, the radiation source is placed

in close proximity to the target volume (intracavitary brachytherapy), or into the target volume (interstitial brachytherapy) or onto the target (surface mould radiotherapy). In external beam radiotherapy, the radiation source is placed at a certain distance from the patient to irradiate the target inside the patient. Most external beam radiotherapy is carried out with photons, only about 15% of patients receive electron beam therapy and a very small fraction is treated with more exotic particles such as protons, heavy ions or neutrons.

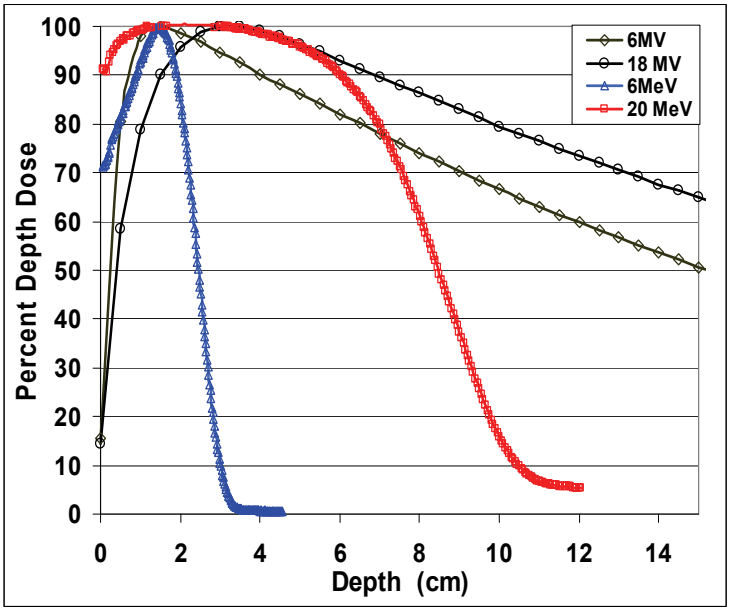

Figure 1.1: *Percent depth dose for photon (6 and 18 MV) and electron beams (6 and 20 MeV).*

Depending on the location and size of the tumour, either a photon beam or an electron beam, or a combination of both may be used for radiation therapy. The choice of either modality is essentially related to the way photons and electrons deposit energy or dose (i.e., energy per unit mass) in tissue. Figure 1.1 shows the *percent depth dose* (PDD) as a function of depth for various megavoltage photon and electron beams in a water phantom.

It appears from Figure 1.1 that photon beams have the following characteristics: *(i)* A relatively low surface dose (typically less than about 30%), which amounts

to a skin sparing effect that protects patient skin in megavoltage beam radiotherapy. *(ii)* A rapid raise of dose beyond the surface to reach a maximum at a depth z_{max}. The region between the surface and z_{max} is known as the *buildup region*. (iii) An exponential decrease of dose (beyond z_{max}) which is steeper when the beam energy is lower.

In contrast, the PDD for electron beams exhibits the following characteristics: *(1)* A rather high surface dose (typically larger than 75%); *(2)* A very small raise in dose from the surface to the depth of dose maximum z_{max}; *(3)* A very sharp fall of dose beyond R_{80} (the depth of 80% PDD beyond z_{max}). (4) A long tail of flat low dose (typically less than 5%) known as the *bremsstrahlung tail*, which is due to photons produced by bremsstrahlung in the Linac head components (collimators, scattering foil, etc), in the phantom and in the air. This means that electrons essentially have a range (that increases with energy) beyond which the energy deposited is very small, and a region of nearly flat dose distribution between the surface and R_{80}. Therefore, electrons offer distinctive advantages over photon beams in terms of dose uniformity in the target volume and in minimizing dose to deeper tissue.

It is clear from Figure 1.1 that photon beams are more penetrating as they deposit a much larger dose deeper in tissue than electron beams, and therefore must be used to treat deep seated tumours. Electron beams are used to treat tumours at shallower depths (typically less than 5 cm deep), with the characteristic drop in dose beyond R_{80} serving to protect healthy tissue beyond the tumour. Therefore, in practice the electron beam energy is selected such that R_{80} or R_{90} (the depth of 90% PDD beyond z_{max}) is at the distal edge of the tumour. The most clinically useful energy range for electrons is 6 to 20 MeV, which are principally used for the treatment of skin and lip cancers, for chest wall irradiation for breast cancer, for administering boost dose to nodes and for the treatment of head and neck cancers [4].

1.3 Relevance, purpose and main features of this thesis

Any adequate radiotherapy treatment planning requires a calculation engine that accurately predicts the dose distribution in the irradiated volume. Such engines require a set of data that are obtained in the commissioning process of the treatment machine (e.g., linear accelerator). Standard depth dose and profile charts used for commissioning linear accelerators (linacs) are measured in water, i.e., assuming a homogeneous unit density medium. In addition, given that the human body is made of 80% water, it is very tempting to perform dose calculations with the assumption that the human tissue is only water. Early dose calculation algorithms for photon and electron beams used that assumption.

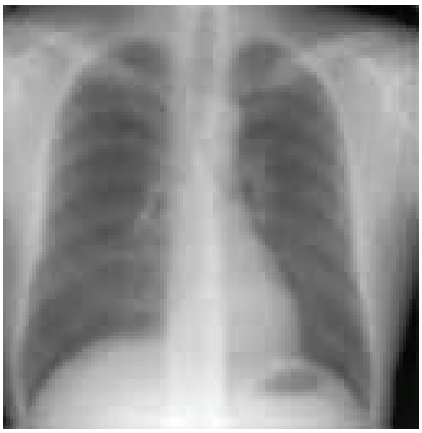

Figure 1.2: *Chest X-ray illustrating various tissue heterogeneities (e.g., bone, soft tissue, fat, …) in the patient. Source http://www.radiologyinfo.org/en/info.cfm?pg=chestrad&bhcp=1.*

In the patient however, as illustrated in the chest X-ray in Figure 1.2 the photon or electron beam may go through inhomogeneous tissue layers whose densities differ substantially from that of water, such as fat, bone, muscle, lung and air. The presence of these inhomogeneities (also known as heterogeneities) will produce changes in the dose distribution, depending on the quality of the radiation beam, and on the amount, size and type of material in the inhomogeneous volume. Therefore any adequate treatment planning system

must be based on an algorithm that accurately account for the effects of these heterogeneities.

The Monte Carlo (MC) simulation is currently the most accurate method for dose calculations in radiotherapy. It is believed that it will soon become the dominant dose calculations engine in radiotherapy treatment planning systems [5,6,7,8]. In fact there are already many general purpose MC codes such as for example EGS4 [9], PENELOPE [10] and EGSnrc [11], but they still cannot meet the main practical requirement imposed by clinical radiotherapy treatment planning, which is computation speed. Indeed, a full MC calculation in a realistic phantom using such a general purpose code with the required accuracy for radiotherapy is very time consuming, despite tremendous improvements in computer resources and algorithms in the past decades. This situation has lead to the development of the so-called fast MC codes [12,13,14,15]. In general, the efficiency gains of these fast MC codes originate from (i) a simplification of the basic MC transport to reduce the CPU time per simulated particle; (ii) variance reduction techniques or (iii) an investment in adding extra hardware for parallel applications. In most cases, the price paid for the increased efficiency is often a loss of some accuracy in the dose calculation.

For electron beam radiotherapy, which is the focus of this project, there are many fast MC commercial packages for radiotherapy treatment planning, among which the THERAPLAN PLUS© electron beam dose calculation module based on the Voxel-based Monte Carlo (VMC) [14] and the Varian Eclipse© treatment planning system (Varian, Palo Alto, CA) based on the Macro Monte Carlo (MMC) method [12]. Unfortunately, many clinics having these packages do not use them for routine planning of electron beam therapy, and “electron planning” is essentially limited to comparing the PDD and cutout size with the depth and size of the tumour. The main purpose of this project is to evaluate the Eclipse© treatment planning system for electron beams using phantoms with heterogeneities. This

evaluation is done by comparing dose calculations from Eclipse© with measurements, and with full MC calculations using DOSXYZnrc© [16], which is a general purpose Monte Carlo user code based on EGSnrc© [11]. In a previous similar approach [17], Ding *et al*. compared Eclipse Monte Carlo (eMC) calculations with phantom measurements. In their approach, they performed a computed tomography (CT) scanning of the physical phantom and imported the image into Eclipse© for calculations and reported relative dose results. Scanning the phantoms introduces some inaccuracies that originate form the conversion of Hounsfield units (HU) resulting from CT images into densities, as well as from CT artefacts and noise. Also, with sharp dose gradients in the dose distribution there is some sensitivity of dose profiles to the reference point chosen for reporting relative dose. The approach used in this thesis avoids scanning the phantom, instead we virtually reproduce each physical phantom in Eclipse© and in DOSXYZnrc© for calculations, thereby avoiding potential inaccuracies mentioned above. In addition, we report absolute doses instead of relative dose, which permit a direct comparison between measurements, Eclipse© and DOSXYZnrc© calculations.

1.4 Organization of the thesis

This thesis is organized as follows. In Chapter 2, we discuss the physics of the interaction of electron beams with matter. Chapter 3 is devoted to a brief description of the Macro Monte Carlo (MMC) [12] used in Eclipse© and of the full Monte Carlo used in DOSXYZnrc©. We present in Chapter 4 the protocol that we use to calibrate and extract dose from EBT Gafchromic films involved in our measurements. Results of our evaluation are presented and discussed in Chapter 5 for heterogeneous phantoms and in Chapter 6 for a real patient. A conclusion is given in Chapter 7. Short Matlab© programs for extracting dose profiles from EBT Gafchromic© films are presented in appendices A and B.

References

1. World Health Organization, *"Cancer"*, Fact Sheet, No. 297, February 2006 (http://www.who.int/mediacentre/factsheets/fs297/en/index.html).
2. Canadian Institute of Health Research (CIHR), *"Health Research – Investing in Canada's Future 2003-2004"*, 2006 (http://www.cihr-irsc.gc.ca/e/24939.html).
3. Canadian Cancer Society/National Cancer Institute of Canada, *"Canadian Cancer Statistics 2008"*, Toronto, Canada, 2008.
4. Khan, F.M., *"The Physics of radiation therapy"*, 3rd Ed., 2003, Lippincott Williams & Wilkins, Philadelphia.
5. Bielajew, A.F., *"Monte Carlo dose calculation: why gamble with anything else?" Proc. 1st Int. Workshop on EGS4,* 1997 (Tsukuba City, Japan: Laboratory for High Energy Physics) p310–323.
6. Ayyangar, K.M., and Jiang, S.B., *"Do we need Monte Carlo treatment planning for Linac based stereotactic radiosurgery? - a case study"*, Med. Dosim. 1998, Vol **23: p**161–167.
7. Ma, C.M., et al., *"Clinical implementation of a Monte Carlo treatment planning system" Med. Phys.* 1999, *Vol.* **26**: p2133–2143.
8. Ma, C.M. and Jiang S.B., *"Monte Carlo modeling of electron beams from medical accelerators"*, Phys. Med. Biol. 1999 **Vol. 4**: R157–89.
9. Nelson, W.R., Hirayama, H., and Rogers, D.W.O., *"The EGS4 code system Stanford Linear Accelerator Center Report"*, SLAC-265, Stanford, 1985.
10. Baró, J., et al., *"PENELOPE: an algorithm for Monte Carlo simulation of the penetration and energy loss of electrons and positrons in matter"*, Nucl. Instrum. Methods B, 1995, **vol. 100**, p31–46.
11. Kawrakow, I., *"Accurate condensed history Monte Carlo simulation of electron transport, I. EGSnrc, the new EGS4 version"*, Med. Phys., 2000, **Vol. 27, p**485–498.

12. Neuenschwander, H., Mackie, T.R., and Reckwerdt, P.J., *"MMC: a high performance Monte Carlo code for electron beam treatment planning"*, Phys. Med. Biol. 1995, **vol. 40, p**543–574.
13. Keall, P.J. and Hoban, P.W., *"Super-Monte Carlo: a 3D electron beam dose calculation algorithm"*, Med. Phys., 1996, **vol. 23**, p2023–2034.
14. Kawrakow, I., Fippel, M., and Friedrich, K., *"3D electron dose calculation using a voxel based Monte Carlo algorithm (VMC)"*, Med. Phys., 1996, **vol. 23**, p445–457.
15. Ma, C.M., et al., *"A Monte Carlo dose calculation tool for radiotherapy treatment planning"*, Phys. Med. Biol., 2002, **vol 47**, p1671-1689.
16. Walters, B., Kawrakow, I., and Rogers, D.W.O., "*DOSXYZnrc Users Manual*", National Research Council of Canada, 2007, Ottawa, 2007.
17. Ding, G.X., Duggan, D.M., Coffey, C.W., Shokrani, P., and Cygler, J.E., "*First macro Monte Carlo based commercial dose calculation module for electron beam treatment planning—new issues for clinical consideration*", 2006, Phys. Med. Biol., Vol. 51, p2781-2799.

Chapter 2: Physics and clinical aspects of electron beams

2.1 Introduction

This chapter is devoted to a brief discussion of the physics of electron beam interactions with a medium, as well as clinical features of electron beams used in radiotherapy. The production of clinical electron beams is the subject of Section 2.2. In Section 2.3, we discuss various Coulomb interaction processes between an electron travelling through a medium and atomic constituents (orbital electrons and nuclei) of the medium. The concepts of stopping power, electron scattering and dose are presented in Sections 2.4, 2.5, and 2.6 respectively. Some characteristics of clinical electron beams are given in Section 2.5.

2.2 Electron beam production

Electron beams have been used in radiotherapy since the early fifties and were initially produced by betatrons. Nowadays, most clinical electron beams are produced by linear accelerators (linacs) due to their numerous advantages [1] over betatrons, such as a full isocentric mounting, a quieter operation, a higher beam output, a larger field size and a more compact design. The clinically used energy range for electron beams is about 4 to 25 MeV. For such energies, electrostatic acceleration which is involved in kilovoltage and orthovoltage machines is no longer feasible, due to the large static fields required [2]. In linacs instead, cyclic acceleration (whereby an electron is repeatedly accelerated many time by a non-conservative force) based on microwave radiofrequency fields is used in the linac waveguide to accelerate electrons to MeV energies [1,2].

Electrons exit the evacuated beam transport system of the linac in the form of electron pulses with a narrow pencil beam shape, which has to be spread over the needed field size (up to 25 x 25 cm^2) used for in radiotherapy. This spreading

of the electron pencil beam is done by using either scattering or scanning. Pencil beam scattering is achieved by placing a thin foil (scattering foil) of high Z material (copper or lead) into the beam at the level of the flattening filter (used in the photon beam mode). Pencil beam scanning is usually implemented with two computer controlled magnets, which scan the pencil beam across the clinical treatment field by deflecting it in two orthogonal planes. Nowadays, beam scanning is considered unsafe and is no longer implemented in modern machines. Due to the high ability of electrons to scatter in air, special cones (applicators) are used to collimate and define the electron field at a typical distance of 5 cm above the target (i.e., the patient) surface.

2.3 Electron interactions with matter

As electrons travel through a medium, they pass in the vicinity of atoms in the medium with which they may interact, essentially via the Coulomb force (see Figure 2.1). In the clinical energy range, these interactions can be classified in following modes in terms of the relative importance of the impact parameter with respect to the radius of the atom [3]:

a) When the impact parameter b is significantly larger than the atomic radius a (i.e. $b >> a$), the incident electron interacts with the whole atom, an interaction referred to as *soft collisions*.

b) For an impact parameter b of the same order of magnitude as the atomic radius a, the incident electron may interact with orbital electrons of the medium, resulting in so-called hard collisions or catastrophic collisions.

c) When the impact parameter b is significantly smaller than the atomic radius a, the electron may interact with the nuclei, leading to bremsstrahlung radiation (radiative loss).

Therefore, an electron travelling in a medium looses energy as a result of collisional and radiative processes.

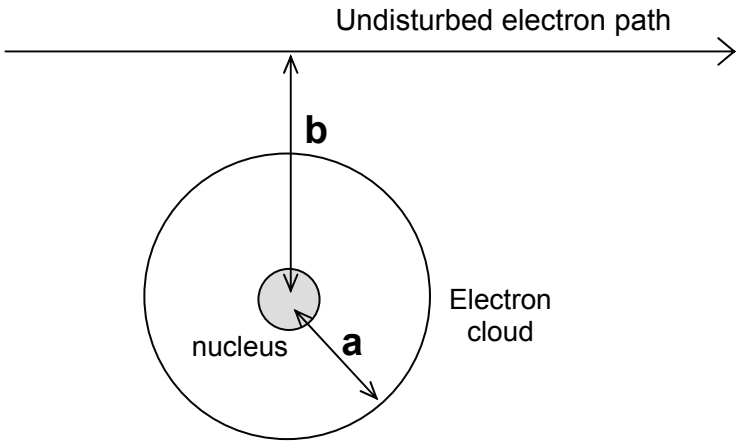

Figure 2.1: *Schematic representation the path of an electron incident on an atom, the impact parameter b and the atomic radius a.*

For interactions of the incoming electrons with individual constituents of atoms (electrons and nuclei) in the medium, the following processes can be identified:

(a) Elastic collisions with orbital electrons and with atomic nuclei, resulting in electron-electron and electron-nucleus scattering, respectively; both lead essentially to a change in the electron trajectory and no energy loss.

(b) Inelastic collisions with atomic electrons resulting in ionization and excitation of atoms, also known as collisional or ionization loss.

(c) Inelastic collisions with atomic nuclei, leading to the production of bremsstrahlung photons, also known as radiative loss.

The interaction of the electron with the nuclei results in most cases in elastic scattering, with little or no consequence for the energy loss of the electron but large consequences for the electron path. Only a fraction of electron-nuclei interactions lead to bremsstrahlung radiation (radiative loss), a process used for producing kilovoltage and megavoltage photon beams.

2.4 Stopping power for electrons

2.4.1 General aspects

The energy loss of a charged particle travelling in a medium is expressed in terms of a macroscopic quantity called *stopping power*. Stopping power is defined as the rate of energy loss of a charged particle per unit thickness of medium, i.e.,

$$S = \frac{dT}{dx},$$

where dT is the expectation value of the kinetic energy lost by the charged particle over a path length dx. The more convenient and widely used mass stopping power (S/ρ) is the ratio of the stopping power to the density of the medium ρ, i.e.,

$$\left(\frac{S}{\rho}\right) = \frac{1}{\rho}\frac{dT}{dx},$$

whose unit is MeV.cm^2/g. Since the collisional energy loss in its first step leads to energy deposition at the interaction point, while radiative energy losses often leads to energy carried away from the point of interaction, it is therefore logical to split the total stopping power into a collisional and a radiative component:

$$\frac{S_{tot}}{\rho} = \frac{S_{col}}{\rho} + \frac{S_{rad}}{\rho}, \tag{2.1}$$

where the mass collision stopping power S_{col}/ρ is due to energy transfers through collisions (soft and hard) and the radiative stopping power S_{rad}/ρ is due to energy lost through bremsstrahlung.

2.4.2 Collisional stopping power for electrons

Seltzer and Berger [4] derived the mass collision stopping power from the Bethe theory [5] for soft collisions and from the Moller differential cross section [6] for hard collisions. It can be written as [7]:

$$\frac{S_{col}}{\rho} = \frac{2\pi r_e^2 m_e c^2}{u}\frac{1}{\beta^2}\frac{Z}{A}\left[\ln\left(\frac{T}{I}\right)^2 + \ln\left(1+\frac{\tau}{2}\right) + F^{\pm}(\tau) - \delta\right], \tag{2.2}$$

where r_e is the classical electron radius, $m_e c^2$ the electron rest energy, u the atomic mass unit, $\beta = v/c$ the velocity of the incident electron in units of the speed of light c; these lead to $\frac{2\pi r_e^2 m_e c^2}{u} = 0.153536\ \text{MeV.cm}^2/\text{g}$. Z and A denote the atomic number and the atomic mass number of the absorber or the stopping medium, respectively. T is the kinetic energy of the incident electron and $\tau = T/(m_e c^2)$. I denotes the mean ionization-excitation potential of the absorber medium and corresponds to the average value of all ionization and excitation potentials of an atom in the absorber medium. In the first order, I increases linearly with Z, and is only dependent on the stopping medium and not on the type of particle imparting. The density effect correction δ accounts for the polarization of the stopping medium due to the passage of a fast ionizing particle, which leads to a decrease in the stopping power. δ is only important for dense media and not in gases, and increases with the kinetic energy of the incident electron. ICRU report 37 [7] contains extensive values of I and δ for materials of interest in radiotherapy. Finally, the $F^{\pm}$ expressions for incoming electrons are given by

$$F^{-}(\tau) = (1-\beta^2)\left[1 + \tau^2/8 - (2\tau+1)\ln 2\right], \tag{2.3}$$

and for incoming positrons by

$$F^{+}(\tau) = 2\ln 2 - (\beta^2/12)\left[23 + 14/(\tau+2) + 10/(\tau+2)^2 + 4/(\tau+2)^3\right]. \tag{2.4}$$

The collisional stopping power expression in Eq. (2.2) allows to make the following remarks [8,9]:

(a) S_{col} depends on the velocity of the incident electron via β and T.

(b) The factor Z/A makes the stopping power dependent on the electron density (i.e., the number of electrons per unit mass) of the absorbing medium. Z/A is 1 for hydrogen;0.5 for low Z absorbers and gradually drops to 0.4 for high Z absorbers.

(c) Since I increases almost linearly with increasing Z, the $-\ln I$ term decreases S_{col} with increasing Z.

2.4.3 Radiative stopping power for electrons

Any time a charged particle is decelerated it emits part of its kinetic energy in the form of Bremsstrahlung photons. This basic law of nature derived by Larmor is at the core of photon beams generation in medical physics by deceleration of electrons into a target. The mass radiative stopping power has been derived from the theory of Bethe and Heitler for light charged particles (electrons and positrons) and can be written as [10]:

$$\frac{S_{rad}}{\rho} = \alpha\, r_e^{\,2}\, \frac{N_A Z^2}{A}(T + m_e c^2) B_{rad}\,, \tag{2.5}$$

where $\alpha \approx 1/137$ is the fine structure constant, N_A is Avogadro's number. B_{rad} is a function of Z, T and $m_e c^2$ that ranges from 16/3 to 15 for energies up to 100 MeV. Other parameters are the same as in Eq. (2.2). Extensive tables for S_{rad} are available for a wide range of materials, as well as programs for generating them [11].

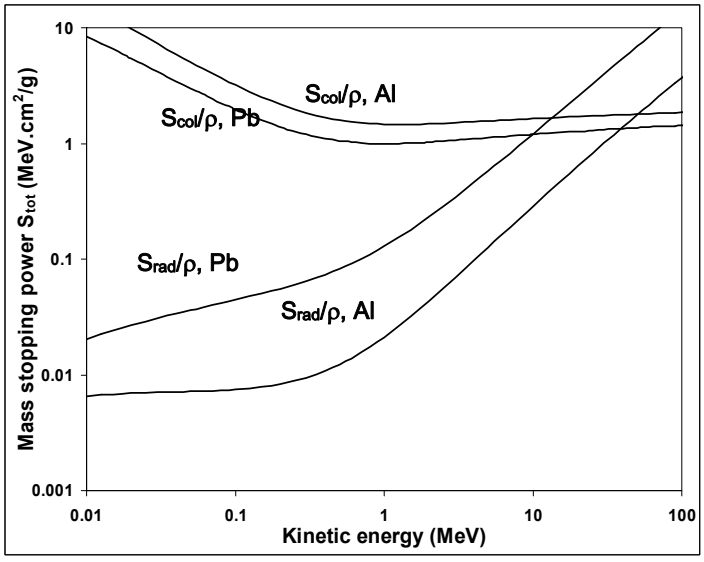

Figure 2.2: *Mass collisional* (S_{col}/ρ) *and mass radiative* (S_{rad}/ρ) *stopping power for Aluminium (Al) and lead (Pb) as a function of the kinetic energy of the incoming electron*.

It follows from Eq. (2.5) that the radiative stopping power is proportional to the atomic number of the absorber Z and to the total energy $T + m_e c^2$ of the incoming electron. This is clearly illustrated in Figure 2.2 where the mass radiative stopping for lead is larger than that of Aluminium, and both increase with the energies of the incoming electron. The mass collision stopping power, also shown in Figure 2.2, is smaller for higher Z elements (Pb) than lower Z element (Al) as discussed in Section 2.4.2.

In our investigation of the heterogeneity effects in this project, we use tissue materials such as "Solid water RMI 457", "Cortical Bone RMI 450" and "Lung LN 450", whose characteristics are described in Table 5.1 in Chapter 5. Using these characteristics, we have calculated the stopping power for these materials using the ESTAR program [11] from the NIST (National Institute of Standards and Technology), and plotted results in Figure 2.3. The total stopping power for these tissue materials in Figure 2.3 is highest for bone and lowest for lung tissue, with water in between. Note that in Figure 2.3 we have plotted the stopping power S_{tot} instead of $\frac{S_{tot}}{\rho}$, as the latter leads to nearly identical curves for the three tissue materials due to weighting by the density ρ.

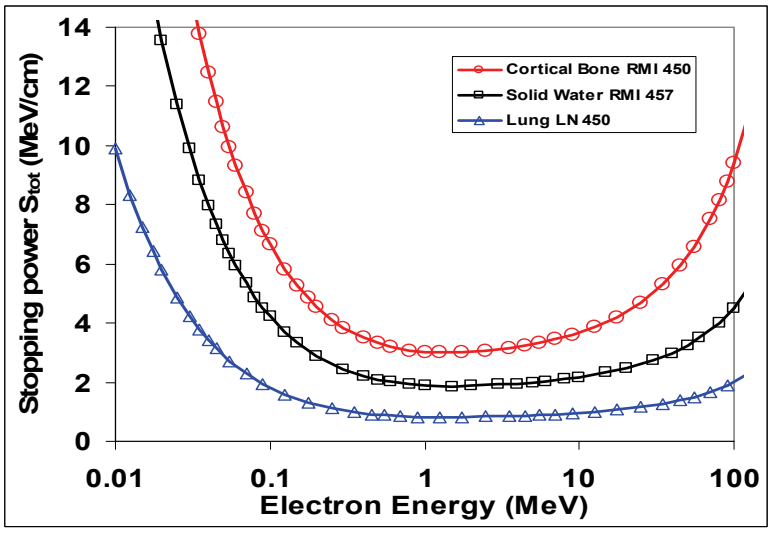

Figure 2.3: *Total stopping power $S_{tot} = S_{col} + S_{rad}$ for tissue materials to be used in this project (see Table 5.1 in Chapter 5) vs. incoming electron energy.*

2.5 Electron Scattering

As electrons pass through a medium, they suffer multiple scatterings due to Coulomb force interactions with orbital electrons and more predominantly with atomic nuclei. The angular deflections of electrons due to a large number of elastic Coulomb interactions can be modelled using multiple scattering theories such as the Molière theory [12,13,14] and the Goudsmit-Saunderson theory [15,16].

By analogy with mass stopping power, the ICRU (International Commission on Radiation Units and Measurements) [17] defines the mass angular scattering power of a material as the quantity $\frac{\overline{\theta}^2}{\rho\ell}$, where $\overline{\theta}^2$ is the mean square scattering angle by an absorber of thickness ℓ. Mass scattering powers for various materials and electron energies have been tabulated [18].

2.6 Dose to a medium

For the calculation of absorbed dose (the energy absorbed per unit mass) in a medium, one needs the electron fluence and the restricted stopping power. The restricted stopping power is involved when one is interested in the electron energy that is deposited locally, in the vicinity of the particle track. Indeed, if we wish to calculate the dose at a point or in a local region, energy transfers leading to energetic secondary particles that may carry away part of the energy imparted have to be excluded from the stopping power used for this dose calculation. The mass collision stopping power $L_{\Delta,col}/\rho$ that excludes energy transfers above a given energy threshold Δ is called *restricted mass collision stopping power*. The absorbed dose D is then given by

$$D = \int_{\Delta}^{T_0} \Phi_T(T) \left(\frac{L_{\Delta,col}}{\rho} \right) dT \,, \tag{2.6}$$

where T_0 is the kinetic energy of the incident electron, and $\Phi_T = \frac{d\Phi(T)}{dT}$ denotes the energy differential electron fluence spectrum, i.e., $\Phi(T)dT$ is the number of electron per unit area with energy between T and $T + dT$.

2.7 Characteristics of clinical electron beams

Due to the complexity of the electron spectrum, no single parameter can fully characterize the electron beam. Several parameters are used for this purpose, such as the most probable energy on the phantom surface $E_{p,0}$, the mean energy on the phantom surface $\overline{E}_0$, and the depth R_{50} at which the absorbed dose in water falls to 50% of the maximum dose. For water, $E_{p,0}$ and $\overline{E}_0$ are given by [3]

$$E_{p,0} = C_1 + C_2 R_p + C_3 R_p^2, \tag{2.7}$$

and

$$\overline{E}_0 = C_4 R_{50}, \tag{2.8}$$

respectively , where $C_1 = 0.22$ MeV, $C_2 = 1.98$ meV/cm^1, $C_2 = 0.0025$ meV/cm^2 and $C_4 = 2.33$ meV/cm.

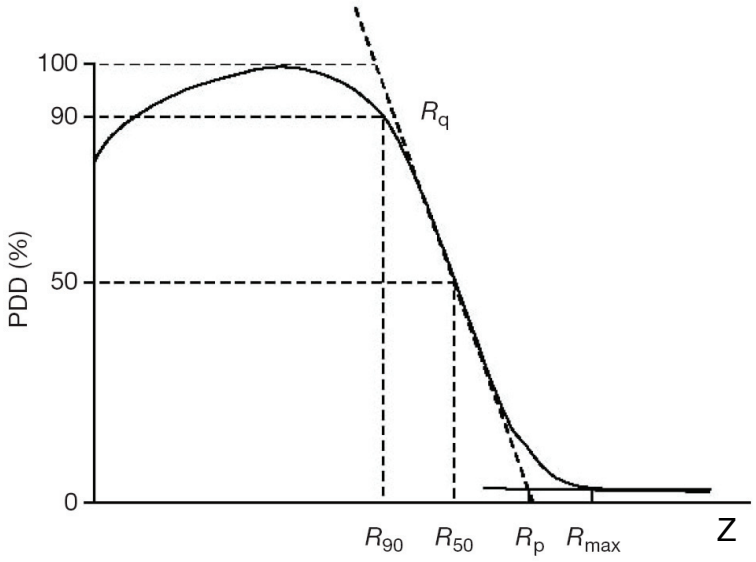

Figure 2.4: *Electron beam PDD curve illustrating R_p, R_q, R_{50}, R_{90}, and $R_{\max}$. Source: Ref. [3].*

All these characteristic parameters are expressed in terms of characteristic depths in the central axis percent depth dose (PDD) illustrated in Figure 2.4: R_q is defined as the depth at which the tangent through the dose inflection point intersects with the maximum dose level (i.e., 100%). R_{90} and R_{80} are the depths on the electron PDD curve beyond the depth of dose maximum z_{max} at which the dose falls to 90% and 80%, respectively. The practical range R_p is the depth on the electron PDD curve at which the tangent through the dose inflection point intersects with the extrapolation line of the bremsstrahlung tail. The maximum range $R_{\max}$ is the depth on the electron PDD curve at which the extrapolation of the dose curve meets the bremsstrahlung tail.

The PDD is a function of depth z, field size A, source to surface distance (SSD) f and beam energy E, and is defined as:

$$\mathrm{PDD}(z, A, f, E) = 100 \times \frac{D(z)}{D(z_{\max})}, \tag{2.9}$$

where $D(z)$ denotes the dose (or dose rate) at a point of depth z on the central axis of the beam, and $D(z_{\max})$ is the dose (or dose rate) on the central axis of the beam at the depth $z_{\max}$ where the PDD is maximum (100%). The central axis depth dose alone does not provide enough information to characterize the radiation distribution produced by the radiation beam in space. Dose distributions in 2D and 3D are determined by combining the central axis depth dose with off-axis ratios (OAR), which are measured perpendicularly to the beam central axis at a given depth (usually z_{max}) in the phantom. The off-axis ratio (OAR) is often defined as the ratio of dose at an off-axis point to the dose on the central axis of the beam at the same depth in the phantom. A plot of the OAR against the distance from the central axis is called a dose profile.

Examples of dose profiles in Figure 2.5 for a uniform phantom at specific depths show a relatively flat central region due to the uniformity of the phantom. The region of the dose profile where the dose changes rapidly is known as the *penumbra region*, which depends on field defining collimators, on the source size

and on the lateral electronic disequilibrium. The *umbra* is the region outside of the radiation field, far removed from the field edges, where dose is generally low and results from radiation transmitted through the linac head.

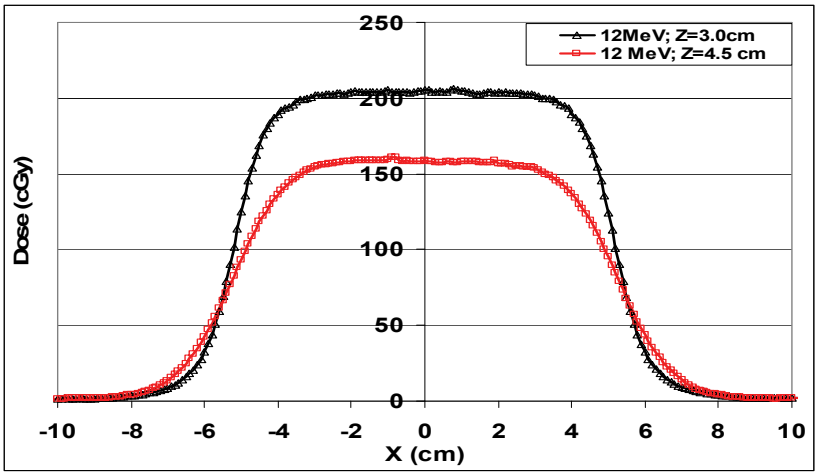

Figure 2.5: *Dose profiles (in cGy) for a 12 MeV electron beam measured (using EBT Gafchromic© film) at 3.0 cm and 4.5 cm depths in a solid water RMI-457 phantom with SSD=100 cm, and a 10x10 cm² applicator with a standard cutout. The number of monitor units given is 200 MU.*

References

1. Podgorsak, E.B., *"Treatment machines for external beam radiotherapy"* in *"Radiation Oncology Physics: a Handbook for teachers and Students"*, Ed. Podgorsak, E.B., IAEA (Vienna, 2005), p. 125-160.
2. Podgorsak, E.B., Metcalfe, P., and Van Dyk, J., *"Medical Accelerators"*, in *"The modern technology of radiation oncology: a compendium for medical physicists and radiation oncologists"*, edited by Van Dyk, J., Medical Physics Publishing (Madison, WI, 1999), p. 349-435.
3. Strydom, W., Parker, W., and Olivares, M., *"Electron means: physical and clinical aspects"*, in *"Radiation Oncology Physics: a Handbook for teachers and Students"*, Ed. Podgorsak, E.B., IAEA (Vienna, 2005), p. 273-299.

4. Seltzer, S.M., and Berger, M.J., *"Improved procedure for calculating the collision stopping power of elements and compounds for electrons and positrons"*, Int. J. of Appl. Radiation and Isotopes, 1984, **vol. 35**, p665.
5. Bethe, H.A., *"Scattering of electrons"*, Z. fur Physics, 1932, vol. 76, p. 293.
6. Moller, C., *" Zur Theorie des Durchgangs schneller Elektronen durch Materie"*, Ann. Phys., 1932, vol. 14, p. 531.
7. ICRU, *"Stopping Powers for Electrons and Positrons"*, 1984, Report No. **37**, Bethesda.
8. Seuntjens, J.P., *"Stopping power and range for electrons"*, Lecture notes in radiation Physics at McGill University, 2007, Private communication
9. Podgorsak, E.B., *"Radiation Physics for Medical Physicists",* 2006 (Springer-Verlag, New-York).
10. Attix, F.H., *"Introduction to Radiological Physics and Radiation Dosimetry"*, 1986 (John wiley & Sons, New-York)
11. ESTAR, *"Stopping powers and range tables for electrons"*, NIST, http://physics.nist.gov/PhysRefData/Star/Text/ESTAR.html.
12. Molière, G.Z., *"Theorie der Streuung Schneller geladener Teilchen. I. Einzelstreuung am abgeschirmten Coulomb-Field"*, Z. Naturforsch, 1947, Vol. 2a, p. 133-145.
13. Molière, G.Z., *"Theorie der Streuung Schneller geladener Teilchen. II. Mehrfachund Veilfachstreuung"*, Z. Naturforsch, 1948, Vol. 3a, p. 78-97.
14. Bielajew, A.F., *"Plural and multiple small-angle scattering from a screened Rutherford cross-Section"*, Nucl. Instr. Meth. Phys. Res. B, 1994, Vol. 86, p. 257-269.
15. Goudsmith, S., and Saunderson, J.L., "*Multiple scattering of electrons",* Phys. Rev., 1940, Vol. 57, p. 24.
16. Kawrakow, I., and Bielajew, A.F., *"On the representation of electron multiple elastic-scattering distributions for Monte Carlo Calculations"*, Nucl. Instr. Meth. Phys. Res. B, 1998, Vol. 134, p. 325-336.

17. ICRU, *"Radiation quantities and Units"*, Report No. **33**, 1980 (Washington, DC).
18. ICRU, *"Radiation dosimetry: electrons with initial energies between 1 and 50 MeV"*, Report No. **21**, 1972 (Washington, DC).

Chapter 3: Monte Carlo and Macro Monte Carlo

3.1. Introduction

The Monte Carlo (MC) method is the most accurate approach for calculation of radiation dose from clinical photon and electron beams, provided that the radiation source and phantom are accurately modeled and that a sufficiently large number of particle histories are simulated [1,2,3,4]. Among the many MC codes of general purpose that can be used for clinical dose calculations, the EGSnrc© (Electron Gamma Shower, National Research Council, Canada) code [5] is the most widely used. Both MC and Macro Monte Carlo (MMC) methods involved in this work are based on the EGSnrc code.

Besides systematic uncertainties due to approximate interaction cross sections, there is always a statistical uncertainty associated with results of MC calculations [6]. This statistical uncertainty is related to the number of particle histories simulated and to the size of the volume element (voxel) used, hence larger field sizes or finer resolutions require a correspondingly larger number of histories. Moreover, in order to avoid systematic resolution error near heterogeneity boundaries, smaller voxel size must be used to avoid dose averaging, and the relative energy loss per MC step should be small (typically a few per cent [7]) in order to avoid systematic sampling errors near heterogeneity boundaries. The consequence is a large number of transport steps, which leads to very long computation time required for MC simulations [7]. A MC dose distribution calculation for a typical clinical phantom would take many hours to complete, this long time is impractical for routine radiotherapy treatment planning in the clinic. This situation has lead to the development of so-called “fast Monte Carlo” methods that aim at reducing the computation time, while maintaining a reasonable accuracy for results.

In this Chapter, we briefly describe the traditional electron MC (eMC) algorithm in Section 3.2. In Section 3.3 we present the fast Electron Monte Carlo algorithm used for electron dose deposition in Eclipse© (Varian, Palo Alto, CA) treatment planning system.

3.2 Monte Carlo for high energy electron transport

3.2.1 Basics of Monte Carlo radiation transport

The basic equation that describes the transport of radiation in a medium is a coupled integro-differential equation that is very complex to solve analytically. Even deterministic numerical approaches are very cumbersome to implement. The MC technique is the only known solution method that can be applied for any energy range of interest. A MC simulation of radiation transport can generally be divided in three components or steps: (i) Initialization of the transport by selecting the type of particle (electrons, positrons and photons) to be transported, its energy, orientation, etc. The task here consists of modelling the radiation source adequately. (ii) Determination of how far the particle travels before interacting and which interaction takes place. This is done by sampling using random number generators (RNG) and known cross sections and probability distributions functions governing all possible interactions. It clearly appears that the success of MC simulations depends strongly on the availability of accurate interaction cross sections and probability distributions for photons, electrons and positrons. (iii) Keep track of or "score" the quantities of interest (energy deposition in our case). Here, quantities of interest are calculated by averaging over a given set of MC particle "histories" (also refereed to as "showers" or "cases" [5]).

More explicitly, step (ii) above involves a simulation of all possible individual particles interactions and tracks throughout the volume of interest, while properly accounting for the geometry of the volume. In this sense, a MC simulation of

particle transport is a faithful simulation of physical reality: particles are “born” according to distributions describing the source, they travel a certain distance without any interaction to a site where an interaction (collision and scatter) occurs. Knowing the physics (i.e. the probability distributions) governing all possible interactions as well as their cross-sections, RNGs are used to sample the distance travelled without interaction. Arriving at the interaction site the particle interacts, leading to a change in its energy and/or direction according to the corresponding differential cross section, possibly producing new particles that have to be transported as well. This procedure is continued until all particles are absorbed or leave the geometry under consideration.

Particle histories are independent from each other, which makes a multiprocessing of MC calculations straightforward and efficient. On the other hand, each particle history corresponds to a point in a multidimensional space whose dimensionality *d* depends on the number of interactions. Thus the above mentioned averaging procedure corresponds to a *d*-dimensional Monte Carlo integration. As such, the Monte Carlo estimate of quantities of interest is subject to a statistical uncertainty which depends on *N*, the number of particles simulated, and usually decreases as $N^{-1/2}$ [5,8]. Depending on the complexity and size of the geometry, and on the desired statistical accuracy, very long calculation times may be necessary.

3.2.2 The condensed history technique

The MC simulation of electron transport is more difficult (compared to photon transport) because in its slowing down process, a charged particle and the secondary particles it creates experiences millions of interactions with nuclei and orbital electrons of the surrounding medium before coming to rest. Due to this large number of interactions, an event by event simulation of electron transport would be extremely time-consuming because of limitations in computing

resources. The “condensed history” technique, developed by Berger [9] for the simulation of charged particle transport, permits to circumvent this difficulty by grouping many track segments (corresponding to soft events) of an electron real random walk into a single “step”, while catastrophic events such as bremsstrahlung are treated separately. This is implemented in EGSnrc in combination with multiple scattering theories [10,11,12]. The cumulative effects of the individual interactions during the step are taken into account by sampling the change of the particle’s energy, direction of motion, and position, from appropriate multiple scattering distributions at the end of the step. The condensed history technique, motivated by the fact that single collisions with the atoms usually cause only minor changes in the particle’s energy and direction of flight, made the MC simulation of charged particle transport possible

3.2.3 Geometry considerations in radiation transport

An important aspect in practical MC simulations is the handling of the geometry of the problem. In principle, this should be straightforward in any MC simulation since particle tracks can be broken into individual segments, each in a single material and region. As a geometric boundary is crossed, one needs to change cross-sections if the material changes, and one has the choice of either reselecting a new distance to travel in the new medium, or keeping track of how many mean free paths were traversed in the previous medium and converting the remaining mean free paths into the physical distance in the new medium using the new cross-sections. This choice comes about because once a particle has reached a given point, the probability of interacting in the new medium is independent of how far it travelled in the previous medium. Although a great strength of Monte Carlo is that the geometry and transport problems can be separated, handling the geometry can, in general, be very complex, but it is essentially book-keeping.

However, the presence of boundaries in a geometry can introduce a severe complication for electron transport simulations due to the implementation of condensed history technique. Although the individual steps of an electron are simulated as if they go in a straight line, this straight line represents the net effect of an ensemble of curved paths. Away from boundaries this approach can be very accurate, but near boundaries between media that differ substantially, the model breaks down because it does not account for contribution from the ensemble of paths which actually occurs in the second medium. This complex problem has been solved (and the solution implemented in the EGSnrc code) via the development of new multiple scattering theories and very complex algorithms for transporting electrons, including reverting to single scattering events near boundaries. [8]

3.2.4 The EGSnrc and the DOSXYZnrc applications

EGSnrc© is a general purpose package for MC simulations of coupled electron, positron and photon transport that employs the condensed history technique [5]. The particle transport uses steps of random length that can be implemented for any compound using cross-section tables for elements 1 through 100. The dynamic range goes from 1 keV up to few hundreds of GeV for charged particle kinetic energies, and from a 1 keV to several hundred of GeV for photon energies [5]. The following physics processes are taken into account in EGSnrc:

- for charged particles; bremsstrahlung production, positron annihilation at rest and in flight, Coulomb scattering from nuclei, electron-electron (Møller) and positron-electron (Bhabha) scatterings
- for photons: pair production, Compton scattering, Coherent (Rayleigh), photo-electric effect
- relaxation of excited atoms leading to fluorescent photons as well as Auger and Coster-Kronig electrons is also modelled.

DOSXYZnrc [13] is an EGSnrc© based MC simulation user code for 3-dimensional absorbed dose calculation in a volume with Cartesian geometry and scores the energy deposition in designated rectilinear voxels. Voxel dimensions are completely variable in all three directions, and every voxel can have different materials and/or varying densities. It is consequently the user code of choice for use with CT data. The user code allows radiation sources of various configurations such as mono-energetic diverging or parallel beams, as well as phase space data. DOSXYZnrc also incorporates a graphical user interface (GUI) which allows input files to be created and executed graphically. Volume geometries can be manually designed in DOSXYZnrc or come from CT images.

3.3 The Macro Monte Carlo (MMC) Method

Electron Monte Carlo (eMC) algorithm is a fast implementation of the MC method for the calculation of dose distributions for high energy radiotherapy electron beams on Eclipse©. The algorithm consists of the following two modules:

(a) An electron transport algorithm based on the Macro Monte Carlo (MMC) method [6].

(b) An electron beam phase space model known as the Initial phase Space (IPS) model describing electrons that emerge from the treatment head of the linear accelerator.

The maximal accuracy of the combined MMC and IPS is estimated to be about 3% of the dose maximum [14]. In this section, we only discuss the MMC method.

The MMC method is designed to speedup the transport of electrons through a 3D voxel type absorber geometry by reducing the number of explicit steps per particle history. This is achieved in two steps [6,14]: The first involves *local* calculations, where a MMC database of probability distribution functions (PDFs) is constructed and the absorber volume is pre-processed. In the second step, calculations are done in a *global* geometry and consist of electron transport

through the absorber in macroscopic steps based on these PDFs generated in local calculations.

3.3.1 The MMC probability distribution database

The MMC method uses spherical volume elements, often referred to as *spheres* or *kugels* (sphere in German) [6]. In addition to some data taken from Refs [17] and [18], the MMC database consists mostly of PDFs that describe the change in the phase space variables of electrons transported through spheres of various sizes and materials. These PDFs are generated in extensive pre-calculations using the EGSnrc code [5] to simulate the transport of vertically incident electrons of variable energies through macroscopic spheres of size and materials likely to be needed for the actual MMC simulation. If more than one electron emerges from a sphere, the electron with the highest energy is called the primary electron, and the others are the secondary electrons.

The geometry for the MMC pre-calculations is shown in Figure 3.1. Starting parameters are the radius r of the sphere, the chemical composition and density ρ of the material contained within the sphere, and incident kinetic energy T_i of the primary electron. The symmetry of the chosen geometry minimizes computer time for the pre-calculations and storage requirements of the resulting MMC database. For each primary electron, the MMC database contains pre-calculated PDFs for the exit position α, the direction θ, and the energy T_f of the emerging electron (see Figure 3.1). For each of these parameters, there is one PDF (in the MMC database) for any combination of

- 5 different materials: air (0.001205 g/cm^3), lung phantom LN4 (0.30 g/cm^3), water (1.00 g/cm^3), lucite (1.19 g/cm^3) and solid bone phantom SB3 (1.84 g/cm^3),
- 5 different sphere radii : 0.5, 1.0, 1., 2.0, 3.0 mm,

- 30 incident energy values T_i: 0.2, 0.4, 0.6, 0.8, 1.0, 1.5, 2, 3, 4, …, 22, 23, 24, 25 MeV.

For secondary particles (electrons and photons), only the average energy released to these particles per primary electron is stored as a function of the incident primary electron energy T_i in the MMC database.

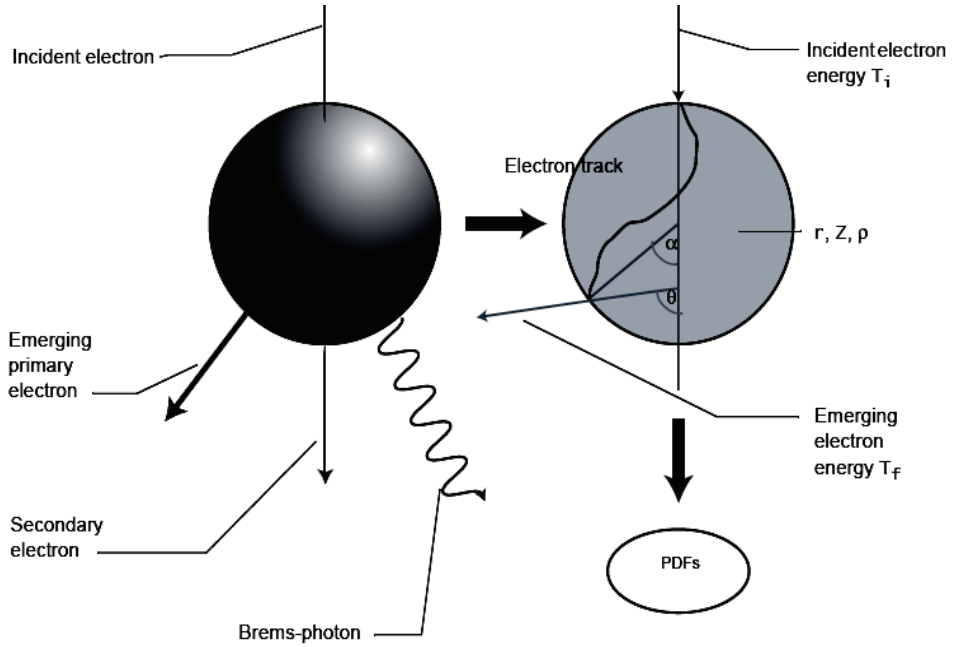

Figure 3.1: *Local geometry used in the MMC algorithm. Source: Ref. [14].*

3.3.2 Pre-processing the absorber volume

Since the MMC transport is done sphere by sphere, it is necessary to know, throughout the whole heterogeneous absorber volume, the size and mean density inside the spheres used for the transport step. For a known sphere size, the mean sphere density is obtained by averaging the density voxels of the absorber volume that are contained within the sphere in the center of each voxel. To avoid the time consuming procedure of having to determine this mean sphere density for each transport step, an algorithm was developed that allows the determination of sphere sizes and mean sphere densities at each position in the

absorber by pre-processing the whole absorber CT volume prior to the MMC simulation.

Pre-processing of the whole absorber CT volume is done in three steps [6,14]. First the CT volume is converted into density volume with a user defined resolution (0.125 – 1 cm), by applying appropriate CT-to-density conversion factors. Second, the resulting density volume is scanned for heterogeneities. To each voxel of the density volume, a sphere index is assigned that corresponds to the maximal sphere radius that can be used from the current voxel center without the corresponding sphere reaching into the other material. This process thus leads to small spheres being assigned to voxels near interfaces between different materials, and large sphere sizes assigned to voxel at larger distances from such interfaces. Two voxels of the density volume are considered to be parts of a heterogeneous area or to lie on different sides of an interface if the density ratio between the two voxels exceeds a limit (typically 1.5). However, if the densities of both voxels are below a threshold (typical value 0.05 g/cm^3), the ratio is not evaluated. This density threshold prevents noise in low density area to be interpreted as heterogeneity. For density ratios below the limits mentioned above, the MMC algorithm is capable of processing differences in the material without decreasing the step size.

In the third pre-processing step, the mean sphere densities for spheres centered on the voxel centres are determined for each voxel of the density volume. This is done by taking the average density of neighbouring voxels according to the maximal sphere size assigned to the voxel under consideration.

3.3.3 Particle transport and energy deposition

In traditional MC methods such as EGSnrc, the electron transport is simulated macroscopically in great detail. As illustrated in Figure 3.2 for a single particle

history, the basis idea of MMC [15] is to transport the primary electron in large macroscopic steps (from sphere to sphere) through the absorber. The primary electron parameters of motion after each step are then sampled from pre-calculated probability distributions. This simplification drastically reduces MMC calculation times, the price paid being an extensive 'once-for-all' preliminary calculations (i.e., building the MMC database and pre-processing the absorber volume) and some approximations for example near interfaces. In the transport process, the electron energy lost is partly deposited along the electron path, partly transferred to secondary electrons and Bremsstrahlung photons, and scored in a 3D dose matrix. The electron history is terminated if the electron is either absorbed or leaves the phantom.

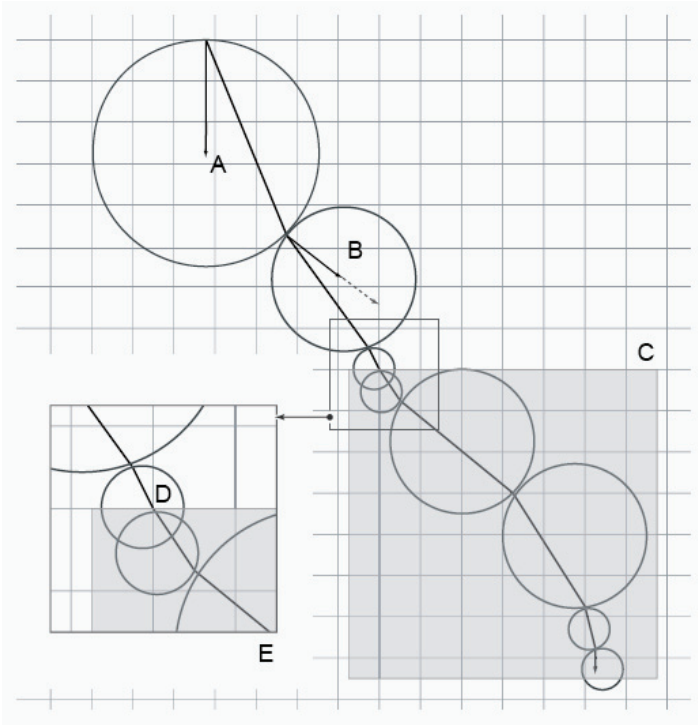

Figure 3.2: *Schematic illustration of the MMC algorithm for a primary single particle history transport. From Ref. [14].*

In the early implementation of MMC [15], the MMC database consisted of a single sphere of size 0.2 cm. Having spheres of multiple sizes in the improved

version of MMC [6] allowed for an adaptive step size algorithm for energy deposition. Due to the CT volume pre-processing discussed above, the determination of appropriate sphere size and mean sphere density for an MMC step reduces to a table look-up for the density voxel containing the current sphere centre. The sphere centre is found at a distance of one radius of the maximum allowed sphere size of the previous step from the current position of the primary electron (which is the exit position on the previous sphere), in the direction of motion of the primary electron. If the maximum allowed sphere index at the new position of the sphere centre is inconsistent with the index that has been used to calculate the new position (i.e. smaller when approaching a boundary, larger when moving away from a boundary), then the position of the sphere centre is recalculated according to the new maximum sphere index. In order to prevent infinite loops in the determination of the proper sphere centre for the next transport step, the selected sphere index for the next step is not allowed to increase again, once it has been decreased.

Another feature of the adaptive step size algorithm is the ability to stop a particle at an interface between different materials (see D in Figure 3.2), and to restart the transport with a new sphere in the new material, preserving the particle's direction of motion. Stopping at interfaces is only required if the ratio of linear stopping powers in dose volume voxels on both sides of the interface exceeds a limit (typical value 1.5). For stopping power ratios below this limit, the MMC algorithm can handle steps across material interfaces without stopping the particle at the interface. The stopping feature is very important to obtain reasonable dose distributions in and near air heterogeneities.

Primary energy is deposited along a straight line from the point where the primary electron enters the sphere to the point where it leaves. A ray trace between these two points is performed by a modified Siddon ray trace algorithm [16] through the voxels of the dose volume. For secondary particles, some

simplifications in scattering and energy deposition are made, since there is no information about the position and direction parameters for these particles in the MMC database. Secondary particles are modelled using a simple scattering model that scatters them with a fixed angle with respect to the primary electron direction. This is a major departure from MC as implemented in EGSnrc, which involves multiple scattering theories, as single scattering models have been shown to lead to inaccuracy near boundaries [8].

3.3.4 Techniques that increase the efficiency of MMC

Besides pre-calculation of PDFs and pre-processing of the CT absorber volume, so that a MMC step for primary particles reduces essentially to a look-up table process, there are other techniques and approximations that increase the speed of the MMC algorithm:

- Secondary particles (electrons and photons) released in a sphere in each MMC step are not transported at first, but stored in those voxels of the secondary energy deposition volumes where it has been released. Transport and deposition of these dose contributions are handled by post-processing of the secondary energy deposition volumes after the actual simulation.
- In the post-processing step, the secondary energy released during the simulation is ray traced through the energy deposition volume in the direction of the incident beam. This is another departure from EGSnrc.
- Mean energy absorption coefficients of photons emerging from MMC spheres for different materials, sphere sizes and incident electron energies are determined in the pre-calculations, based on the mean energy of emerging photons and data tabulated by Johns and Cunningham [17].
- The sines and cosines function calls in the transformation from spheres to phantom coordinates are replaced by table look-ups.

References

1. Bielajew, A.F., *"Monte Carlo dose calculation: why gamble with anything else?" Proc. 1st Int. Workshop on EGS4,* 1997 (Tsukuba City, Japan: Laboratory for High Energy Physics) p310–323.
2. Ayyangar, K.M., and Jiang, S.B., *"Do we need Monte Carlo treatment planning for Linac based stereotactic radiosurgery? - a case study"*, Med. Dosim. 1998, Vol **23: p**161–167.
3. Ma, C.M., et al., *"Clinical implementation of a Monte Carlo treatment planning system" Med. Phys.* 1999, *Vol.* **26**: p2133–2143.
4. Ma, C.M. and Jiang S.B., *"Monte Carlo modeling of electron beams from medical accelerators"*, Phys. Med. Biol. 1999 **Vol. 4**: R157–89.
5. Kawrakov, I., and Rogers, D.W.O., *"The EGSnrc Code System: Monte Carlo Simulation of Electron and Photon Transport"*, National Research Council of Canada (Ottawa, 2006).
6. Neuenschwander, H., Mackie, T.R.,and Reckwerdt, P.J., *"MMC - a high-performance Monte Carlo code for electron beam treatment planning"*, Phys. Med. Biol., 1995, Vol. **40**, p. 543-574.
7. Bielajew, A.F., and Rogers, D.W.O., *"PRESTA: The parameter reduced electron-step transport algorithm for electron Monte Carlo transport"*, Nucl. Instrum. Methods B, 1987, Vol. 18, p. 165.
8. Kawrakov, I., *"Accurate condensed history Monte Carlo simulation of electron transport. I. EGSnrc, the new EGS4 version"*, Med. Phys, 2000, Vol. 27, p. 285-498.
9. Berger, M.J., *"Monte Carlo calculation of the penetration and diffusion of fast charged particles"*, in *"Methods in Computational Physics"*, Edited by Alder, B., Fernbach, S., and Rotenberg M., 1963, Vol. 1, (Academic, New-York), p. 135–215.
10. Goudsmit, S. A., and Saunderson, J. L., *"Multiple scattering of electrons"*, Phys. Rev., 1940, Vol. **57**, pp. 24-29.

11. Goudsmit, S. A., and Saunderson, J. L., *"Multiple scattering of electrons. II"*, Phys. Rev., 1940, Vol. **58**, pp. 36-42.
12. Kawrakow, I. and Bielajew, A. F., *"On the representation of electron multiple elastic-scattering distributions for Monte Carlo calculations"*, Nucl. Instrum. Methods, 1998, vol. **134B**, pp. 325–336.
13. Walters, B., Kawrakow, I., and Rogers, D.W.O., *"DOSXYZnrc users manual"*, Ionizing Radiation Standards, National Research Council of Canada (Ottawa, 2007).
14. Varian Medical Systems, *"Electron Monte Carlo Algorithm: Reference guide"*, 2003 (Palo Alto, CA).
15. Neuenschwander, H., and Born, E.J., *"A macro Monte carlo method for electron beam calculations"*, Phys. Med. Biol., 1992, Vol. **37**, p. 107-125.
16. Siddon R.L., *"Fast calculation of the exact radiological path for a three-dimensional CR array"*, Med. Phys, 1985, vol. **12**, p. 252-255.
17. Johns, H.E. and Cunningham J.R., "*The Physics of Radiology*", 1983 (Springfield, IL, Thomas).
18. ICRU, *"Radiation dosimetry: Electron beams with energies between 1 and 50 MeV"*, ICRU Report 1984, vol. 35 (International Commission on Radiation Units and Measurements, Bethesda).

Chapter 4: Dose profile extraction from Gafchromic© EBT films

4.1 Introduction

Measurements in this project are essentially dose profiles (dose along a specific direction at a specified depth in a phantom), and in many cases they involve sharp dose gradients. In this context, film dosimeters, due to their high spatial resolution, are the most appropriate detector for radiation dosimetry. In this chapter, we describe a procedure for extracting dose profiles from irradiated Gafchromic© EBT films by means of a commercial flat-bed document scanner. This procedure builds on the approach developed in Ref. [1] for Gafchromic© EBT film calibration.

General features of radiochromic films are discussed in Section 4.2, while the specific description of Gafchromic© EBT film and their response to radiation is given in Section 4.3. Section 4.4 is devoted to the calibration procedure of Gafchromic© EBT film and the approach used to extract dose profiles from these films is described in Section 4.5. A validation of this extraction approach is discussed in Section 4.6.

4.2 Generalities about Radiochromic films

In many dosimetry applications there is often a need for detectors having the following properties: 2D dose measurement capabilities, an easy and fast processing, a negligible energy dependence, a near tissue equivalence, and a high spatial resolution. One or many of these features are lacking in conventional detector systems such as ionization chambers, semiconductor, thermo-luminescent dosimeters (TLDs) and radiographic films. While Ionization chambers and semiconductors have a relatively low spatial resolution, TLDs are cumbersome and time consuming when used for 2D dose measurements. Also,

radiographic films require chemical processing, are sensitive to room light, are not tissue equivalent, and they have a very energy dependent response in the keV range. These difficulties have lead to the development of radiochromic film dosimeters, which have a very high spatial resolution and a relatively low spectral sensitivity variation, are near tissue equivalent and insensitive to visible light, thus offering ease of handling and preparation in room light [2]. Radiochromic dosimeters change color (radiochromic reaction) directly after absorption of energetic radiation, without requiring latent chemical, optical or thermal processing.

Many types of radiochromic films are provided by various manufacturers, among which are [3]: the *FW-60 nylon* film by Far West Technology (Goleta, CA, USA), the *Gafchromic©* film by International Speciality Products (Wayne, NJ, USA), the *B3* type film by GEX Corporation (Centennial, CO, USA) and more recently the SIFID film by Gordhan Patel and JP Laboratories (Middlesex, NJ, USA). All the above mentioned films have the necessary sensitivity for medical physics applications, except the *FW-60 nylon* film, which is used for high dose applications such as radiation processing, food irradiation, and sterilization. Many forms of Gafchromic© films are now available; they have similar sensitive emulsion basically, and differ essentially in film construction and emulsion thickness. However, throughout this work, we use EBT Gafchromic© films.

4.3 Description of Gafchromic© EBT films

Gafchromic© EBT film is the latest model of Gafchromic films released in 2004. As illustrated in Figure 4.1, they consist of two 17μm thick active/sensitive layers separated by a 6μm thick surface layer, all sandwiched between two 97μm thick clear polyester sheets. The atomic composition of Gafchromic© EBT dosimetry film is **C** (42.3%), **H** (39.7%), O (16.2%), **N** (1.1%), **Li** (0.3%), **Cl** (0.3%), for an effective atomic number $Z_{eff} = 6.98$, which is close to the value 7.3 for water [4].

Gafchromic© EBT films are colorless and have the following characteristics, according to the manufacturer [4]: (i) a dose range of 1 cGy to 8 Gy (i.e., about 10 times more sensitive than previous generations), (ii) uniformity better than 1.5%, (iii) a faster and lower post-exposure density growth, (iv) an energy independence from the keV range into the MeV range and (v) can withstand temperatures up to 70 ^{o}C.

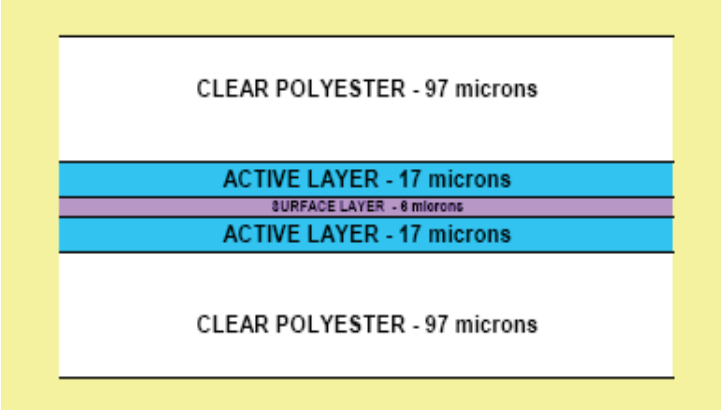

Figure 4.1: *Configuration of Gafchromic EBT dosimetry film [4].*

The radiosensitive layer in Gafchromic© EBT film contains microcrystals of a monomer, which undergoes a partial polymerization when irradiated with ionizing radiation, turning into a blue color that becomes increasingly darker as the dose increases. The increase in color of the film is measured at a narrow spectral wavelength band using a spectrophotometer or a densitometer (such as a document scanner), and the results are expressed in terms of a change in the absorbance (i.e., optical density OD) or in the transmittance T of light by the film ($OD = -\log_{10} T$). When the polymer on the irradiated Gafchromic© EBT film is exposed to visible light it shows absorption maxima at about 636 nm and 585 nm wavelength (see Figure 4.2), near the red color of the visible spectrum. Consequently, the response of this dosimetry film will be enhanced by measurement with red light from a densitometer.

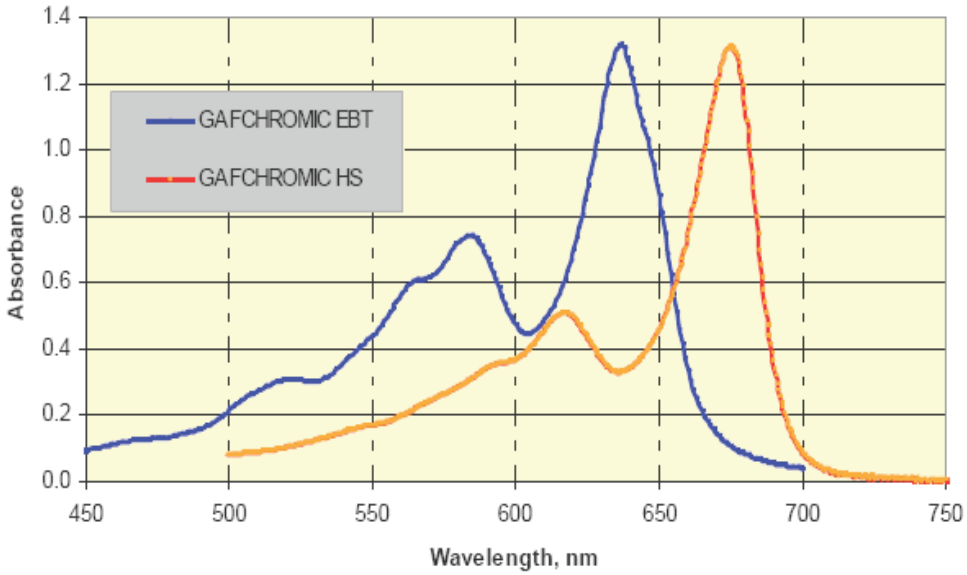

Figure 4.2: *Absorption spectra of Gafchromic© EBT and HS dosimetry films [4].*

4.4 Calibration of Gafchromic© EBT films

The purpose of the calibration is to find a relationship between the optical densities (OD) measured on irradiated films and the dose received. In our calibration procedure, we follow the protocol described in Ref. [1] whose steps are:

a) The film is cut in 2.5 cm by 2.5 cm pieces and grouped in sets of four.

b) Each set of such unexposed film pieces is scanned three times and the scan transmission values are saved in TIF (Tagged Image File) format.

c) One set of film is kept unexposed. The remaining film sets are each positioned at a given depth in a solid water phantom and a known dose of radiation is given to each set. These films are then left for a period of about 6 hours to self-develop [4].

d) Each set of exposed film pieces is scanned again three times, leading to scan transmission values also stored in TIF image file format.

In the calibration process for electron beams, a 20x20 cm^2 field size is used with films placed at depths of 3.0 cm for 12 to 20 MeV beams, whereas for photon

beams a 10x10 cm^2 field size is used with films placed a depth of 10 cm in order to obtain the most uniform dose over the 4 film pieces. The dose given to each film set is then derived from the Linac output (measured just before film calibration) via appropriate data (PDDs and relative dose factors). All scans are done with films always positioned in the same orientation and using the 48-bit RGB mode (16 bits per color) with a 127 dots per inch (ppi) resolution using a document scanner. Throughout this work, an EPSON Expression 1680 document scanner is used to scan all Gafchromic© EBT films.

Multiple scans are performed in order to remove the noise caused by the scanner via subsequent averaging of scanner images. Following multiple scans (three) mentioned above for each set of four film pieces, we have three images for the unexposed set and three for the exposed set. All the images are imported into an in-house manipulation routine [5] written with Matlab. The three images for each set of four films are averaged to remove scanner noise and a 2D Wiener filter is applied to the averaged image to decrease the image noise caused by imperfections in the film sample.

For each film piece, we consider a region of interest (ROI) of 5x5 pixels and define the transmission scan value as the mean pixel value over the ROI. This leads to the transmission scanner readings $I_{un\exp}$ and $I_{\exp}$ for unexposed and exposed films respectively, as well as their respective standard deviations $\sigma_{I\,un\exp}$ and $\sigma_{I\exp}$. The standard deviation on the other hand is defined as the standard deviation over the ROI for the corresponding exposed or unexposed film. Thus the net optical density $netOD^i(D_j)$ and the corresponding standard deviation $\sigma^i_{netOD}(D_j)$ for the i-th film piece that received a dose D_j can be written as [6]:

$$netOD^i(D_j) = OD^i_{\exp}(D_j) - OD^i_{un\exp}(D_j) = \log_{10}\left(\frac{I^i_{un\exp}(D_j) - I_{bckg}}{I^i_{\exp}(D_j) - I_{bckg}}\right), \qquad (4\text{-}1)$$

$$\sigma^{i}_{netOD}(D_j) = \frac{1}{\ln 10}\sqrt{\frac{\left(\sigma^{i}_{I\,un\,\exp}(D_j)\right)^2 + \left(\sigma_{bckg}\right)^2}{\left(I^{i}_{un\,\exp}(D_j) - I_{bckg}\right)^2} + \frac{\left(\sigma^{i}_{I\,\exp}(D_j)\right)^2 + \left(\sigma_{bckg}\right)^2}{\left(I^{i}_{\exp}(D_j) - I_{bckg}\right)^2}}\,, \qquad (4\text{-}2)$$

where $I^{i}_{\exp}(D_j)$ and $I^{i}_{un\,\exp}(D_j)$ are the scan transmission readings for the i-th exposed and unexposed film piece, which is part of the set j-th set of four film pieces that received a dose D_j. $\sigma^{i}_{I\,\exp}(D_j)$ and $\sigma^{i}_{I\,un\,\exp}(D_j)$ denote the associated standard deviations. The zero light transmitted intensity value I_{bckg} characterizes the background signal of the scanner, as well as the corresponding standard deviation σ_{bckg} [1]. For a particular dose point (D_j) the final net OD $netOD(D_j)$ and the standard deviation $\sigma_{netOD}(D_j)$ are obtained as a weighted mean over the four film pieces of each set, i.e.,

$$netOD(D_j) = \frac{\sum_{i=1}^{4}[netOD^{i}(D_j)/(\sigma^{i}_{netOD}(D_j))^2]}{\sum_{i=1}^{4}[1/(\sigma^{i}_{netOD}(D_j))^2]}\,, \qquad (4\text{-}3)$$

$$\left[\sigma_{netOD}(D_j)\right]^2 = \frac{1}{\sum_{i=1}^{4}[1/(\sigma^{i}_{netOD}(D_j))^2]}\,. \qquad (4\text{-}4)$$

A plot of the dose D_j received by each set of film against the net OD on the film leads a calibration curve, which is sensitive to the beam quality, film batch, and the scanner used.

Figure 4.3 shows three calibration curves obtained for a 6 MV photon beam, and for 12 and 16 MeV electron beams. The fact that the 3 curves are nearly identical illustrates the energy independence of Gafchromic© EBT films, which is an important feature for any relevant dosimeter. This is also relevant for the PDD measurements in electron beams due to the bremsstrahlung tail. The delivered dose D versus the net OD is fitted as $D = a \times netOD^3 + b \times netOD^2 + c \times netOD$, where $a = 2377.52$, $b = 520.99$ and $c = 481.41$. Hence, by measuring the OD on any area of a film (from the same batch) we can determine the dose deposited on the area.

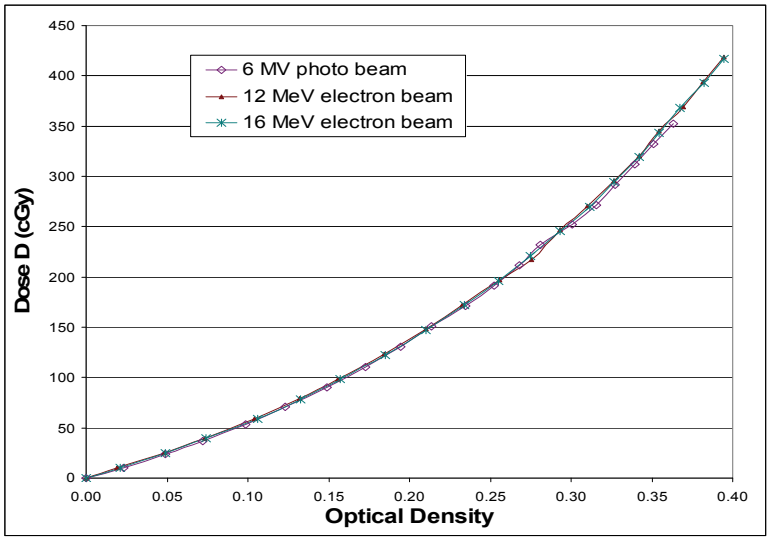

Figure 4.3: Gafchromic© EBT film calibration curve for various beam qualities.

4.5 Dose profile extraction from Gafchromic© EBT films

For dose profile measurements, we cut films into strips of width 2.5 cm and length equal to the length of the profile under interest (see Figure 4.4). We propose the following protocol, which is an extension of the protocol in Ref. [1]:

(a) Each unexposed film strip is scanned three times, and scan transmission values are saved in a TIF file format. The three images are imported into the MatLab routine "**PROFILE_STEP1**" (described in Appendix A), where they are averaged and a Wiener filter is applied.

(b) The film strip is then exposed under desired conditions, let to self-develop for six hours and then also scanned three times, averaged and filtered as described in the previous step.

(c) The last step is executed using the MatLab routine "**PROFILE_STEP2**" described in Appendix B. Here the averaged image is subdivided into small consecutive 2D voxels of size $\Delta x \times \Delta y$ along the direction of the profile as shown in Figure 4.4. For the *j*-th voxel, the scan transmission values $I_{un\exp}(D_j)$ for unexposed and $I_{\exp}(D_j)$ for exposed film are calculated as the mean pixel value over the voxel, which leads to the net OD $netOD(D_j)$ on the voxel *j* calculated

using Eq. (4-1). Analogously, the standard deviation in the scan transmission value $\sigma_{I\,un\exp}(D_j)$ and $\sigma_{I\exp}(D_j)$ are used in Eq. (4-2) calculate the standard deviation $\sigma_{netOD}(D_j)$ in the net OD. Note that in this case the index I in Eqs (4-1) and (4-2) is irrelevant because a single film strip is scanned each time. Knowing $netOD(D_j)$ and $\sigma_{netOD}(D_j)$ for each voxel *j* the calibration cure curve allows to obtain the dose D_j on each voxel *j*, and the associated standard deviation.

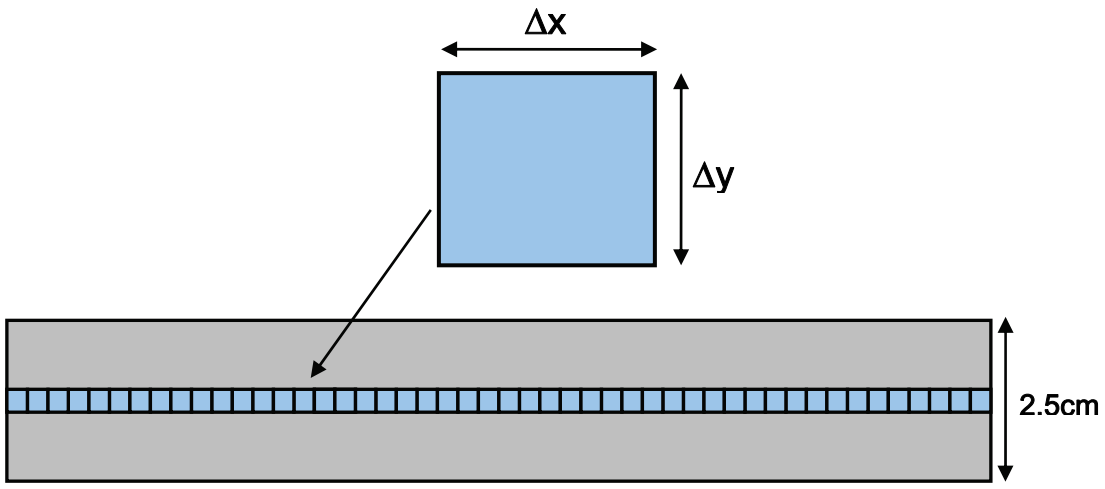

Figure 4.4: Film subdivision for extracting the dose profile along the x-axis. A magnification of a voxel is done for better illustration.

Note that the size of the voxel (i.e., Δx and Δy) determine the spatial resolution of the film dose measurement. Indeed, since we are scanning with a 127 ppi, the image resolution on the scanned film is $\frac{127\ pixels/inch}{25.4\ mm/inch} = 5\ pixels/mm$, thus selecting with 5x5 pixels corresponds to a 1 mm x 1 mm resolution. Finally, marks are placed on the irradiated film in order to identify the position of the Linac crosshair in the scanned image.

4.6 Validation of the dose profile extraction algorithm

We now attempt to validate the above dose profile extraction approach described in the previous section. For this purpose, EBT Gafchromic film strips are

irradiated at various depth in a solid a water phantom and the dose is extracted as described above. Results for two cases are summarized in Figure 4.5.

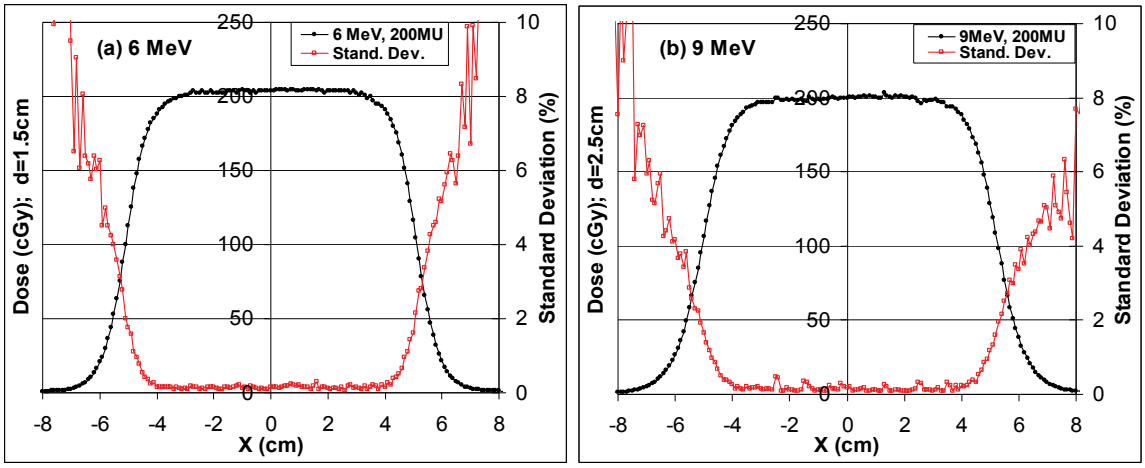

Figure 4.5: *Dose profiles and standard deviation extracted (using a 5x5 pixel resolution) from EBT Gafchromic© film strips exposed in solid water phantom under the following conditions:* ***(a)*** *6 MeV electron beam, depth d=1.5 cm;* ***(b)*** *9 MeV electron beam, depth d =2.5 cm. A 10x10 cm² applicator and SSD=100 cm is used for both.*

The dose profile and standard deviation in Figure 4.5 (a) for a 6MeV electron beam is obtained with 200 MUs given with a 10x10 cm² applicator, SSD=100 cm and the film at depth 1.5 cm. Given that the machine output was 99.8 cGy per 100 MU at depth 1.56 cm, and that the percent depth dose at the two depths are PDD(1.5 cm)=97.6% and PDD(1.56 cm)=96.0%, then the expected dose at 1.5 cm depth is $D(1.5\text{ cm}) = \frac{\text{PDD}(1.5\text{ cm})}{\text{PDD}(1.56\text{ cm})} \times \frac{99.8\text{ cGy}}{100\text{ MU}} \times 200\text{ MU} = 202.9\text{ cGy}$, which agree within a fraction of percentage with the value 203.4 cGy on the central axis of the profile in Figure 4.5(a). Similarly, for the 9MeV beam the output at reference depth 2.3 cm is 101.5 cGy per 100 MU, which leads at 2.5 cm depth to the expected dose

$$D(2.5\text{ cm}) = \frac{\text{PDD}(2.5\text{ cm})}{\text{PDD}(2.3\text{ cm})} \times \frac{101.5\text{ cGy}}{100\text{ MU}} \times 200\text{ MU} = \frac{95.8 \times 101.5\text{ cGy}}{98.5 \times 100\text{ MU}} \times 200\text{ MU} = 197.4\text{ cGy},$$

which is within 1% of the value 200.0 cGy extracted from the Gafchromic on the central axis in Figure 4.5(b). This excellent agreement indicates that the dose

profile extraction works properly. Further insight into the accuracy of this dose profile extraction is provided in Chapter 4 for both uniform and heterogeneous phantoms.

The standard deviation of the extracted dose, also shown in Figure 4.5, is very small in general, typically less than a faction of % in the high dose regions of the profile. However, as expected, the standard deviation increases as the dose decreases in the penumbra and the umbra profile, where it can be as high as 40%. This increase in the standard deviation reflects the low signal to noise ratio in the optical density in areas of the film where the deposited dose is very small.

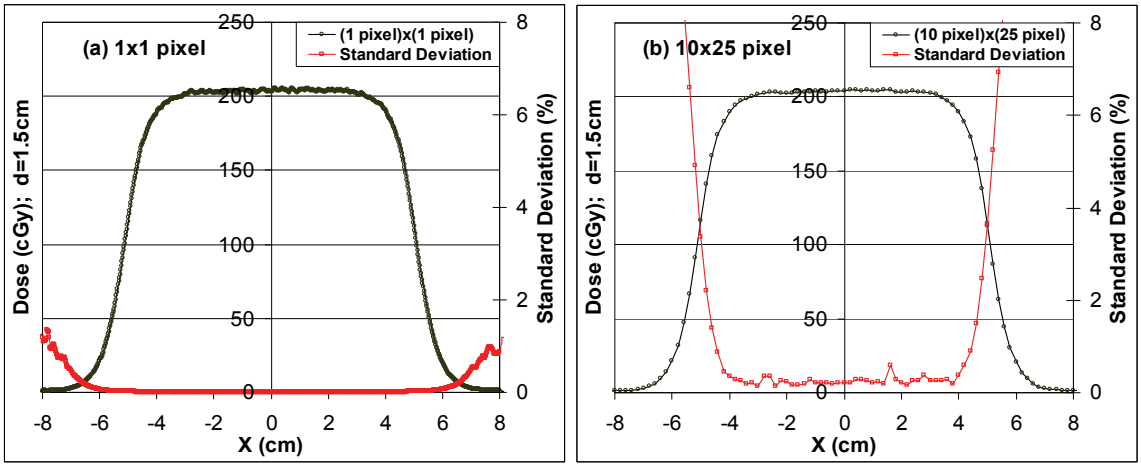

Figure 4.6: *Dose profiles and standard deviation extracted using various spatial resolution from scanned EBT Gafchromic© film strips exposed at depths d=1.5 cm in a solid water phantom by a 6 MeV electron beam: (a) 1x1 pixels voxel size or equivalently a 0.2 mm by 0.2 mm resolution; (b) 10x25 pixels voxel size or equivalently a 2 mm by 5 mm resolution.*

Dose profiles displayed in Figure 4.5 are extracted using voxels of size 5x5 pixels on the image of the scanned EBT Gafchromic© film for each dose point, which corresponds to a spatial resolution of 1 mm by 1 mm, i.e., Δx=1 mm and Δy=1 mm in Figure 4.5. We display in Figure 4.6 the dose profiles extracted from scanned films using a 1x1 pixel resolution (i.e., Δx=0.2 mm and Δy=0.2 mm) and a 10x25 pixel resolution (i.e., Δx=2 mm and Δy=5 mm). The dose profiles for the

two cases in Figure 4.6 are identical and identical to the 6 MeV profile in Figure 4.5. The three profiles are plotted separately because they would not be distinguishable on the same plot. The only distinction occurs for the standard deviation, which increases with the voxel size used for extracting the profile. This is due to the fact that for larger voxel sizes, a larger number of pixels with a broader signal distribution (compared with smaller voxel sizes) are averaged to obtain a single dose point, thereby leading to a larger standard deviation.

The fact that the profiles are unchanged when the resolution changes from 2 mm by 5 mm to 0.2 mm by 0.2 mm indicates that even within a 0.2 mm by 0.2 mm area on the film there is enough active material to interact with the electron beam to yield a good signal to noise ratio. Both resolutions lead to the same dose here because of the relatively flat nature of the profile considered (i.e., no sharp dose gradients). The scanning resolution can be improved beyond the 127 ppi used in this work, in this case extracting dose with a 1x1 pixel resolution as in Figure 4.6(a) leads to problems related to low signal to noise ratio in each voxel. Using a large voxel size such 2 mm by 5 mm is inadequate in the presence of sharp dose gradients, as it leads to dose averaging effects. The 127 ppi scanning resolution and the 1 mm by 1 mm spatial resolution for dose extraction is a good compromise for the type of dose gradients involved in his work.

References

1. Devic, S., et al., *"Precise radiochromic film dosimetry using a flat-bed document scanner",* Med. Phys., 2005, **vol. 32**, p. 2245-2253.
2. Niroomand-Rad, A., et al., "*Radiochromic film dosimetry: Recommendations of AAPM Radiation Therapy Committee Task Group 55",* Med. Phys., 1998, **vol. 25**, p. 2093-2115.
3. Soares, C.G., *"Radiochromic film dosimetry",* Radiation Measurements, 2006, **vol. 41**, p. S100-S116.

4. Internal Specialty Products, *"Gafchromic© EBT: Self-developing film for radiotherapy dosimetry",* August 2007.
5. Devic, S., Private Communication, (2007).
6. Devic, S., et al, *"Dosimeric properties of improved Gafchromic films for seven different digitizers",* Med. Phys., 2005, **vol. 31**, p. 2392-2401.

Chapter 5: Evaluation of Eclipse© using heterogeneous phantoms

5.1 Introduction

This chapter is devoted to the evaluation of the Eclipse© (varian, Palo Alto, CA) treatment planning system, by comparison of Electron Monte Carlo calculations from Eclipse© treatment planning system with measurements, and with full Monte Carlo (MC) simulations done using DOSXYZnrc© (national Research Council of Canada, Ottawa, ON). While measurements are done using physical phantoms, calculations on Eclipse© and in DOSXYZnrc© are done with a virtually reproduced copy of the physical phantom on each of the two platforms (Eclipse© and DOSXYZnrc©). The alternative approach of CT scanning phantoms and exporting them on each platform for calculations introduces some uncertainties originating from the conversion of CT data into electron densities and from noise and artefact in the image coming from the CT scan. Thus, a virtual reproduction of the physical phantom avoids such uncertainties. It also introduces new uncertainties related to the size of the pixel in the phantom design, which is very small and which we estimate to be less than half mm.

All measurements throughout this work are done on a Varian© (Palo, Alto, CA) CLINAC 21 EX, using a source to surface distance (SSD) of 100 cm and a 10x10 cm^2 applicator with a standard 10x10 cutout. Results of all calculations and measurements are given and compared in terms of absolute dose. Also, for dose profiles, we place our focus near depths of dose maximum, where the percent depth dose is relatively flat. This way, we avoid regions of high dose gradients where positioning accuracy is very difficult to achieve and which are not clinically important for electron beams because they are located beyond the dose prescription depths R_{80} and R_{90}. Also, in our evaluation of Eclipse© we focus on heterogeneous phantoms, as uniform phantoms have been the subject of a previous investigation [1].

This chapter is organized as follows: In Section 5.2, we describe experimental setups and procedures. Details on how calculations are done on Eclipse© and DOSXYZnrc© [2] platforms are given in Sections 5.3 and 5.4, respectively. Section 5.5 is devoted to an error analysis of our measurements, which leads to the determination of relevant error bars. An evaluation of Eclipse© for uniform phantoms is briefly discussed in Section 5.6. Comparisons of Eclipse MC and MC calculations with measurements for heterogeneous phantoms are presented in Section 5.7 for "two-bars" and in Section 5.8 for "three-bars" phantoms. The difficulties of comparing dose calculations in very low dose area and in near high dose gradients are discussed in Section 5.9.

5.2 Physical phantoms and measurements

Physical phantoms used in our measurements are built by various combinations of rectangular bars (simply referred hereafter as "bars") of various tissue densities. Only lung and bone tissue equivalent bars are used in this work. Each bar has 2 cm width, 2 cm height and is 30 cm long, as illustrated in Figure 5.1.

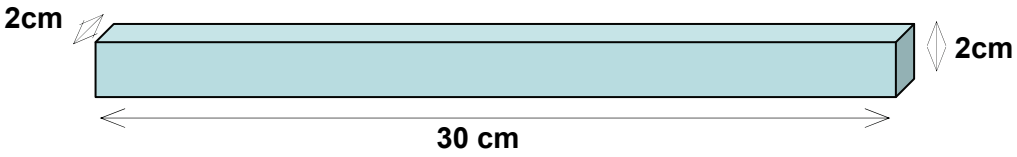

Figure 5.1: *Typical bar of tissue used with solid water blocs as heterogeneity.*

Sandwiching two bars with solid water blocs leads to a phantom illustrated in the left image in Figure 5.2, which is referred to hereafter as the *"two-bars"* phantom. Superposing three bars separated by air gaps on a solid water bloc leads to the phantom on the right image in Figure 5.2, which is hereafter referred to as the *"three-bars"* phantom.

For dose profile measurements, a piece of Gafchromic© EBT film is placed below each of these phantoms perpendicularly to the bars and the whole set is placed above a slab of solid water phantom which provides backscatter on the film. Since for the “two-bars” phantom the bars are sandwiched between solid water blocs, there are air cavities at the interfaces between the bars and the solid water blocs, due to irregularities at their contact surface. As we shall see later, such air cavities may substantially affect measurement results. In order to minimize the effects of such air cavities, we apply a water equivalent liquid gel at the contact surfaces between the bars and the solid water blocs.

Figure 5.2: *Physical phantoms used for measuring heterogeneity effects on dose profiles. On the left, a phantom with two heterogeneity bars (i.e., the "two-bars" phantom) sandwiched in solid water blocs; On the right, a phantom with three heterogeneity bars (i.e., the “three-bars” phantom) separated by air gaps.*

Two types of heterogeneity bars are used in this project: one is equivalent to bone tissue (Cortical bone RMI 450) and the other to lung tissue (Lung LN 450). The properties of those tissue materials provided by the manufacturer are summarized in table 5.1. Throughout this work, our mention of “solid water” shall refer to the water equivalent tissue (Solid Water RMI 457) whose characteristics are also given in Table 5.1.

Material	Physical properties of each material						Proportion of atomic elements in each								Total
	Z_{eff}	Z_{avr}	n_e/ρ	ρ	n_e	n_e/n_w	%H	%C	%N	%O	%Mg	%Si	%Cl	Ca	
Solid Water (RMI 457)	8.112	6.361	0.539	1.046	0.564	1.016	8.02	67.23	2.41	19.91			0.14	2.31	100.02
lung (LN450)	7.835	6.689	0.541	0.450	0.243	0.438	8.47	59.57	1.97	18.11	11.21	0.58	0.10		100.01
Bone (Cortical RMI 450)	14.017	10.336	0.516	1.819	0.939	1.692	3.41	31.41	1.84	36.50			0.04	26.81	100.01

Table 5.1: *Physical properties of tissue materials involved in the physical phantom: Z_{eff} and Z_{av} are the effective and average atomic numbers, n_e/ρ is the mass electron density (in units of the Avogadro number N_A), ρ denotes the physical density, n_e denotes the electron density (in units of N_A), n_e/n_w denotes the electron density relative to water.*

5.3 Calculations on the Eclipse© platform

In contrast to the case of a typical treatment planning process on Eclipse©, our calculations do not involve manipulations of imported CT image data, since we design our phantom virtually instead of uploading its CT image. In this context, the main steps in the dose calculation on Eclipse© are the following:

1) Design the phantom geometry and contour with inherent heterogeneities: various tissue volumes are specified by assigning a specific CT number;
2) Selection of radiation delivery parameters such as the accelerator unit, the beam energy, the gantry and collimator angles, the source to surface distance (SSD), the applicator and field size, etc.;
3) Specification of electron MC parameters such as the grid and voxel sizes, required accuracies (dose and MUs), dose smoothing or not, …;
4) Run Electron MC calculations and exporting results in a desired format.

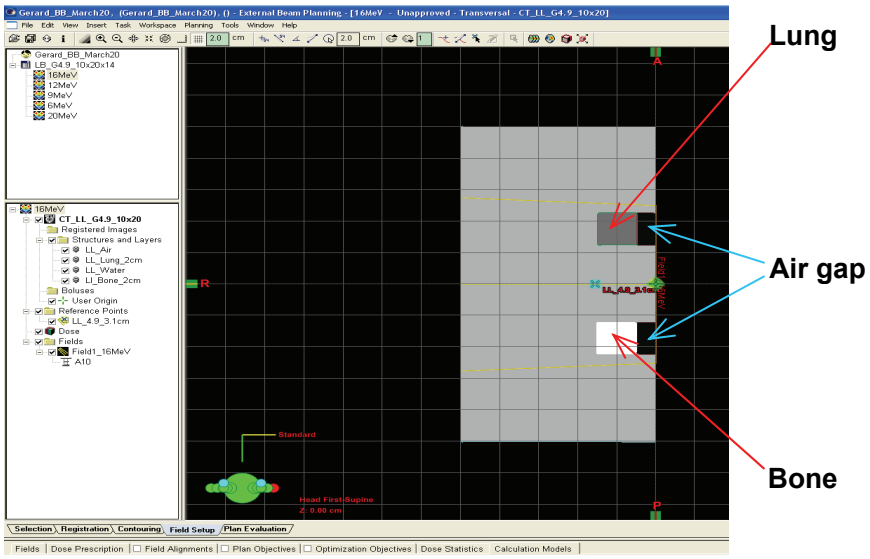

Figure 5.3: *Screen capture of a cross-section of the "two bars" phantom reproduced on Eclipse©. The two bars of heterogeneity are clearly visible, as well as the two air gaps.*

As mentioned earlier, the physical phantom used for measurements is reproduced virtually in 3D on Eclipse© for dose calculation. Figure 5.3 shows a cross-section of the “two-bars” phantom as virtually reproduced on Eclipse©. In

the designing process of the heterogeneous phantom on Eclipse©, tissue geometries and volume of various densities are assigned a given Hounsfield unit (HU) or CT number, which is derived using the density of the corresponding material from Table 5.1, and an interpolation of Eclipse's HU versus mass density calibration curve illustrated in Figure 5.4. It follows that for:

(i) solid water whose density is 1.046 g/cm^3, the CT number used is +44;

(ii) lung tissue whose density is 0.45 g/cm^3, the CT number used is -552;

(iii) cortical bone whose density is 1.82 g/cm^3, the CT number +1424.

The size of the phantom reproduced is 20 cm along the x-direction in which the profile is calculated, and 16 cm in the y-direction. This is much larger than the size 10x10 cm^2 of the applicator cone used throughout this project. The phantom depth or length along the z-direction (i.e., parallel to the electron beam entrance) depends on the selected electron beam energy and is taken larger than the electron range in water for the corresponding beam energy. The same considerations are used for selecting the phantom size used for measurements.

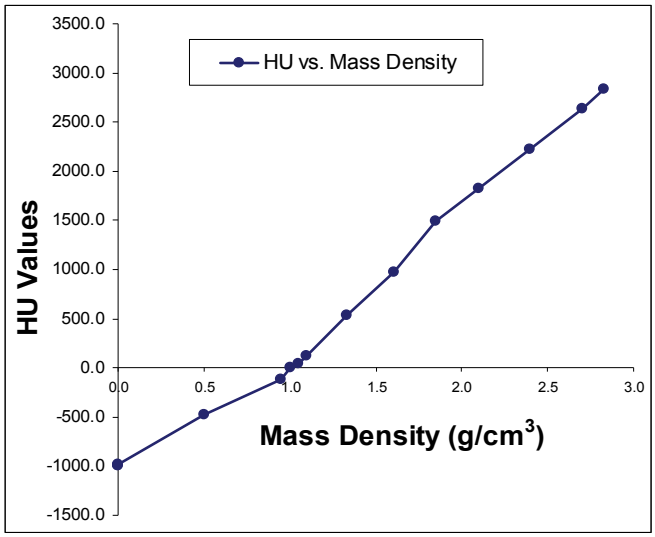

Figure 5.4: *Hounsfield unit values vs. mass density calibration curve for Eclipse© treatment planning system.*

In step 2) of calculations in Eclipse©, we select various electron beam energies from CLINAC 21EXA, which is the linear accelerator unit used for our evaluation. The collimator angle is fixed and 90^o, and gantry angle at 0^o (oblique incidence is

beyond the scope of this work). Throughout this project, we use a source to surface distance of 100 cm and a 10x10 cm^2 applicator with a standard 10x10 cutout to define the field size on the phantom surface.

In step 3) where we define electron MC calculation parameters on Eclipse©, the smallest grid size of 1mm is selected, with the purpose of properly tracking expected sharp gradients in dose profiles. The accuracy of 2% is selected for monitor units (MU) calculations and the best accuracy of 1% is selected for dose calculations. Eclipse© Provides an option for dose "smoothing". We realised that selecting an accuracy better than 2% prevents Eclipse from computing the number of MUs. Smoothing is a mathematical operation that aims at reducing the statistical noise and the amount of time spent in the calculation. Reducing statistical noise prevents an irregular dose pattern due to high statistical uncertainty from being interpreted as a dose variation due to heterogeneity. However, it has been shown [3] that smoothing could distort dose profiles from reality in the presence of sharp dose gradients. For this reason, the "no smoothing" option has been used for all our calculations in Eclipse©.

In our measurements on the physical phantom, we set a given number of MUs (say X_{MU}) on the accelerator console to deliver dose. In contrast, for the Eclipse electron MC dose calculation in step 4), we do not specify the number of MUs as input to get the dose; instead a reference point is selected in the phantom and a specified dose (e.g., 1 Gy) is required to be delivered at that point. Once the calculation on Eclipse is done, Eclipse's gives a dose matrix that can be exported, as well as the number of MUs (say N_{eMU}) that needs to be set on the linac console to obtain the specified dose at the reference point. In order to compare Eclipse MC calculations with measurements where the number of MUs X_{MU} is set on the linac console, we scale the dose at any point in the phantom as:

$$D(X_{MU}, P) = \frac{X_{MU}}{N_{eMU}} D(N_{eMU}, P), \tag{5.1}$$

where $D(N_{eMU}, P)$ is the dose obtained from Eclipse MC calculations at an arbitrary point P in the phantom, and N_{eMU} the corresponding number of MUs from Eclipse. $D(X_{MU}, P)$ is the dose a point P in the phantom for a number of MUs X_{MU} set on the Linac console, Finally, we use **Version 8.1.17** of Eclipse© MC algorithm throughout this work.

5.4 Calculation on the DOSXYZnrc© platform

The full Monte Carlo dose calculations are done with DOSXYZnrc© using a virtual reproduction of the physical phantom. Figure 5.5 shows a snapshot of a cross section of the virtually reproduced phantom on DOSXYZnrc©. This virtual phantom is the same as the one used on Eclipse (see Section 5.3).

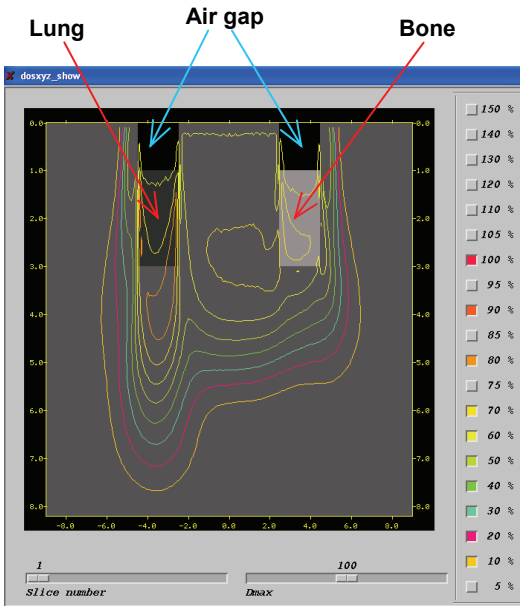

Figure 5.5: *Screen capture of a cross-section of a "two-bars" phantom in DOSXYZnrc©. Some isodose lines following calculations are shown.*

In contrast to Eclipse MC calculations which are very fast (completed within a few minutes), we cannot use a single small voxel size along all coordinates in the full MC simulation because it is very time consuming and typically takes many hours to complete. The reason is that the resulting matrix of voxels becomes too large,

leading to a much longer computation time. In order to reduce the computation time in DOSXYZnrc©, we use a small voxel size (1 mm) only along the x-direction across the heterogeneity bloc where the profile is to be measured. This allows tracking of the expected sharp dose gradient. In the y direction where there is no gradient (except in the penumbra), we use a larger voxel size of 2 mm, which also helps improve the statistical uncertainty of MC simulations by reducing statistical noise. Along the z-direction parallel to the electron beam, we also use a 2mm voxel size, as a smaller one does not substantially change results. As we shall see later, this appropriately chosen voxel size allow us to adequately track the sharp dose gradients in the profile, while keeping a very good statistical accuracy for the MC calculation. Despite such relatively larger voxels, a typical MC calculation still takes many hours on our computer cluster to complete.

Since we need absolute dose, we must extract it in cGy from MC calculations. Output from MC simulation is in cGy/particle. To convert this output into cGy/MU, we express the number of particles per MU (i.e., $[\#\,\text{of (part./MU)}]$) as

$$[\#\,\text{of (part./MU)}] = [\#\,\text{of (part./cGy)}] \times [\#\,\text{of (cGy/MU)}] = \frac{[\#\,\text{of (cGy/MU)}]}{[\#\,\text{of (cGy/part.)}]}$$

The two quantities involved in the ratio are obtained as follows: From the output measurement for a given electron beam energy, i.e., the dose at z_{max}, we obtain the quantity $[\#\,\text{of (cGy/MU)}]$. Then we simulate this output measurement in MC by calculating the dose per particle at z_{max}, which leads to the second quantity $[\#\,\text{of (cGy/part.)}]$. Having the quantity $[\#\,\text{of (part./MU)}]$ and the number of MU given, the output of a MC calculation in (cGy/part.) is converted into dose using

$$[\text{Dose (in cGy)}] = [\text{MC results in cGy/part.}] \times [\#\,\text{of (part./MU)}] \times [\#\,\text{of MUs given}]$$

5.5 The error analysis

Most measurements in this project involve Gafchromic© films. In this section, we discuss our estimation of the uncertainties from Gafchromic© film measurements. We have identified the following major sources of errors in our measurements:

(i) The dose resolution or uncertainty σ_{res} in the dose extraction from EBT Gafchromic© films: This is related to the standard deviation $\sigma_{netOD}(D_j)$ in the net optical density on the voxel j of the film that received a dose D_j, as discussed in Chapter 4. Using the parameters a, b, and c obtained from the third order polynomial fit of the calibration curve (see Section 4.4), the uncertainty in the dose from each portion of EBT Gafchromic© film that received a dose D_j is obtained as

$$\sigma_{res}(D_j) = a \times [\sigma_{netOD}(D_j)]^3 + b \times [\sigma_{netOD}(D_j)]^2 + c \times \sigma_{netOD}(D_j).$$

This dose resolution (a type A uncertainty) has already been illustrated as the standard deviation in Fig. 4.5.

(ii) Besides the dose resolution, there are many other sources of uncertainties associated with EBT Gafchromic© films and their processing, such as the non-uniformity of the scanner response, the scanner noise, the film non-uniformity, and the calibration fit uncertainties. We denote these uncertainties as $\sigma_{EBT}(D_j)$ and estimate them to be about 2% of any dose D_j extracted from a film voxel [4], i.e.,

$$\sigma_{EBT}(D_j) = \frac{2}{100} D_j.$$

(iii) The linac beam output: Clinically, the beam output is required to be precise within 2 %. Therefore, for any voxel of the film that receives a dose D_j, we estimate the uncertainty in dose due to the output fluctuation (type B uncertainty) as

$$\sigma_{out}(D_j) = \frac{2}{100} \times D_j.$$

(iv) The uncertainty σ_{pos} due to the error in positioning of the film before irradiation (this is another type B uncertainty): As illustrated in subsequent sections of this chapter, there are various areas of sharp dose gradients in our film measurements, which lead to a strong spatial dependence of the measured dose. For dose profile measurements, we have to align EBT Gafchromic© film

pieces as well as marks on the phantom with the crosshair of the light field of the Linac. We estimate that our film alignment could be off by δ=0.5 mm for dose profiles. For PDD measurements instead, we estimate a higher uncertainty of δ=1 mm, because the EBT Gafchromic© film is slippery and difficult to position accurately. In fact, in this case the film is sandwiched vertically between two solid water blocs with a water equivalent gel applied at the interfaces to minimize air cavities. Therefore, we evaluate the error in the film positioning at depth z (for PDDs) or coordinate z (for profiles) by taking the average of the differences between the dose $D(z)$ at depth z and the doses at the adjacent depth/coordinates $D(z-\delta)$ and $D(z+\delta)$ located at the distance δ from z, i.e.,

$$\sigma_{pos}(z) = \frac{1}{2}\left[\,|\, D(z) - D(z-\delta)\,| + |\, D(z) - D(z+\delta)\,|\right].$$

This translates into a larger dose uncertainty in sharp dose gradient regions.

Finally, the total uncertainty is the quadratic sum of all uncertainties:

$$\sigma_{tot}(z) = \sqrt{\sigma_{res}^2 + \sigma_{EBT}^2 + \sigma_{out}^2 + \sigma_{pos}^2}\ .$$

5.6 Results for uniform water phantoms

Since all our measurements and calculations are done with solid water, it is natural to use solid water instead of liquid water for evaluating dosimetry functions such as percent depth dose (PDD) and dose profiles. In this section, we compare percent depth doses (PDDs) and dose profiles from MC and Eclipse© MC calculations with measurements for uniform solid water phantoms. CLINAC 21EX electron beams ranging from 6 to 16MeV are used and all measurements are done using EBT Gafchromic© films.

5.6.1 The percent depth dose (PDD)

PDDs are measured in solid water by sandwiching a piece of EBT Gafchromic© film between solid water blocs and positioning the whole set as shown in Figure 5.6, with the median line of the film in coinciding with the beam central axis. The top phantom surface and the top edge of the film are positioned at SSD=100 cm.

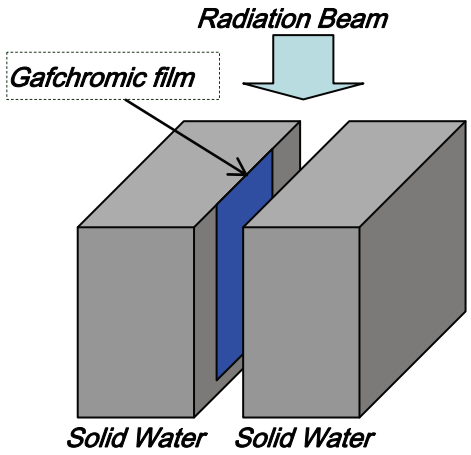

Figure 5.6: *Solid water phantom setup for PDD measurements. The EBT Gafchromic© film is sandwiched between two solid water blocs and the beam is incident vertically on the film. The whole set is positioned such that the median line along the film (where the PDD will be read) coincides with the central axis of the beam. Mechanical clips are used to squeeze the film within the solid water blocs in order to reduce air cavities at the interfaces.*

When the film is sandwiched between solid water phantoms, small air cavities exist at the interfaces between the phantom and the film. Such air cavities may have a non-negligible effect on the measured dose, particularly for electron beams. To minimize this effect, we apply a water equivalent gel at the interfaces between the film and the phantom.

The major source of uncertainty in the measurement comes from uncertainties in positioning the film such that its top edge is at SSS=100 cm and aligned with the top surface of the two squeezing solid water blocs. Using water gel makes things worst as the film becomes slippery and tends to move when the solid water blocs are pressed against each other to squeeze the film. Note also that the film

dimensions in all direction are made larger than the range of electrons in water. This prevents effects of lateral electronic disequilibrium on the central region of the film where the recorded dose is read.

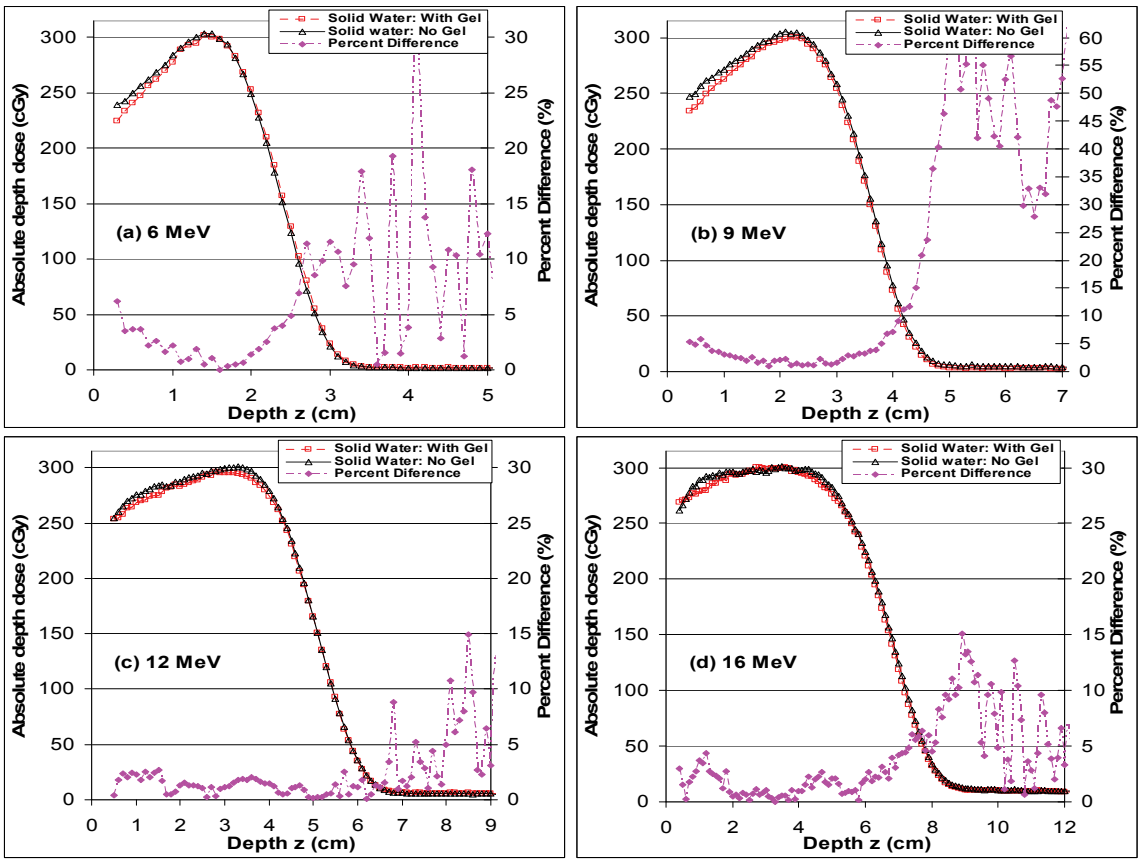

Figure 5.7: *Absolute depth dose curves in solid water for various electron beam energies, measured with and without an applied water equivalent gel. All measurements are done using EBT Gafchromic© films with the setup illustrated in Figure 5.6. 300 MUs are set on the linac and a 10x10 cm² applicator with a standard cutout is used.*

The absolute depth dose (in cGy) measured in solid water with and without a water equivalent gel are shown in Figure 5.7 for various electron beam energies. All plots in Figure 5.7 indicate a maximum dose of about 300 cGy at the depth of dose maximum. This is expected given the 300 MUs given on the phantoms and the usual linac calibration at 1 cGy per MU at the depth of dose maximum. Except for the surface dose and the bremsstrahlung tail, results obtained with and without a gel agree within 3% or less. Discrepancies as high as 5% exist in

the buildup region. This is the region most affected by uncertainties in positioning the top edge of the film and its alignment with the top phantom surface. Much larger uncertainties found in the bremsstrahlung tail are essentially the result of low signal to noise ratio on the films.

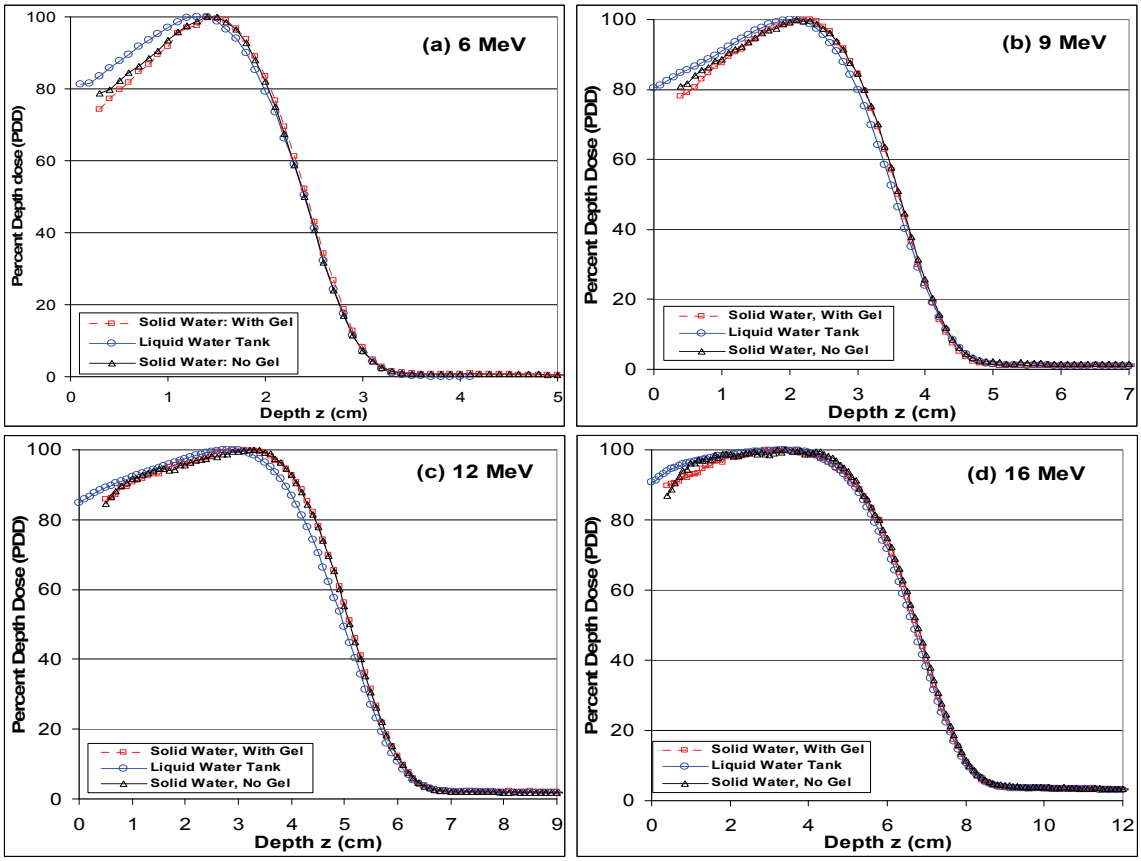

Figure 5.8: *Percent depth dose (PDD) measured in a liquid water tank compared with the PDD measured in solid water using EBT Gafchromic© films and the setup shown in Figure 5.6.*

The PDDs are extracted from the absolute depth dose measurements are shown in Figure 5.7 and compared in Figure 5.8 with the PDDs measured in liquid water using an IC10 chamber. Substantial discrepancies are found in the buildup region between solid water and liquid water measurements; these are more pronounced (as high as 10%) for lower energies (6 meV and 9 meV). The exact cause of these discrepancies is not clear. Some may be due to the fact that EBT Gafchromic films may not be adequate for surface dose measurements near the buildup region where electronic equilibrium is not established. Some may be due

to the higher resolution of EBT Gafchromic films compared to the relatively large volume (inner radius of 1.5 mm) of the cylindrical IC10 chamber used in water. There may be some issue related to the difference in properties between liquid water and the solid water used, which could be exacerbated at lower energies, especially given the age of the phantom. In short, this matter needs further investigation. However, beyond the depth of dose maximum d_{max}, the distance to accuracy is about 2 mm, i.e., within acceptable limits [5].

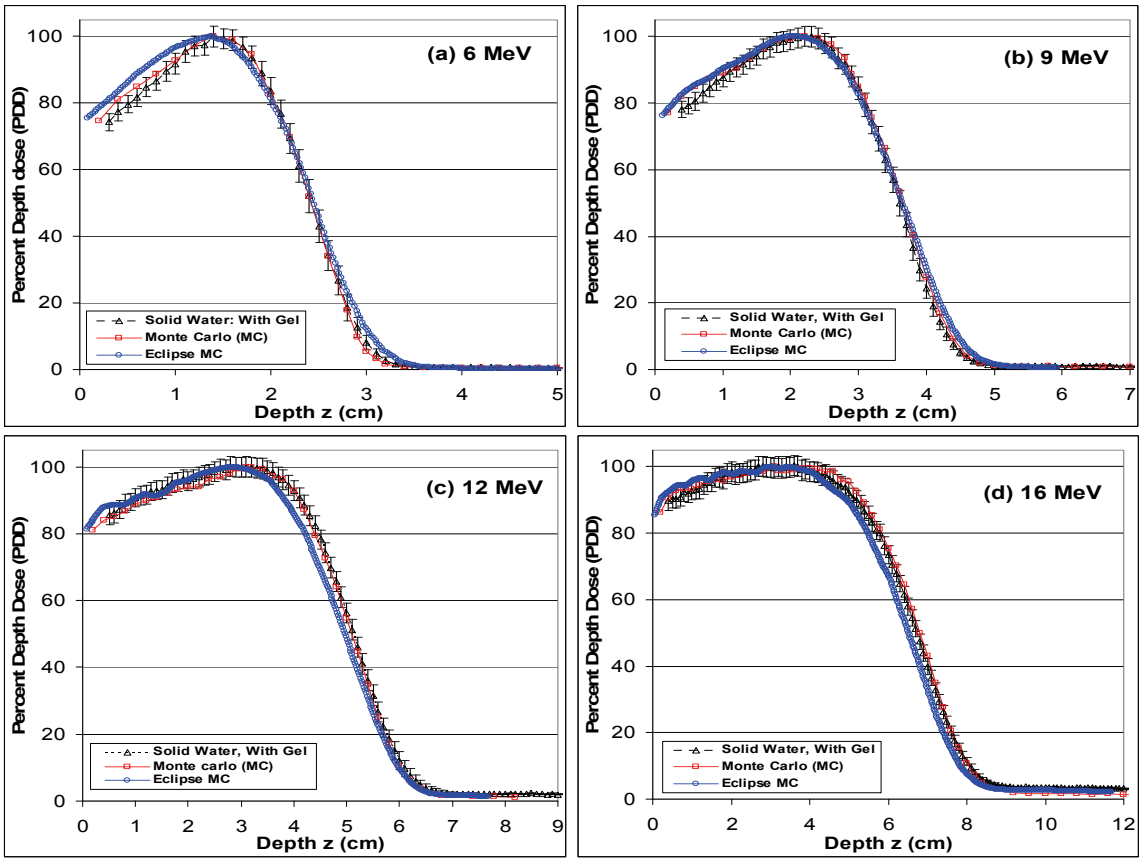

Figure 5.9: *PDD measured in a solid water phantom using EBT Gafchromic© films vs. MC and Eclipse MC calculations in solid water. A 10x10 cm² applicator is used with SSD=100 cm. Error bars in solid water PDD measurements are obtained as described in Section 5.5.*

A comparison of PDDs obtained from MC and Eclipse MC with measurements in solid water is illustrated in Figure 5.9. It appears that MC results agree better with measurements is solid water than with those in liquid water. This supports our assertion earlier that there may be substantial differences between solid water

and liquid water or that EBT Gafchromic films with their higher spatial resolution are better than the IC10 ionization chamber used. MC simulations agree with measurements within 3%, except in the buildup region where discrepancies can be as high as 5%. This agreement of MC with measurements is better than that of Eclipse MC where higher discrepancies are found, especially in the buildup region and in the PDD's dose falloff region. Given that the best agreement between MC and Eclipse MC in the PDD is found near the depth of dose maximum, our subsequent evaluation of Eclipse will focus near this depth where Eclipse MC performance is the best.

5.6.2 Dose profiles

Our next step in the evaluation of Eclipse© MC is for dose profiles in uniform phantoms. In this case, air cavities are not much an issue because a uniform flat phantom surface is presented to the incident beam, with a Gafchromic film pressed under a piece of solid water at a specific depths. Figure 5.10 shows dose profiles for various electron beam energies at various depths. The depths selected for dose measurements are close to the calibration reference point for each energy beam. 200 MU are set on the linac in each case, and since the linac output is usually about 1 cGy per MU at the reference point (including daily variations of the output), one sees that the central axis dose in all plots in Figure 5.10 is close to 200 cGy as expected. It also appears from Figure 5.10 that MC agrees better with measurements than Eclipse MC. Relative differences between MC and measurements are about 2% or less, while they are about 5% or less between Eclipse MC and measurement.

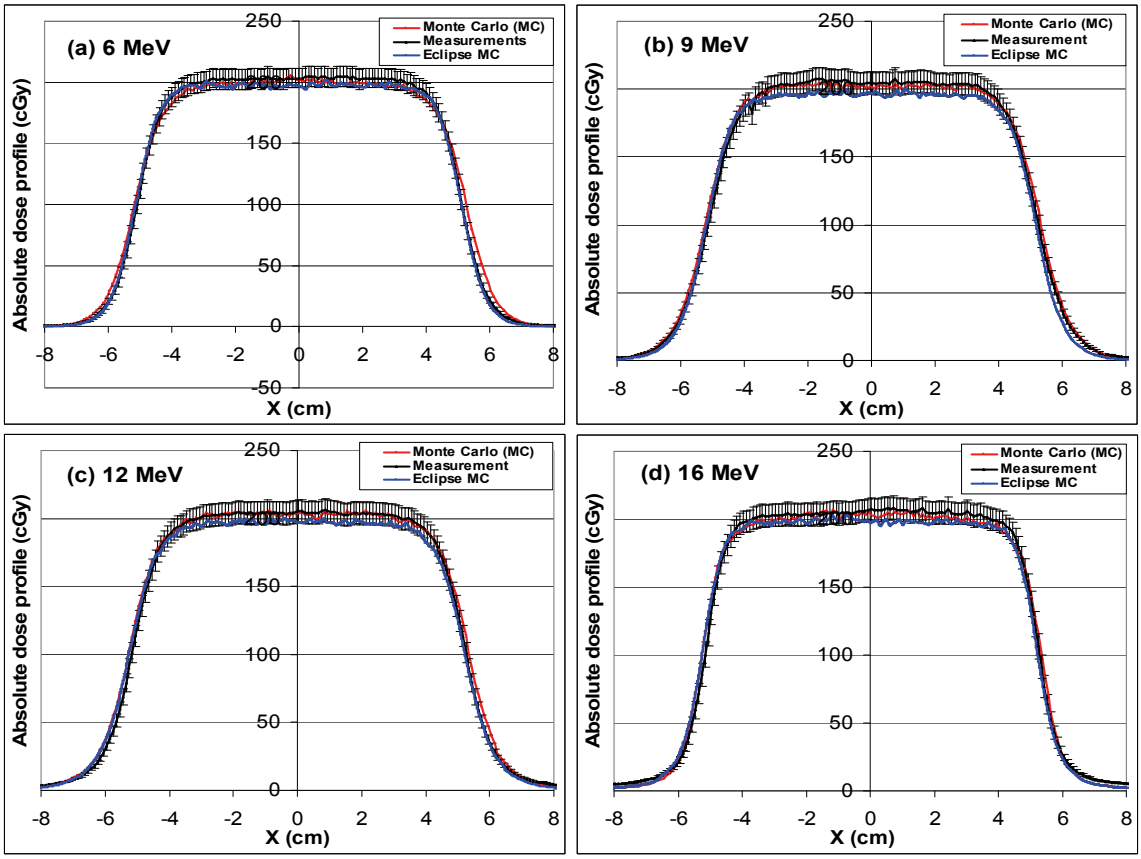

Figure 5.10: *Absolute dose profiles in uniform solid water for various electron beam energies and depths: (a) 6 MeV beam for depth 1.5 cm; (b) 9 MeV beam for depth 2.5 cm; (c) 12 MeV beam for depth 3.0 cm; (d) 16 MeV beam for depth 3.0 cm. In each case, 200 MUs are given at SSD=100 cm using a 10x10 cm² applicator. Error bars are obtained as described in Section 5.5.*

5.7 Results for "two-bars" heterogeneous phantom

In this section, we evaluate Eclipse MC by comparison with measurements and with MC simulations for the two-bars phantom whose cross-section is illustrated in Figure 5.2 and at the top of Figure 5.11, Figure 5.12 and Figure 5.14. The heterogeneity bars have 2x2 cm² section and are sandwiched in solid water blocs of 3 cm height, so that there is a 2 cm wide and 1 cm deep air gap between the top of the bar and the surface of the phantom (see Figure 5.11). In the two-bars phantom illustrations at the top of Figure 5.11, Figure 5.12 and Figure 5.14, the horizontal dashed line shows where the film is placed for measurement at a

depth 3.2 cm from the phantom surface, i.e., 2 mm under the bars. Unless stated otherwise, a water equivalent gel is applied at the interfaces between heterogeneity bars and solid water blocs for all “two-bars” dose profile measurements in order to minimize the effects of air cavities.

5.7.1 The “two-bars” lung-lung heterogeneous phantom

Here, we first consider the two-bars phantom with both bars being lung tissue equivalent. Results for MC, Eclipse MC and measurements are summarized in Figure 5.11 for 6, 9, 12, and 16 MeV beams. An illustration of the cross-section of the phantom is given at the top of Figure 5.11.

Results show that under the bars (and air gap), which are lower density material compared to water, dose rises sharply. This is due to the smaller stopping power for lung tissue (and air gap) compared to solid water (see stopping powers in Figure 2.3), which allows more electrons to pass through and deposit dose at depth 3.2cm on the film. At the interface between solid water and bars, there is a sharp dose gradient in the profile, which reflects the sharp change in tissue density from water to lung (and air gap). For lower energy beam, the peak in the profile is very smooth (see Figure 5.11 (a) and (b)). However, as the beam energy increases, sharp edges increasingly appear on the sides of the peak in the dose profile (see Figure 5.11(c) and (d)). These are due to electrons scattered at the edges of the solid water phantom near the interface with the bars: At lower beam energies such electrons are scattered with energy too low to reach the depth of 3.2 cm at which the profile is investigated. In contrast, for higher beam energies, the scattered electrons can reach the above mentioned depth, leading to the sharp edges in the dose profile.

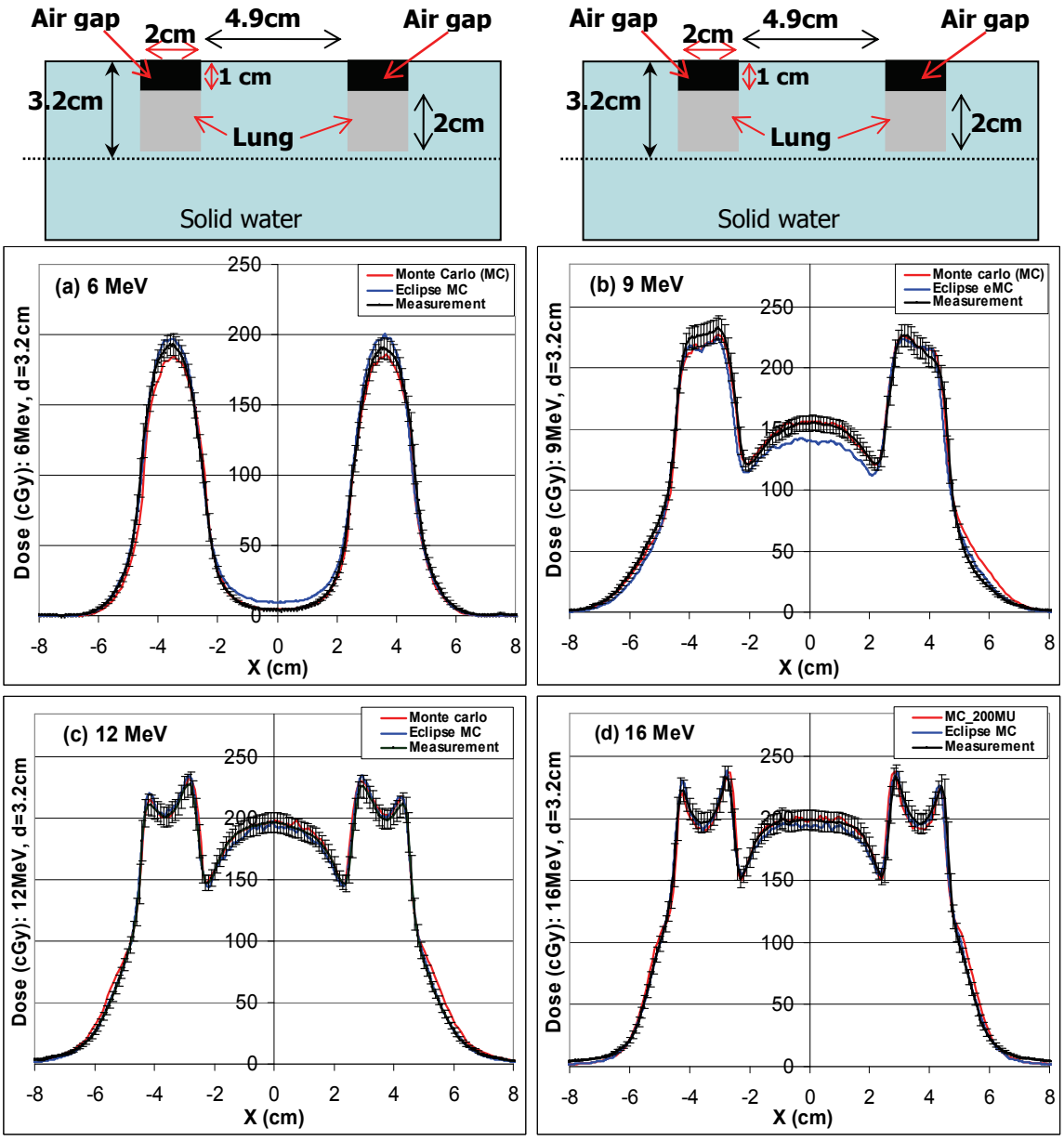

Figure 5.11: *Comparison of MC and Eclipse MC calculations with measurements for various electron beam energies using the "two-bars" phantom with lung tissue equivalent bars:* ***(a)*** *6 MeV;* ***(b)*** *9 MeV;* ***(c)*** *12 MeV;* ***(d)*** *16 MeV. 200 MU are given to the phantom at SSD=100 cm with a 10x10 cm² applicator. Error bars in the measurement are obtained as described in Section 5.5.*

Regarding the comparison of MC and Eclipse MC with measurements, it appears from Figure 5.11 that in general both results agree quite well with measurement, but MC calculations agree better with measurements (relative differences of about 4% or less) than Eclipse MC results. Disparities between Eclipse MC and

measurements are as high as 9% and occur essentially below tissue heterogeneities. Table 5.2 shows estimated maximum percent differences between measurements and calculations for various beam energies. Note however that the overall accuracy achieved by Eclipse MC is rather impressive, given the remarkable speed of Eclipse MC compared to MC. It is also remarkable that the two calculations agree well with each other and with measurements for 6 MeV beam, given that the depth of 3.2 cm is almost in the bremsstrahlung tail of the electron PDD.

Beam Energy	Eclipse MC vs Measurements	MC vs Measurements
6 MeV	4.2%	4.4%
9 MeV	9.2%	0.7%
12 MeV	2.9%	1.5%
16 MeV	6.0%	1.5%

Table 5.2: *Summary of estimated maximum percent differences between measurements and each of the two MC simulations (Eclipse MC and full MC), for the two-bars lung-lung phantom. In this estimation we ignore regions of small dose, and of high dose gradients where accuracy is better described by the distance to agreement (see discussion in Section 5.9).*

We now attempt to assess the importance of accounting for tissue heterogeneity in dose calculations. We use MC calculations for this assessment, as they agree better with measurements. We report in Figure 5.12 full MC simulations for the physical phantom with lung tissue bars, and the same calculation with lung tissue bars replaced by solid water bars (the air gaps remains in place). In other words, we assume that lung tissue in the phantom is just water. It appears from Figure 5.12 that replacing lung tissue by solid water tissue lowers the dose profile in the region under the bar, as water has a higher stopping power than lung tissue. Also the strength of this effect is stronger for lower beam energy: For 6 MeV electron beam (Figure 5.12 (a)) ignoring the lung heterogeneity (i.e., treating lung tissue as water) leads to an underestimation of dose as high as 30%. The picture is

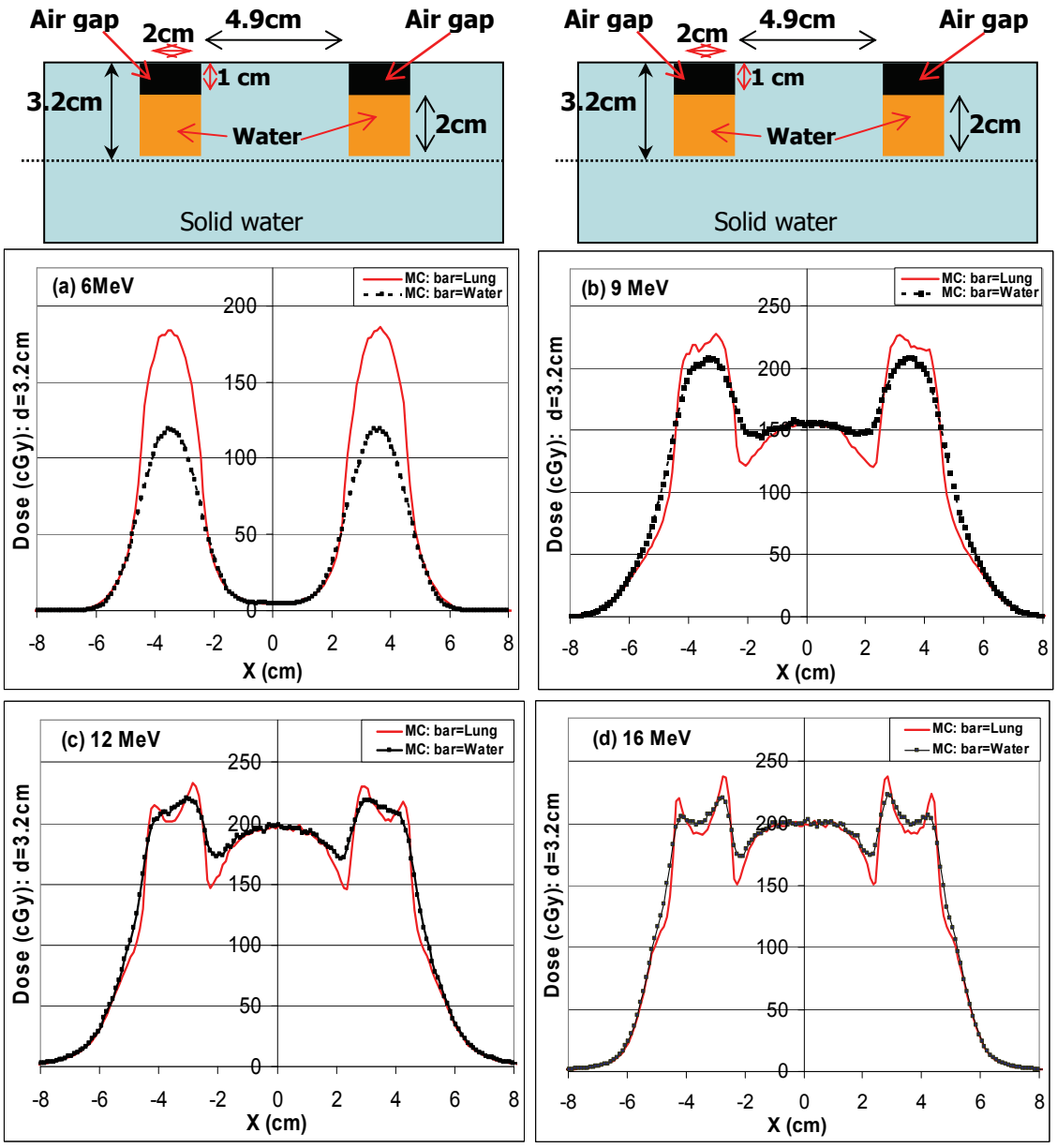

Figure 5.12: *MC absolute dose profiles at depth d=3.2cm for the "two-bars" phantom with lung tissue bars (thick dots) compared to the same calculation with lung bars replaced by solid water (solid line): (a) 6 MeV; (b) 9 MeV; (c) 12 MeV; (d) 16 MeV. 200 MU are given to the phantom at SSD=100 cm with a 10x10 cm² applicator.*

mixed for higher energies (9 – 16 MeV) where ignoring the lung heterogeneity leads to both underestimation and overestimation of doses as high as 16%, depending on the area of the profile. This clearly indicates that neglecting tissue heterogeneities is a large approximation in electron beam dose calculation for radiotherapy purposes. Note also that the dose profiles are smoother when the

lung heterogeneity bar is replaced by water, as sharp edges near the peak of the profiles are no longer present. This is due to the fact that when lung bar is replaced by water more electrons scattered at the edges of the phantom near the bars are stopped in the higher density solid water bars as compared to lung bars.

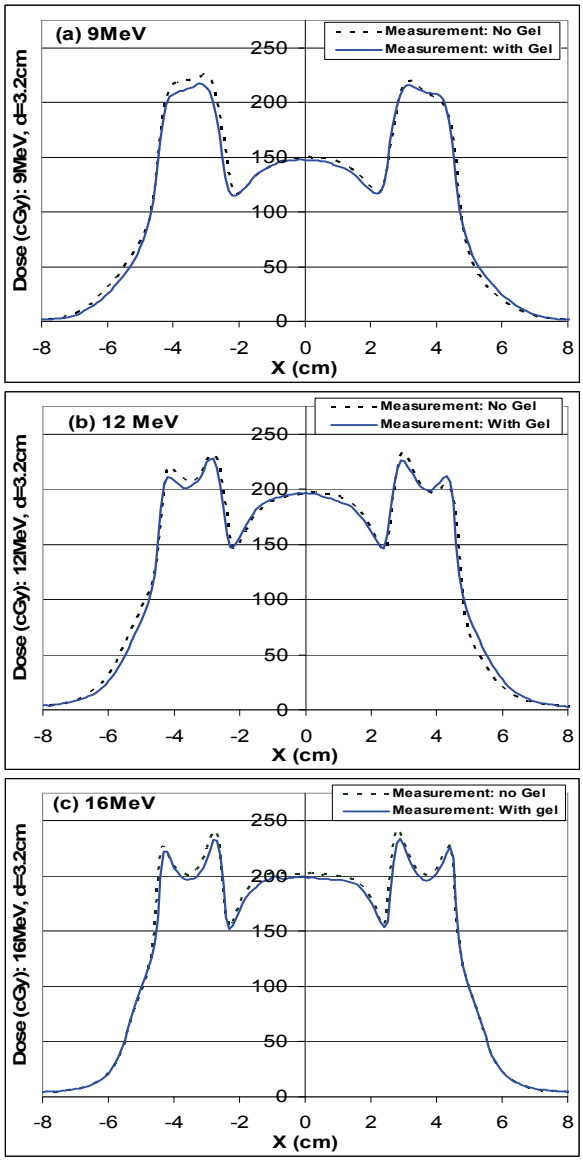

Figure 5.13: *Absolute dose profiles measured for various beam energies (9 MeV in (a), 12 meV in (b), and 16 MeV in (c)) at 3.2 cm depth in the "two-bars" phantom with lung equivalent bars. Each plot shows the profile measured with and without a thin layer of water equivalent gel applied at interface between lung bars and solid water blocs.*

As mentioned earlier, there may be air cavities at the interface of the bars and the solid water blocs in the “two-bars” phantom. Figure 5.13 shows dose profile measurements (for various beam energies) at depth of 3.2 cm with and without a thin layer of water equivalent liquid gel applied at the interface. Substantial differences (as high as about 5%) between the two measurements occur near the heterogeneities and illustrate the fact that there are indeed air cavities at the interfaces. Also, as expected, dose is in general lower when the gel is applied.

5.7.2 The “two-bars” Bone-Lung heterogeneous phantom

In this section, we consider the same phantom as in the previous section, but with one of the two lung bars replaced by bone-tissue. The phantom cross section and the absolute dose profiles at 3.2 cm depth are shown in Figure 5.14.

Under the lung tissue bar, there is an increase in dose due to the lower stopping power of the combined lung tissue bar and air gap. In contrast, the dose profile under the bone bars shows a sharp decline due to the higher stopping power of bone tissue compared to solid water. Overall, MC and Eclipse MC results agree with measurements, but once again MC does better. Yet substantial difference (as high as 18% for 9 MeV) between both MC and Eclipse MC with measurement can be found in very low dose area under bone tissue. It is not clear why highest discrepancies between Eclipse MC and measurements are found for the 9MeV beam. This matter needs further investigation.

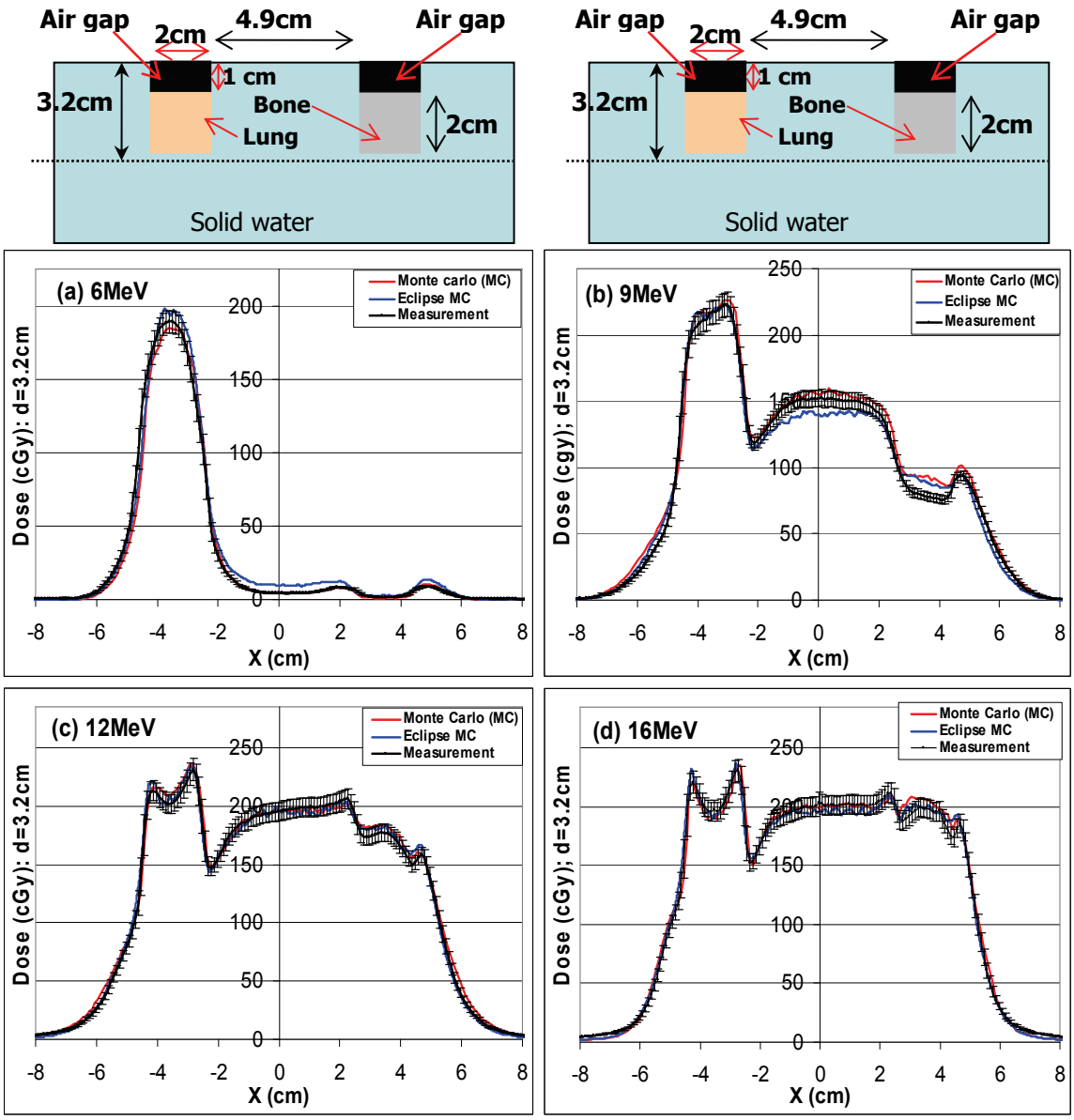

Figure 5.14: *Comparing absolute dose profiles from MC and Eclipse MC calculations with measurements at depth d=3.2 cm, for various beam energies using the "two-bars" lung-bone phantom: (a) 6 MeV; (b) 9 MeV; (c) 12 MeV; (d) 16 MeV. 200 MU are given to the phantom at SSD=100 cm with a 10x10 cm² applicator. Error bars are obtained as described in Section 5.5.*

For various beam energies, Table 5.3 summarizes for various beam energies the maximum percent differences between measurements, and Eclipse MC and full MC calculations for the two-bars bone-lung phantom discussed above.

Beam Energy	Eclipse MC vs Measurements	MC vs Measurements
6 MeV	3.2%	2.3%
9 MeV	10.0%	4.2%
12 MeV	3.9%	4.1%
16 MeV	4.6%	4.0%

Table 5.3: *Summary of estimated maximum percent differences between measurements and each of the two MC simulations (Eclipse MC and full MC), for the two-bars bone-lung phantom. In this estimation we ignore regions of small dose, and of high dose gradients where accuracy is better described by the distance to agreement (see discussion in Section 5.9).*

5.8 Results for "three-bars" heterogeneous phantom

The "three-bars" phantom consists of three rectangular bars of tissue of various densities separated by air gaps, as illustrated at the top of Figs. Figure 5.15, Figure 5.16, Figure 5.17, Figure 5.18, Figure 5.19, and Figure 5.20. In all these figures, the dashed line shows the depth at which EBT Gafchromic films are inserted for dose profile measurements. Thus in this case, there is a much sharper change in density at the interface between tissue heterogeneities, which makes dose calculations more challenging. Note also that there is no issue in this case regarding air cavities at the interface between tissue heterogeneities.

5.8.1 The "three-bars" Bone-Bone-Bone phantom

In this case, a cross section of the phantom is illustrated in Figure 5.15(a), where the three bars have tissue equivalence to bone (B). The air gap between the bars is Δ=1 cm and the dose profile is calculated (MC and Eclipse MC) and measured at depth d=3.0cm from the top surface of the phantom.

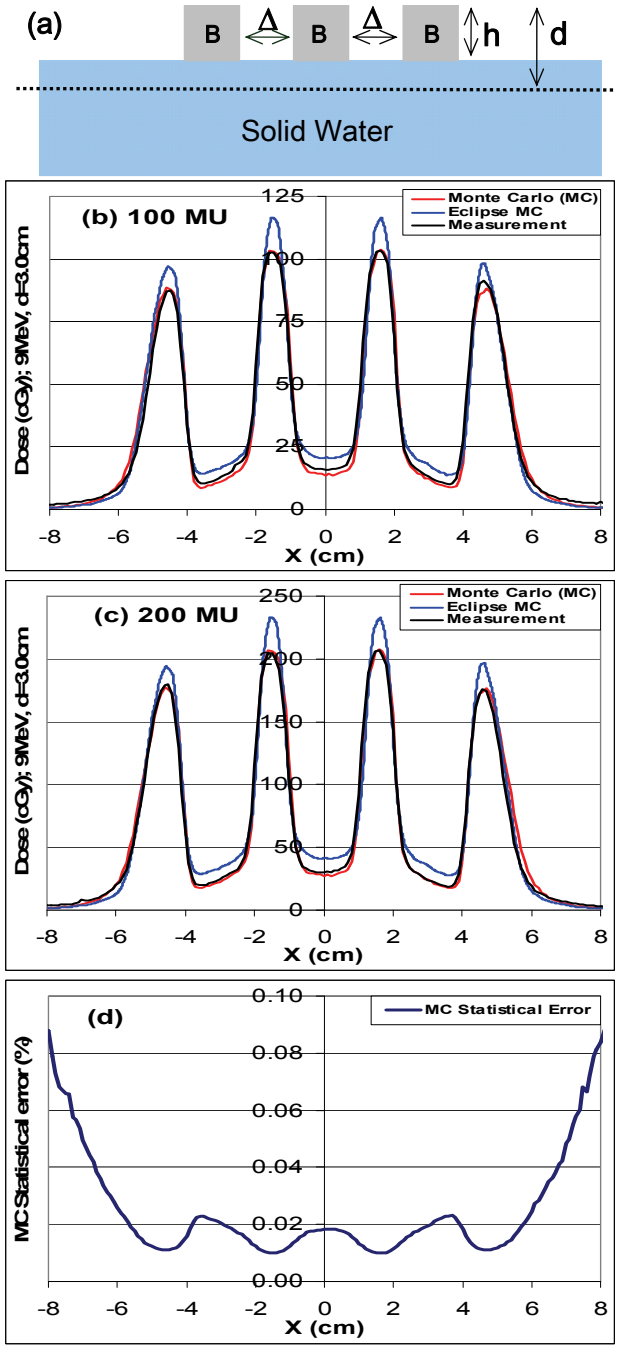

Figure 5.15: (a) *Cross-section of the "three-bars" phantom with Δ=1 cm, h=2 cm and d=3.0 cm. Absolute dose profiles (in cGy) for:* ***(b)*** *100 MU and* ***(c)*** *200 MU given. In each case, results form MC (red curve), Eclipse MC (blue curve) and measurements are displayed. SSD=100 cm is used with a 10x10 cm² applicator. The statistical error in the MC simulation is illustrated in* ***(d)****.*

For 100 MUs and 200 MUs given, absolute dose profiles from MC and Eclipse MC calculations are plotted along side with measurements in Figure 5.15(b) and Figure 5.15 (c), respectively. The profiles show a minimum in the dose profile under the bone slabs and a maximum in the dose profile under the air gap, which is due to the higher stopping power of bone relative to air. There is also sharp dose gradient at the interface between bone and air, which reflects the rapid change in tissue heterogeneity in that region. It is quite remarkable that this sharp dose gradient is well reproduced by both MC and Eclipse MC calculations. However, results from MC simulations show a better agreement with experiments, with relative differences better than 4% except in very low dose area and in high dose gradient. The reason for larger relative differences in very low dose and high dose gradient areas in both cases (i.e., MC relative to measurements and Eclipse MC relative to measurements) is discussed in Section 5.9. Even in area with a high dose and a negligible dose gradient, significant disagreements of Eclipse MC with measurements are found to be as high as 14%, especially in regions under heterogeneity bars.

To reiterate, the accuracy in Eclipse MC is set to 1% (the best available on Eclipse) throughout our calculations. However, the statistical uncertainty in the MC dose calculation, illustrated in Figure 5.15 (d), indicates that the uncertainty in the dose profile is well below a fraction of 1%. This is due to the large number of particle histories (120 million) used in the MC calculation, as well as the appropriately chosen voxel size as discussed in Section 5.4.

Results for the bone-bone-bone phantom are summarized in Figure 5.16 for various beam energies, and for 200 MUs given to the phantom for each energy. Similar features as from Figure 5.15 can be pointed out, namely the presence of a very sharp dose gradient near the interfaces between bone bars and air gap, the minima in the dose profile under bone bars and maxima under air gaps, as well as the fact that in general MC calculations agree better with measurements

than Eclipse MC results do. Relative differences between Eclipse MC and measurements away from sharp dose gradients can be as high as 40% in very low dose portions of the profile, whereas between MC and measurements relative differences tend to be at most about 10% for very low dose portions of the profile. As the beam energy increases, it appears that there is no clear advantage for either MC or Eclipse MC.

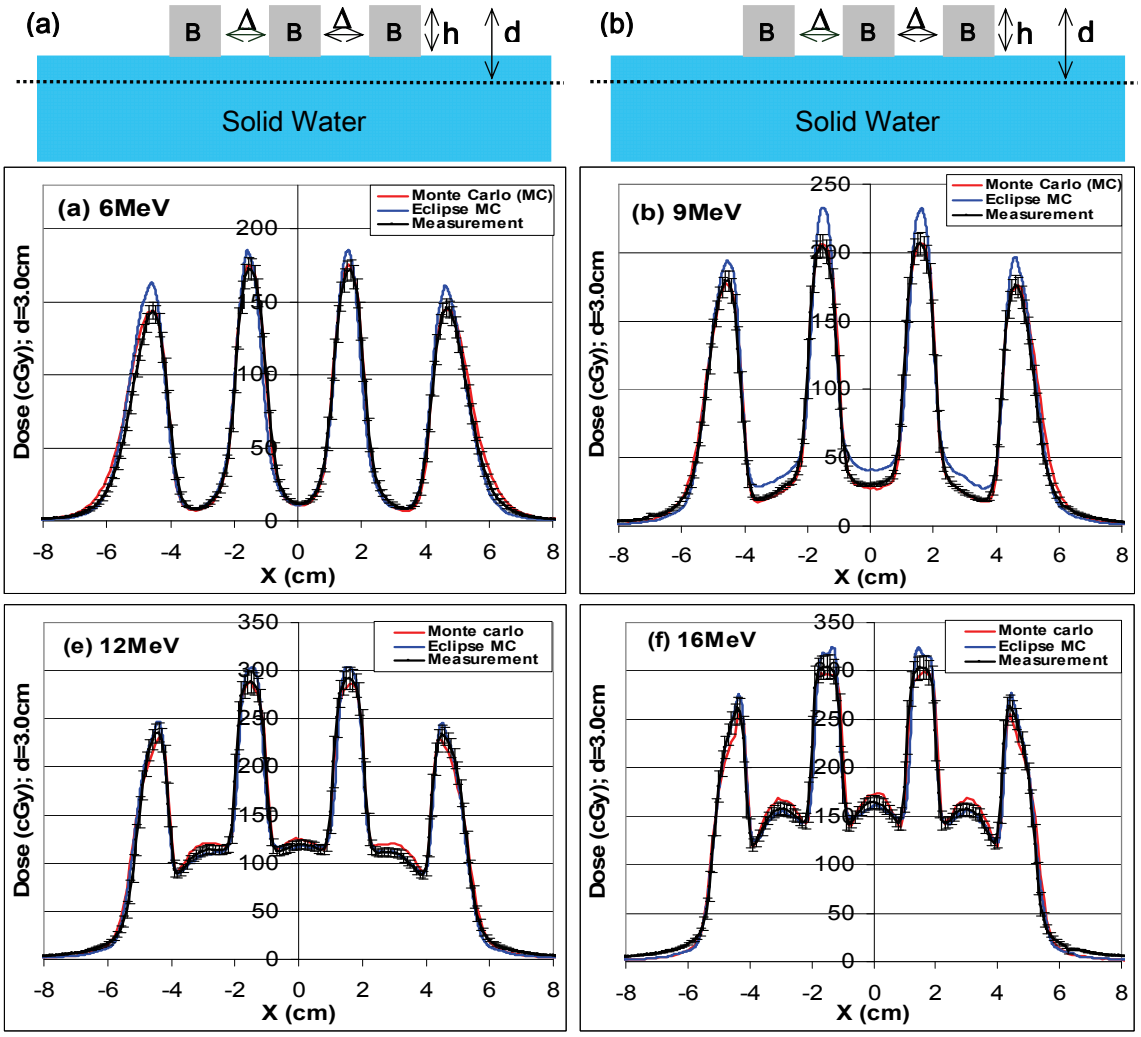

Figure 5.16: *Absolute dose profiles (in cGy) at depth d=3.0 cm for the "three-bars" bone-bone-bone phantom (see cross-sections in* ***(a)*** *and* ***(b)****) with Δ=1 cm, and h=2 cm, for various electron beam energies:* ***(c)*** *6 MeV;* ***(d)*** *9 MeV;* ***(e)*** *12 MeV,* ***(f)*** *16 MeV. In each case, MC and Eclipse MC results, as well as measurements are plotted. SSD=100 cm is used with a 10x10 cm² applicator. Error bars are obtained as described in Section 5.5.*

As discussed in Section 5.9, relative differences with respect to measurements for each of the two calculations in very low dose region (as well as very high gradient area) can be misleading and are not much clinically relevant, as such doses are very small and correspond to area outside of the planning target volume (PTV). In large dose area near the dose peaks where relative doses are meaningful, MC calculations agree with measurements to within 3% or less, while relative differences between Eclipse MC results and measurements can be as high as 15%. An extensive discussion of the relative difference between calculations and measurements near the sharp dose gradient portion of the profile shall be presented in subsequent sections. A summary of maximum percent differences between measurements and calculations is given in Table 5.4 for various beam energies.

Beam Energy	Eclipse MC vs Measurements	MC vs Measurements
6 MeV	13.2%	0.7%
9 MeV	12.0%	2.1%
12 MeV	5.2%	2.0%
16 MeV	4.2%	2.6%

Table 5.4: *Summary of estimated maximum percent differences between measurements and each of the two MC simulations (Eclipse MC and full MC), for the three-bar bone-bone-bone phantom. In this estimation we ignore regions of small dose, and high dose gradients where accuracy is better described by the distance to agreement (see discussion in Section 5.9).*

5.8.2 The “three-bars” Lung-lung-Lung phantom

The phantom considered here is the same as in the previous section with bone bars replaced by lung (L) tissue bars. A cross section of the phantom is illustrated in Figure 5.17(a)-(b), and the absolute dose profiles at depth d=3.0 cm

from the phantom surface are plotted in Figure 5.17. In each case shown in this figure, we use the same electron beam energy and number of monitor units as in Figure 5.16, as well as the same SSD and applicator.

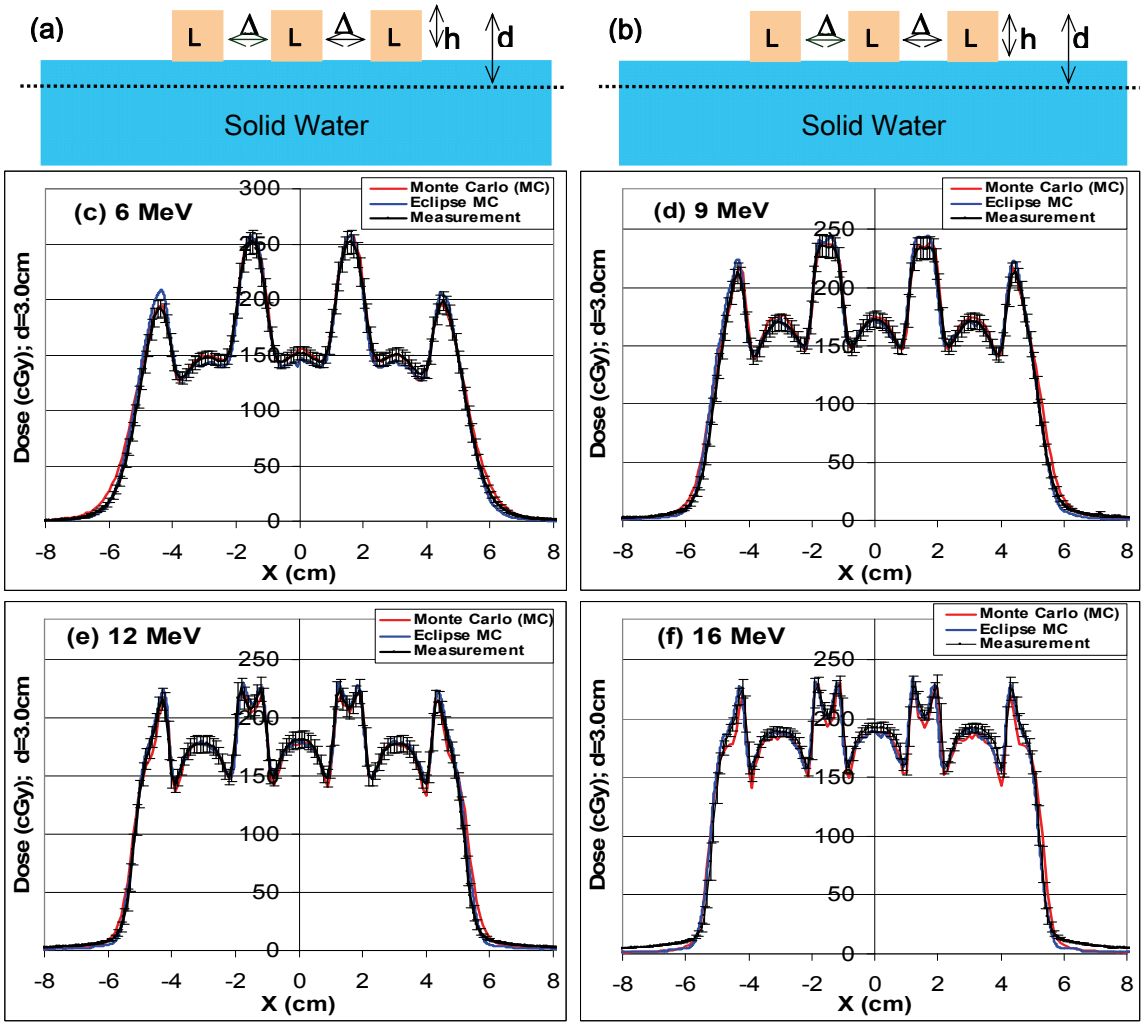

Figure 5.17: *Absolute dose profiles (in cGy) at depth d=3.0 cm for the "three-bars" lung-lung-lung phantom (see cross-section in (a) and (b)) with Δ=1 cm, and h=2 cm, for various electron beam energies: (c) 6 MeV; (d) 9 MeV; (e) 12 MeV, (f) 16 MeV. In each case, 200 MUs are given, and results from MC and Eclipse MC, as well as measurements are plotted. Error bars are obtained as described in Section 5.5.*

Results in Figure 5.17 and those for bone in Figure 5.16 show minima in area under the lung bars, reflecting the higher stopping power of lung tissue relative to air. In addition, these minima are shallower for lung tissue in Figure 5.17 than for bone in Figure 5.16, reflecting the higher stopping power of bone relative to lung

tissue. Once again, Figure 5.17 indicates that MC results agree better with measurements (within 3%) than Eclipse MC does, as the latter can depart from measurements by as much as 9% (i.e., better than bone is Section 5.7.1). With increasing energy, there is no clear advantage for MC over Eclipse MC. For various beam energies, Table 5.5 shows estimated maximum percent differences between measurements and calculations.

Beam Energy	Eclipse MC vs Measurements	MC vs Measurements
6 MeV	7.3%	1.6%
9 MeV	3.8%	2.8%
12 MeV	3.5%	1.9%
16 MeV	3.4%	3.0%

Table 5.5: *Summary of estimated maximum percent differences between measurements and each of the two MC simulations (Eclipse MC and full MC), for the three-bar lung-lung-lung phantom. In this estimation we ignore regions of small dose, and high dose gradients where accuracy is better described by the distance to agreement (see discussion in Section 5.9).*

5.8.3 The "three-bars" Lung-Bone-Lung phantom

In this case, two lung (L) bars and one bone (B) bar are combined as illustrated in Figure 5.18(a)-(b); lung first, bone next and a lung last. The air gaps are Δ=1 cm. Simulations and measurements are done for a 200 MU setting on the linac, a SSD of 100 cm and a 10x10 cm^2 applicator with a standard cutout. The dose profiles at depth d=3.0 cm for the three approaches in Figure 5.18 show a low dose under lung and bone bars and a maximum under the air gaps. The dose valley under bone is deeper than under lung, a reflection of higher electron density in bone tissue compared to lung. This higher density for bone than lung

leads to fewer electrons going through the bone bar and depositing dose at depth d=3.0cm under the bone bar.

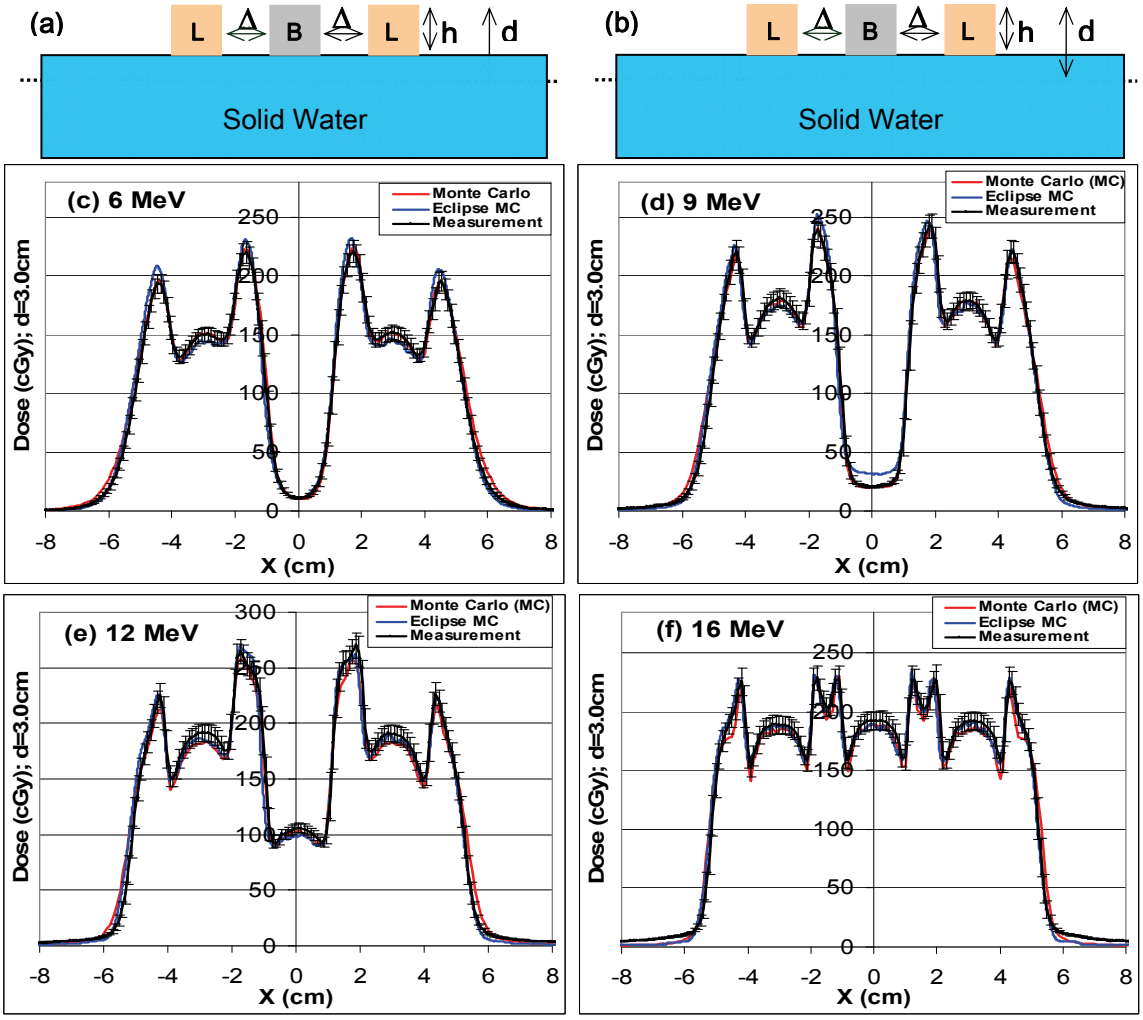

Figure 5.18: *Absolute dose profiles (in cGy) at depth d=3.0 cm for the "three-bars" lung-bone-lung phantom (see (a) and (b)) with Δ=1 cm and h=2 cm, for various electron beam energies: (c) 6 MeV; (d) 9 MeV; (e) 12 MeV, (f) 16 MeV. In each case, results from MC and Eclipse MC, as well as measurements are plotted. See Section 5.5 for details on error bars in measurements.*

An analysis of dose profiles in Figure 5.18 also indicates that except for a few spots MC results have better agreement with measurements than Eclipse MC (see Table 5.6 for estimated largest percent differences between measurements and calculations). Largest discrepancies with measurements occur near the

maxima and near the peaks in the dose profile. Note however that the accuracy of Eclipse MC tends to improve with increasing electron beam energy.

Beam Energy	Eclipse MC vs Measurements	MC vs Measurements
6 MeV	6.7%	1.1%
9 MeV	4.7%	2.1%
12 MeV	4.1%	3.4%
16 MeV	6.7%	3.5%

Table 5.6: *Summary of estimated maximum percent differences between measurements and each of the two MC simulations (Eclipse MC and full MC), for the three-bar lung-bone-lung phantom. In this estimation we ignore regions of small dose, and high dose gradients where accuracy is better described by the distance to agreement (see discussion in Section 5.9).*

5.8.4 The "three-bars" Bone-Lung-Bone phantom

We now consider heterogeneities that consist of successive bars of bone (B), lung (L) and bone tissues, separated by air gaps of width Δ. For a width Δ=1 cm, the corresponding phantom is illustrated in Figure 5.19(a)-(b). Also illustrated in Figure 5.19 is a comparison of absolute dose profiles from the three approaches at depth d=3.0 cm, for various electron beam energies. In order to further challenge MC and Eclipse MC, we also report in Figure 5.20 calculations and measurements for a similar phantom but with a thinner air gap heterogeneity, i.e., with Δ=0.5 cm.

Absolute dose profiles from Figure 5.19 and Figure 5.20 indicate that once again MC results agree better with measurements than Electron MC, especially for lower electron beam energies. At higher energies (12 MeV and 16 MeV), the situation is a little bit balanced, as there are areas in the dose profile where Eclipse MC agrees better with measurements than to MC, as well as those

where MC does better than Eclipse MC compared to measurements. This is well illustrated in table 5.7 that summarizes estimated maximum percentage differences between measurements and calculations. However, when the air gap is decreased as in the case in Figure 5.20 the accuracy of MC results compared to measurements remains nearly unchanged (typically 5% or less), but the disparity between Eclipse MC and measurements increase to reach as high as 14%. This suggests that Eclipse MC has difficulties dealing with dose calculations near smaller and sharper heterogeneities.

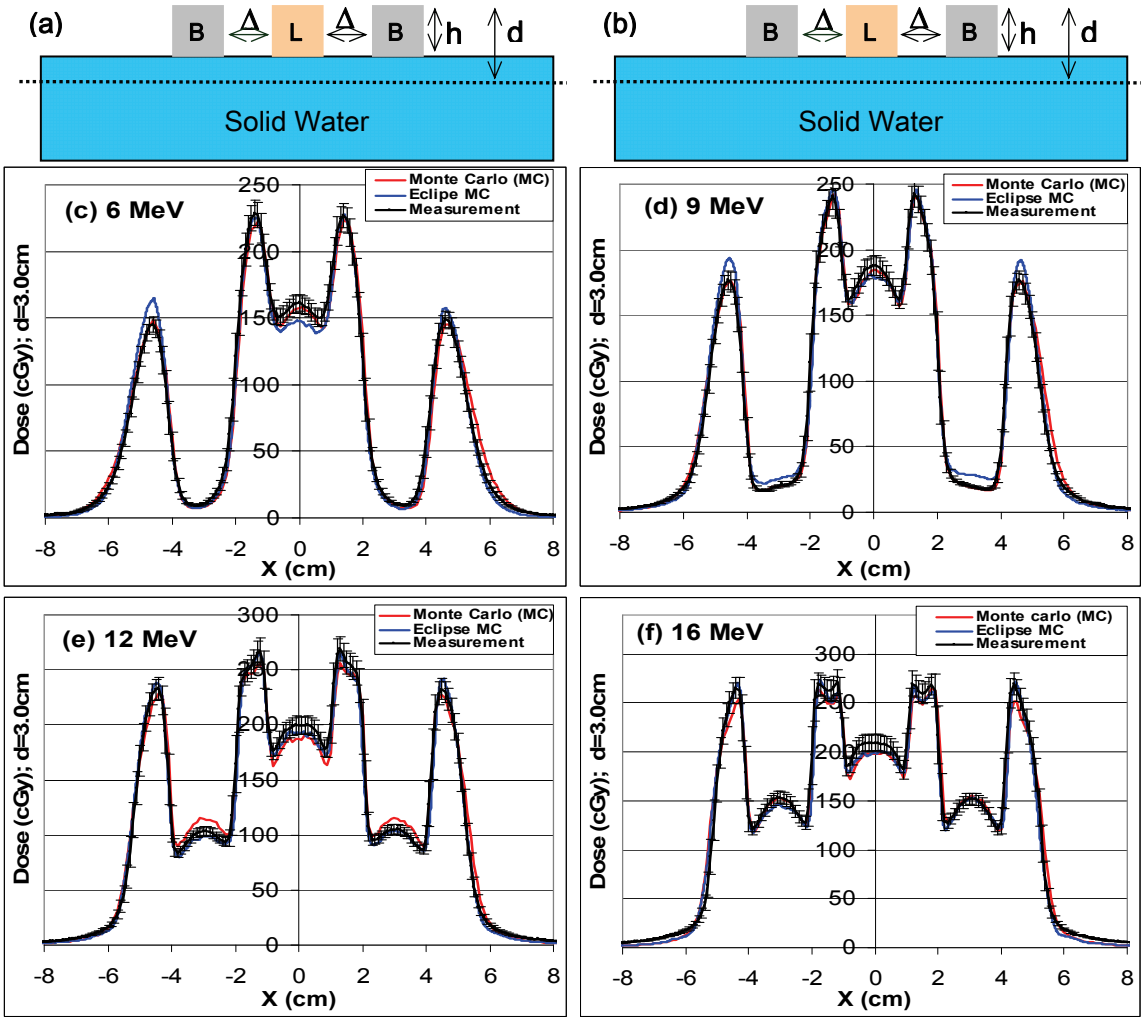

Figure 5.19: *Absolute dose profiles (in cGy) at depth d=3.0 cm for the "three-bars" bone-lung-bone phantom (see (a) and (b)) with Δ=1 cm and h=2 cm, for various electron beam energies: (c) 6 MeV; (d) 9 MeV; (e) 12 MeV, (f) 16 MeV. In each case, results from MC and Eclipse MC, as well as measurements are plotted. See Section 5.5 for details on error bars in measurements.*

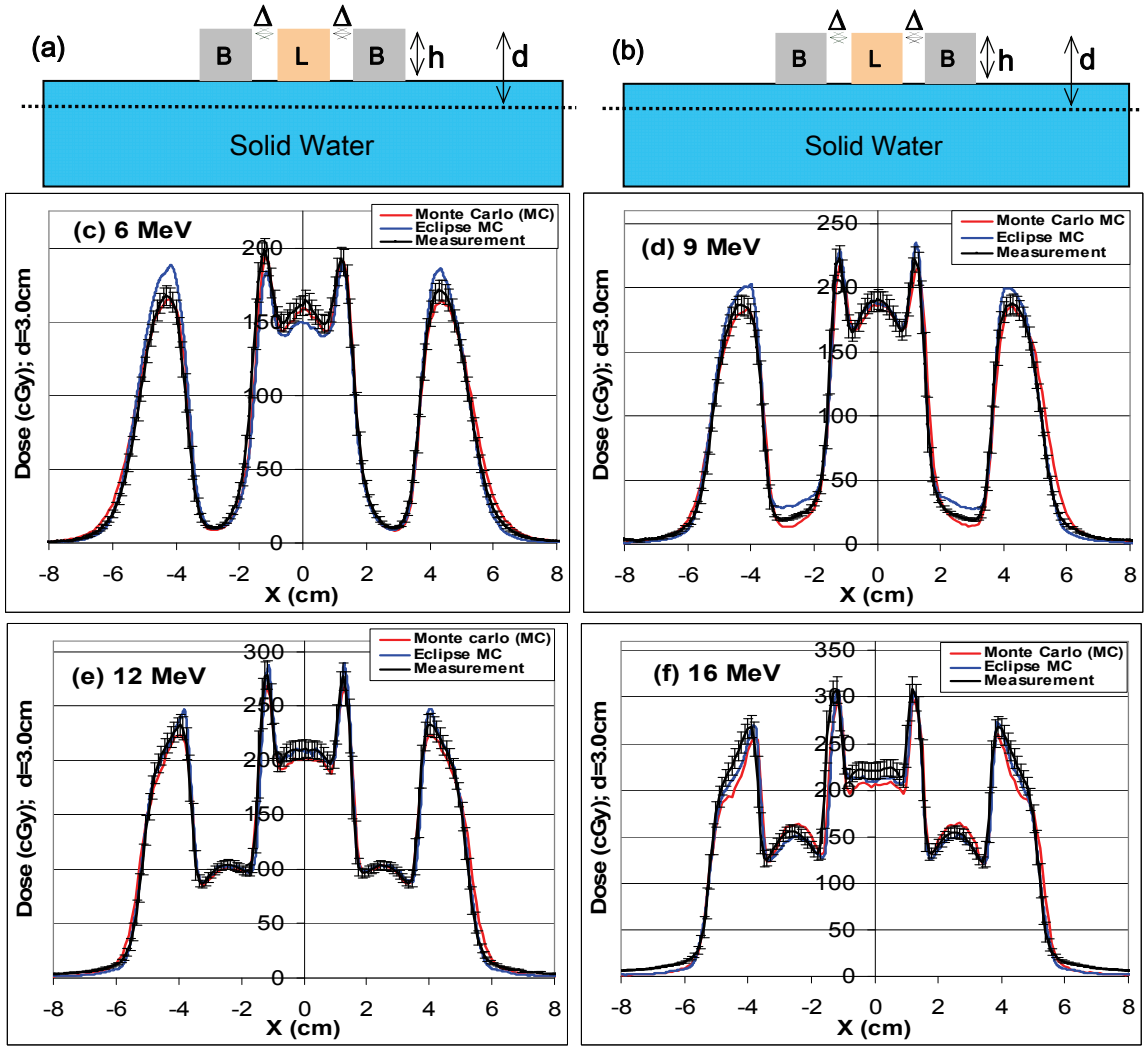

Figure 5.20: *Absolute dose profiles (in cGy) at depth d=3.0 cm for the "three-bars" bone-lung-bone phantom (see (a) and (b)) with a narrower air gap Δ=0.5 cm and h=2 cm, for various electron beam energies: (c) 6 MeV; (d) 9 MeV; (e) 12 MeV, (f) 16 MeV. In each case, results from MC and Eclipse MC, as well as measurements are plotted. Error bars are obtained as described in Section 5.5.*

	Bone-Lung-Bone with a Δ=1 cm gap		Bone-Lung-Bone with a Δ=0.5 cm gap	
Beam Energy	Eclipse MC vs measurements	MC vs measurements	Eclipse MC vs measurements	MC vs measurements
6 MeV	11.4%	4.5%	13.3%	3.6%
9 MeV	8.8%	1.6%	11.4%	3.1%
12 MeV	3.0%	4.3%	4.9%	4.5%
16 MeV	4.9%	4.4%	4.8%	5.1%

Table 5.7: *Summary of estimated maximum percent differences between measurements and each of the two MC simulations (Eclipse MC and full MC), for three-bar bone-lung-bone phantoms with air gaps Δ=1.0 cm (in Figure 5.19) and Δ=0.5 cm (in Figure 5.20). In this estimation we ignore regions of small dose, and high dose gradients where accuracy is better described by the distance to agreement (see discussion in Section 5.9).*

5.9 Issues with comparing dose profiles involving sharp dose gradients

In this section, we discuss difficulties in assessing relative and absolute dose differences between results from our calculations (MC and Eclipse MC) and measurements when very low doses and high dose gradients are involved. The absolute difference ADMC(d,x) and the relative difference RDMC(d,x) between MC results and measurements at the coordinate x in the profile at a given depth d in the profile can be defined as

$$\mathrm{ADMC}(d,x) = \left|\mathrm{MeasuredDose}(d,x) - \mathrm{MCdose}(d,x)\right|,$$

and

$$\mathrm{RDMC}(d,x) = \frac{\left|\mathrm{MeasuredDose}(d,x) - \mathrm{MCdose}(d,x)\right|}{\mathrm{MeasuredDose}(d,x)} \times 100,$$

where MeasuredDose(d,x) and MCdose(d,x) denote, respectively, the dose measured and obtained from MC calculations at point x in the profile at depth d. Similarly, the absolute difference ADeMC(d,x) and the relative difference

RDeMC(d,x) between Eclipse MC results and measurements at coordinate x and depth d can be written as

$$\mathrm{ADeMC(d,x)} = \left|\mathrm{MeasuredDose(d,x)} - \mathrm{eMCdose(d,x)}\right|,$$

and

$$\mathrm{RDeMC(d,x)} = \frac{\left|\mathrm{MeasuredDose(d,x)} - \mathrm{eMCdose(d,x)}\right|}{\mathrm{MeasuredDose(d,x)}} \times 100,$$

where eMCdose(d,x) is the dose obtained from Eclipse MC calculations.

One problem with obtaining the above quantities, which allow for an adequate comparison of calculations with measurements, is that the measurement and calculation outputs (i.e., measuredDose(d,x), MCdose(d,x) and eMCdose(d,x)) are not available at the same point x. This problem could be solved by interpolating all outputs at the same point x. However, due to the sharp dose gradients in the outputs, any ordinary interpolation would lead to significant interpolation errors. We rather use spline interpolation here, because the interpolation error can be made very small even when using low degree polynomials for the spline [6]. We have written a cubic spline interpolation program that reads dose profiles at calculated or measured point x_j (j=1,2,3, …,N_{max}, with $x_{min} \le x_j \le x_{max}$), and then calculates the interpolated value at any point x such that $x_{min} \le x \le x_{max}$. Here x_{min} and x_{max} denote the minimum and maximum of the available output data from measurements and calculations. This procedure permits to obtain needed quantities measuredDose(d,x), MCdose(d,x) and eMCdose(d,x) at the same point x.

For the “three-bars bone-bone-bone phantom and for a 9MeV beam, we show in Figure 5.21(b) the relative differences RDMC(d,x) between measurements and MC calculations and RDeMC(d,x) between measurements and MC. These two quantities are given in percentage (%) and since they are obtained by dividing the absolute difference between measurements and calculation by the measured dose at the corresponding point, they can become quite large near low dose area. This clearly appears in Figure 5.21(b) near the minima in the profiles as

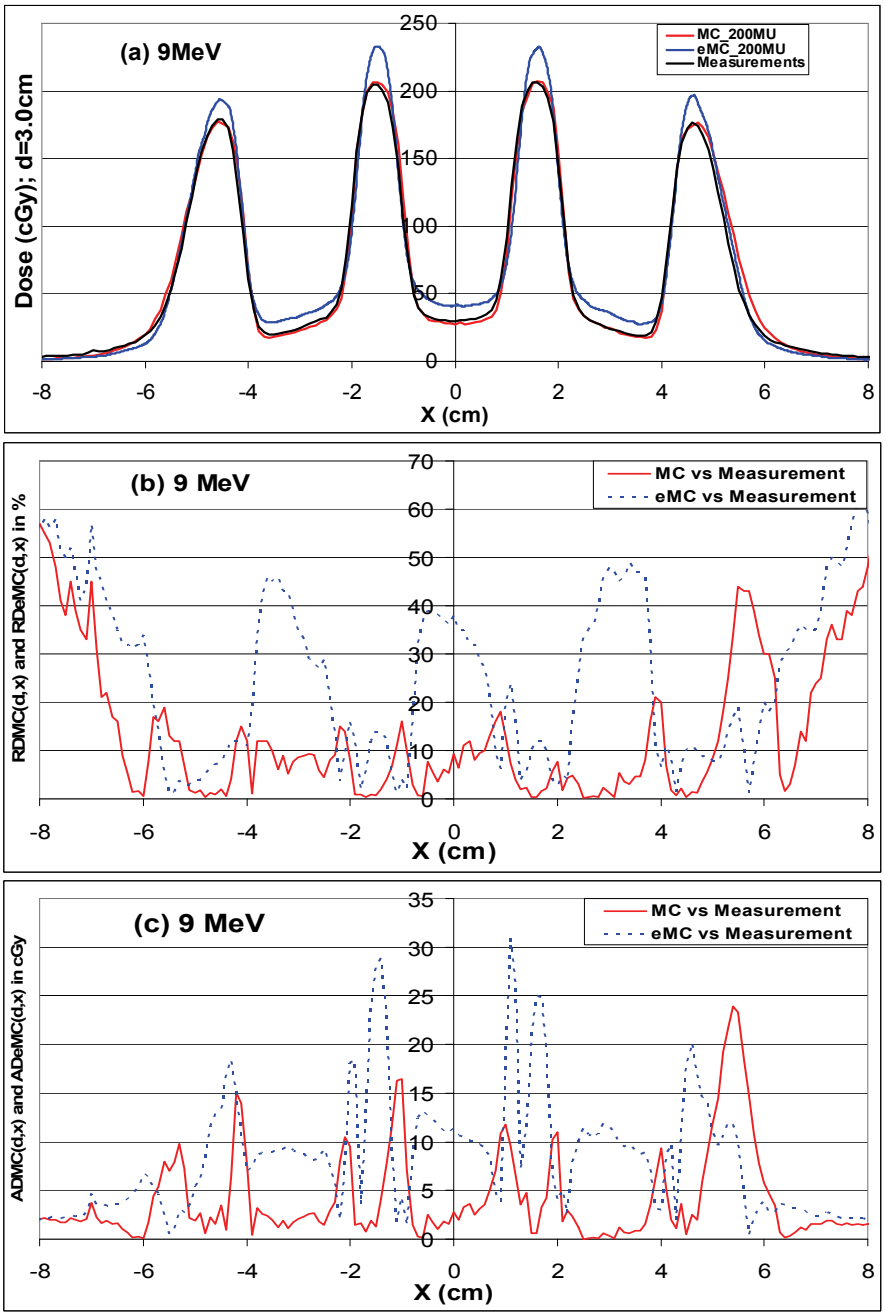

Figure 5.21: ***(a)*** *Dose profile for the "three-bars" bone-bone-bone phantom at depth d=3.0cm for a 9MeV beam already displayed in Figure 5.16.* ***(b)*** *Relative differences RDMC(d,x) between measurements and MC, and RDeMC(d,x) between measurements and Eclipse MC.* ***(c)*** *Absolute differences ADMC(d,x) between measurements and MC, and ADeMC(d,x) between measurements and Eclipse MC.*

well as near the penumbra and umbra of the profile where the relative differences can reach as high as 50%. For such low doses, it would be quite misleading to use relative differences as a tool for assessing the accuracy of calculations, as a small difference between calculations and measurements can translate into very large relative error. In fact, this magnification of the relative difference in the low dose area is not observed in the absolute dose in Figure 5.21(c).

It also follows from Figure 5.21 that in the region where the dose profile exhibits a sharp dose gradient, relative differences in Figure 5.21(b) as well as absolute differences in Figure 5.21(c) increase substantially. This is more noticeable in Figure 5.21(c) for the absolute dose difference than in Figure 5.21(b). This is related to the so-called distance to accuracy. In fact, with such sharp dose gradients, even a small shift in the x-direction of less than 1 mm translates into a large dose difference between measurements and calculations. Distance to accuracy in the x-direction of less than 1 mm is well within acceptable quality assurance standards and in clinical applications [5].

Therefore, the only region in the profile that provides non-equivocal relative differences between calculations and measurements are regions where dose is substantial and where there is no significant dose gradient. Such regions in our profiles are essentially near the peaks of the dose profile. Typical values of percentage differences given throughout this work will correspond to the region near peaks in the dose profile. In this context, relative differences between Eclipse MC and measurements in the case in Figure 5.21 are as high as 13%, whereas relative differences between MC and measurements are about 2% or less.

References

1. Asiev, K., *"Validation of a Monte Carlo Treatment Planning System (TPS) for electron beams"*, Master Thesis, 2006, McGill University.
2. Walters, B., Kawrakow, I., and Rogers, D.W.O., *"DOSXYZnrc users manual"*, Ionizing Radiation Standards, National Research Council of Canada (Ottawa, 2007).
3. Ding, G.X., Duggan, D.M., Coffey, C.W., Shokrani, P., and Cygler, J.E., *"First macro Monte Carlo based commercial dose calculation module for electron beam treatment planning—new issues for clinical consideration"* Phys. Med. Biol., 2006, vol. **51**, p. 2781–2799.
4. Internal Specialty Products, "*Gafchromic© EBT: Self-developing film for radiotherapy dosimetry",* August 2007.
5. Van Dyk, J., et al., *"Commissioning and quality assurance of treatment planning computers"*, Int. J. Radiat. Oncol. Biol. Phys., 1993. vol. 26, p. 261-273.
6. Press, W.H., Teukolski, S.A., Vetterling, W.T., and Flannery B.P., *"Numerical Recipes in Fortran: The Art of Scientific Computing"*, 2nd Edition (Cambridge, 1992)

Chapter 6: Evaluation of Eclipse© using real patient data

6.1 Introduction

Phantoms used in the evaluation of Eclipse© in Chapter 5 consist of slabs of tissue that define heterogeneities with well defined and extremely sharp tissue interfaces. In addition, the bone heterogeneities used are relatively thick compared to common bones in the human body. Therefore, although these phantoms are very useful in providing insight into the efficiency and accuracy of calculation algorithms, they do not accurately reproduce the situation in a real patient, where the interface between bone and soft tissue for example usually has a transitional region consisting of a combination of soft tissue and bone. It follows that phantoms used for evaluating Eclipse© Monte Carlo (MC) in Chapter 5 might overestimate or underestimate the situation in real patients. In this chapter, we attempt to evaluate Eclipse© MC for a real patient case. Since we cannot place a dosimeter inside a patient, and since conventional MC done with DOSXYZnrc© [1] has lead in previous chapters to results in better agreement with measurements, we shall consider MC as the benchmark against which Eclipse© MC is to be compared in this chapter.

This chapter is organized as follows. The patient case under study is presented in Section 6.2. Section 6.3 is devoted to a description of MC and Eclipse© MC dose calculation procedures for the patient. Finally, a comparison of MC and Eclipse© MC results is done in Section 6.4.

6.2 Presentation of the case under study

In our investigation, we consider the case of a patient treated for breast cancer. Figure 6.1 shows a screen capture of few CT slices of the patient on the Eclipse© platform. The physician requires an electron beam irradiation of the mediastinal

region where some nodal structures have to be treated. Since these nodal structures extend close to the patient skin, an electron beam is chosen because it provides a high entrance dose while having a limited penetration at the range of electrons, which protects healthy tissues beyond this range such as the heart.

Figure 6.1: *CT slices of the patient under study: the top left, bottom left and bottom right images show a transversal, frontal and sagittal views of the patient, respectively. The top right image is a beam's eye view that illustrates the field defining cutout inserted in the applicator to define the irradiated region.*

An electron cutout is used to define and restrict the electron beam field in the mediastinal region (see top right panel in Figure 6.1), thereby limiting the dose deposition to healthy tissues beyond the mediastinal region.

6.3 Procedures and methods

The patient structure and geometry is captured in a CT scanning process and images are exported into the Eclipse© treatment planning system. Eclipse© handles the CT Hounsfield units conversion into materials and densities used in for MC calculations. In this process, the calibration curve in Figure 5.4 is used. Thus, Eclipse© MC calculations are straightforward from patient data on the Eclipse© platform.

For MC calculations in DOSXYZnrc© however, CT data processing is usually performed separately using the stand-alone code known as *ctcreate*, because this permits to use larger phantoms without running out of memory [1]. The *ctcreate* code reads CT data and re-samples it to correspond to volume elements where dose will be scored, and converts it into materials and densities for each voxel. The output by *ctcreate* is written into an ASCII file with extension *egsphant*, which contains all the information necessary for DOSXYZnrc© to simulate the CT phantom. However, we do not use *ctcreate* to generate the *egsphant* file needed for our DOSXYZnrc calculation. Instead, the patient CT data is exported in DICOM format from the Eclipse© platform into a Matlab© (The MathWorks, Natick, MA, USA) code known as “BrachyGUI” [2], which is used to converts the CT patient data into an *egsphant* file. This *egsphant* file, combined with an appropriate phase space file for each electron beam energy and cutout is used for MC dose calculations with DOSXYZnrc©.

6.4 Monte Carlo against Eclipse Monte Carlo

In our calculations in Eclipse© we select a reference point in the patient along the central axis of the beam at 1.5 cm depth below the patient surface, and near the center of the cutout at which we deliver a dose of 2 Gy. For comparisons of the

resulting Eclipse© absolute dose with MC results, we scale the latter such that a dose of 2 Gy is delivered at that same point.

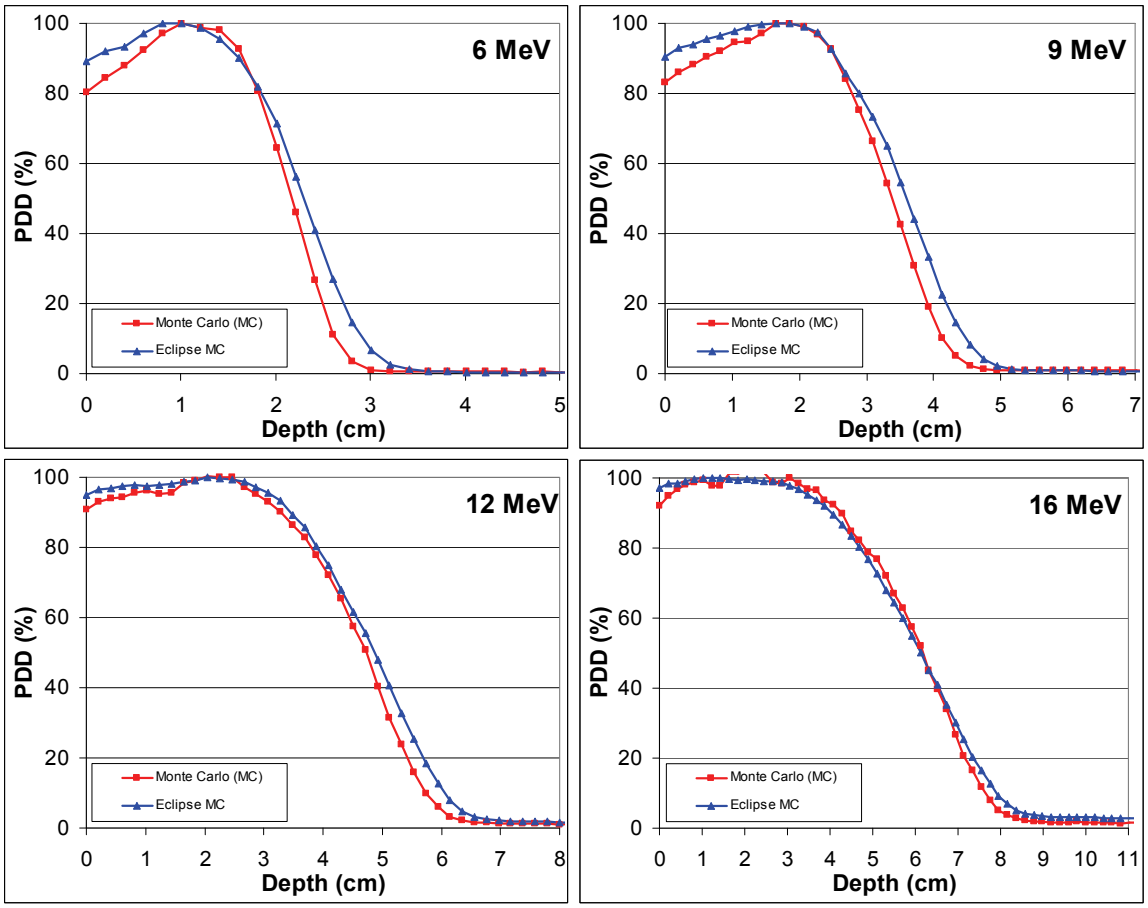

Figure 6.2: *Comparison of percent depth doses (along the central axis of the cutout) for various energies obtained from MC and Eclipse MC calculations in the real patient case.*

Figure 6.2 shows MC and Eclipse MC PDDs in the patient along the central axis of the cutout for various energies. The two methods agree relatively well, especially, for higher energies beams (12-16 MeV). Larger discrepancies between MC and Eclipse MC are found near the patient skin entrance for lower energy beams (about 11% for 6 MeV and 8% for 9 MeV), and near the practical range of the PDD. Similar discrepancies between MC and Eclipse MC, yet with a lower magnitude, have been found in Chapter 5 for PDDs in water phantoms.

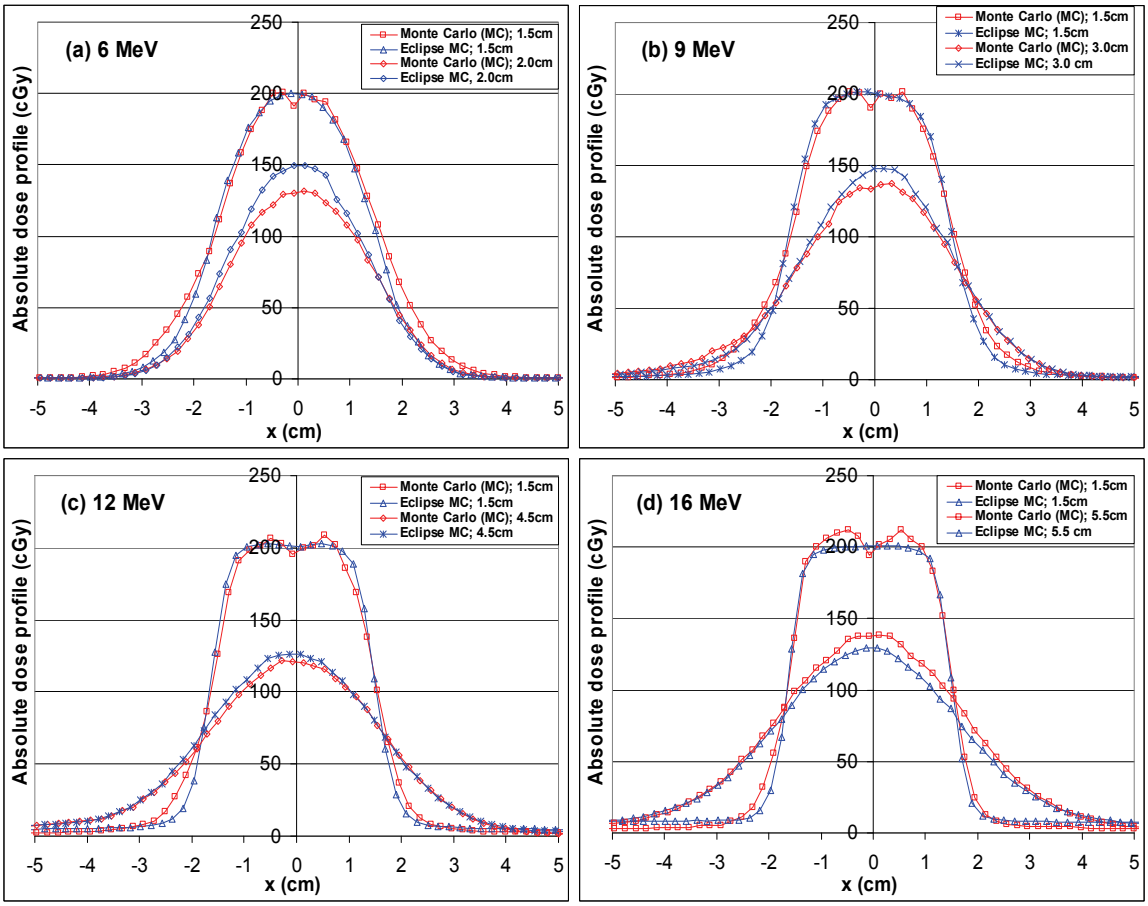

Figure 6.3: *Absolute dose profiles for various beam energies and depths across the cutout in the transversal plane of the patient. Depths are measured along the central axis of the beam from the patient surface. (a) 6 MeV, depths of 1.5 and 2 cm; (b) 9 MeV, depths of 1.5 and 3 cm; (c) 12 Mev, depths of 1.5 and 4.5 cm; (d) 16 MeV, depths of 1.5 and 5.5 cm.*

Dose profiles across the cutout in the transversal plane of the patient body on the CT slice along the central axis of the beam are shown in Figure 6.3 for various electron beam energies. Eclipse© MC Results agree with MC within less that 10%, even at depths as shallow as 5.5 cm. This is slightly better than discrepancies as high as 15% found in the study using physical phantoms in Chapter 5. The reason is the relatively smoother change in heterogeneity densities in the patient as compared to very sharp changes in the physical phantoms.

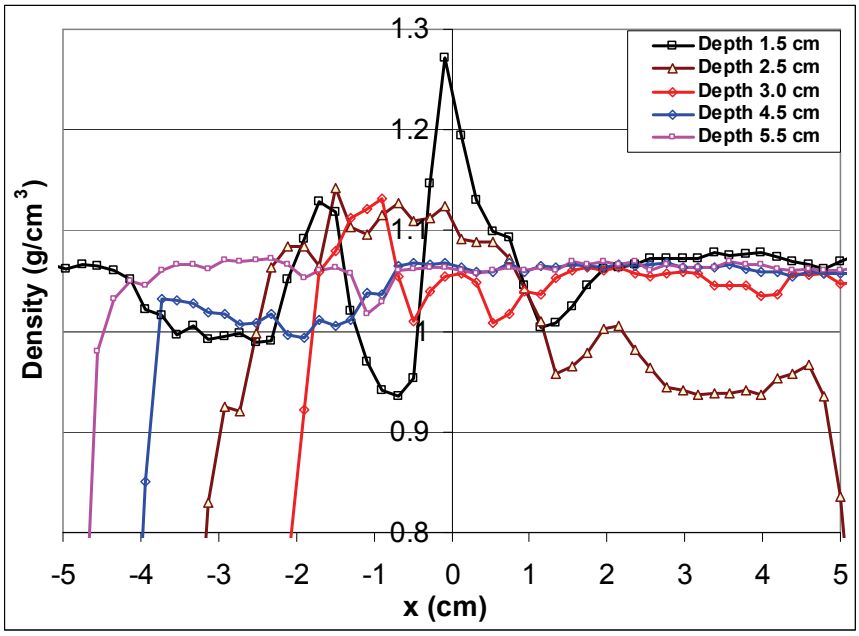

Figure 6.4: *Tissue density profiles across the patient at various depths (considered in Figure 6.3) relative to the patient surface on the beam central axis.*

However, for all energies in Figure 6.3, there is local minimum in the dose profile near the central axis at 1.5 cm depth. This pattern in the dose profiles is similar to our finding in Chapter 5 near high density cortical bone, and is due to the high density bone tissue of the sternum. In other to confirm that, we plot in Figure 6.4 the density profiles at various depths of interest in the patient. One sees that the density profile at depth 1.5 cm shows a sharp increase in the near the beam central axis, in an area that corresponding to the sternum. Eclipse MC however, shows no feature indicating the presence of this relatively sharp density gradient. This, once again, illustrates the difficulty for Eclipse to accurately deal with high density gradients.

In some cases in Figure 6.3 discrepancies between Eclipse© MC and MC found near the penumbra of profiles can be relatively large. Such differences could be the result of the relatively poor reproduction of the cutout in both Eclipse and MC calculations. In fact, in both cases the input of the cutout is not digitized, instead it is entered manually by mouse clicking around a drawing of the cutout on a

paper sheet. This inaccurate reproduction of the cutout is also apparent in the 2D dose profile in Figure 6.5 where dose profile from MC and Eclipse MC are compared for various electron beam energies. Indeed, one sees that away from the center of the cutout, substantial discrepancies exist between results from the two approaches. Note that in routine clinical applications, the cutout is drawn on the Eclipse platform and moulded for treatment delivery.

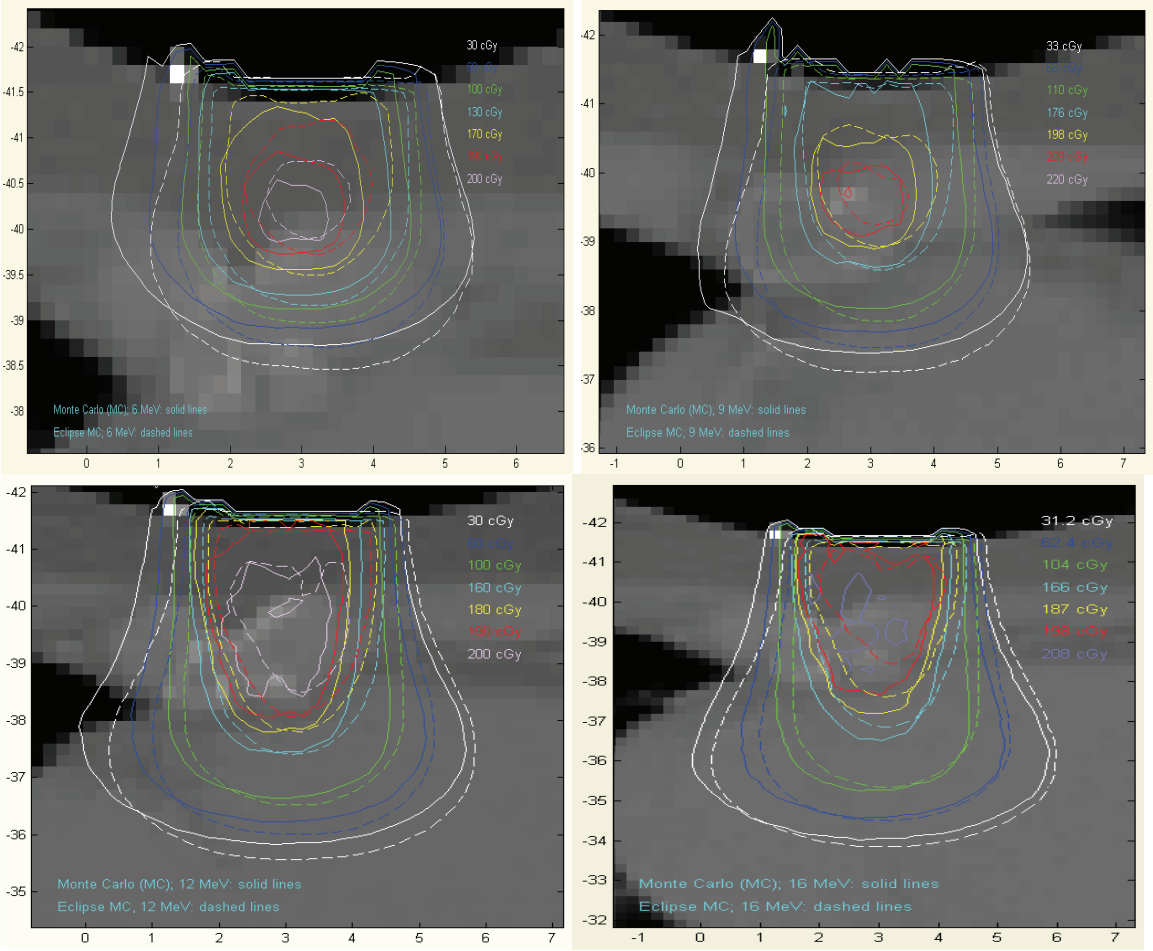

Figure 6.5: *Comparison of isodose distributions from MC (solid lines) and Eclipse MC (dashed lines) calculations for various electron beam energies; 6 MeV (top left plot); 9 MeV (top right plot), 12 MeV (bottom left plot); and 16 MeV (bottom right plot). The vertical labels on the vertical axis are pixel indices and the labels on the horizontal axis are distances in cm.*

References

1. Walters, B., Kawrakow, I., and Rogers, D.W.O., *"DOSXYZnrc users manual"*, Ionizing Radiation Standards, National Research Council of Canada (Ottawa, 2007).
2. Poon, E., Le, Y., Williamson, J.F., Verhaegen, F., *"BrachyGUI: an adjunct to an accelerated Monte Carlo photon transport code for patient-specific brachytherapy dose calculations and analysis"*, J. Phys.: Conf. Ser., 2008, vol. **102**, 012018.

Chapter 7: Summary, conclusions and perspectives

7.1 Summary and conclusions

Increasingly higher standards for patient care combined with more and more complex irradiation procedures and target localization techniques involved in modern radiotherapy require increasingly sophisticated and numerically intensive calculation algorithms that should furthermore be very fast for practical use in the clinic. One of the most important aspects is the need for accurate photon and electron transport algorithms that permit to calculate dose in tissue, which is the first step in any attempt to conform and optimize dose delivery. Monte Carlo (MC) method are the most accurate method for dose calculation in radiotherapy, yet their rigorous implementations are time consuming for routine use in the clinic. This has lead to the development of "fast" implementations of MC methods [1,2,3,4] that use tricks and approximations with the aim of speeding MC calculations while maintaining a clinically acceptable accuracy in dose calculations. For electron beams some of these fast MC methods are now available in commercial treatment planning systems. It is the responsibility of medical physicists to evaluate and commission these software packages prior to their use in the clinic.

In this project, we have performed an evaluation of the electron Monte Carlo (eMC) algorithm of Eclipse© (Varian, Palo Alto, CA) treatment planning system, which is based on a fast MC implementation known as Macro Monte Carlo (MMC) [1]. This evaluation is done using purpose-built phantoms containing heterogeneities by comparing Eclipse© MC results (i.e., percent depth doses and dose profiles) against measurements, and against full MC simulations using DOSXYZnrc© (National Research Council of Canada, Ottawa, ON). We also consider a case of a real patient for this evaluation. A previous evaluation [5] of the eMC algorithm of Eclipse© used dedicated phantoms that were scanned and

imported into Eclipse© for calculations, and relative doses from Eclipse were compared with measurements. The originality of this work comes from several aspects: First we do not scan phantoms used for calculations; instead we digitally reproduce copies of these phantoms on each platform (Eclipse© and DOSXYZnrc©) for calculations. This way, we exclude any uncertainty that could arise from the conversion of CT data into densities used in MC calculations. Second, our evaluation is based on the comparison of absolute dose, which requires extraction of absolute dose from calculations and from measurements. Third, we evaluate Eclipse for a real patient case. Finally, an approach for extracting absolute dose profiles and percent depth doses (PDDs) from EBT Gafchromic© films has been developed.

EBT Gafchromic© films are used for measuring PDDs and dose profiles in phantoms. They are handled and processed using a document scanner, as recommended by the AAPM task Group 55 report [6]. The film processing involves scanning the film and extracting the PDDs and dose profiles based on a protocol described in Ref [7] for EBT Gafchromic© film calibration. Building on this protocol for film calibration, we have developed an approach for extracting PDDs and absolute dose profiles from EBT Gafchromic© film.

Following calculations and measurements using physical phantoms with embedded heterogeneity bars, we have analyzed Eclipse© MC and conventional MC results in comparison with measurements. It follows that, as expected, conventional MC simulations using DOSXYZnrc© lead to results in better agreement with measurements than those from Eclipse©. Discrepancies between MC and measurements are about 5% or less, except in regions where dose is very low or where a high dose gradient exists. Even in regions with a high dose gradient, MC results have a distance to agreement well within the recommended 2 mm [8]. The price paid for the better accuracy in MC results is longer computation time. On the other hand, discrepancies between Eclipse© MC

results and measurements can be as high as 15%, especially for smaller size heterogeneities with substantial density differences with surrounding materials. Larger uncertainties in Eclipse© MC results are found near and under tissue heterogeneities, as already pointed out in Ref. [9]. However, the accuracy achieved by Eclipse© MC is quite remarkable; given that it is many orders of magnitude faster that conventional MC, faster enough to perform calculations within a time scale already practical for clinical use.

Since physical phantoms used have thicker tissue heterogeneities with sometimes sharper changes in density at tissue interfaces than in the human body, we considered a real patient case, with the purpose of probing Eclipse accuracy in a realistic clinical context. Thus, we have compared Eclipse calculations with conventional MC simulations using DOSXYZnrc©. In this case, slightly smaller discrepancies (about 10% or less) are found with MC results. This suggests that Eclipse's largest uncertainties occur near areas with sharp changes in tissue heterogeneities. This could be due to the limited transport step (no less than 0.5 mm) in Eclipse MC, given that near sharp heterogeneities increasingly smaller transport steps are needed to maintain accuracy. However, note that while the Eclipse MC calculation for a real patient takes about 20 to 30 minutes to complete, the MC simulation using DOSXYZnrc© needs more than 10 hours to complete on our computer cluster.

In conclusion, despite relatively large uncertainties in very specific area with high and sharp density gradients, Eclipse MC are fast enough for clinical use and can be very helpful for planning complex treatment setups. However, such a planning must be supplemented by a patient specific quality assurance to verify the calculated doses.

7.2 Perspectives

Our investigation indicates substantial inaccuracies for Eclipse Calculations near sharp tissue heterogeneities. Improving the fast MC implementation in Eclipse could improve the results, but it is beyond the scope of clinical activities. However, the discrepancies found between the measured PDD in water and those calculated in Eclipse indicate that there is room for improvement of the commissioning steps of Eclipse Monte Carlo, at least until a good agreement is found between the two PDDs. In addition, it would be interesting to investigate the influence of inaccuracies in the PDDs on dose calculation with heterogeneities in order to get an idea of what king of accuracy you need in the basic data.

Throughout this project, we used phantoms with a sufficiently broad range of heterogeneities, but focussed on normal electron beam incidences with respect to phantom surface. It would be interesting to extend this work for oblique incidences at various angles. In addition, instead of the standard 10x10 cm^2 cutout with the applicator used in this work, one could combine heterogeneous phantoms used in this work with various irregular cutout shapes to evaluate the Eclipse© electron Monte Carlo algorithm.

One of the special radiotherapy techniques that involve electron beams is electron arc therapy, which is used to treat certain large superficial tumours that follow curved surfaces [10,11]. In this case, the electron beam is moved isocentrically over a stated arc. While the technique is well known and widely accepted as clinically used for certain tumours, it is not widely used because it is relatively complicated and its physical characteristics are poorly understood. This begs for an evaluation of Eclipse© for arc therapy treatments. If proven accurate enough, Eclipse treatment planning has the potential to make electron arc therapy planning and delivery easier in the clinic.

References

1. Neuenschwander, H., Mackie, T.R., and Reckwerdt, P.J., *"MMC: a high performance Monte Carlo code for electron beam treatment planning"*, Phys. Med. Biol. 1995, **vol. 40, p**543–574.
2. Keall, P.J. and Hoban, P.W., *"Super-Monte Carlo: a 3D electron beam dose calculation algorithm"*, Med. Phys., 1996, **vol. 23**, p2023–2034.
3. Kawrakow, I., Fippel, M., and Friedrich, K., *"3D electron dose calculation using a voxel based Monte Carlo algorithm (VMC)"*, Med. Phys., 1996, **vol. 23**, p445–457.
4. Ma, C.M., et al., *"A Monte Carlo dose calculation tool for radiotherapy treatment planning"*, Phys. Med. Biol., 2002, **vol 47**, p1671-1689.
5. Ding, G.X., Duggan, D.M., Coffey, C.W., Shokrani, P., and Cygler, J.E., *"First macro Monte Carlo based commercial dose calculation module for electron beam treatment planning—new issues for clinical consideration"* Phys. Med. Biol., 2006, vol. **51**, p. 2781–2799.
6. Niroomand-Rad, A., et al, *"Radiochromic film dosimetry: Recommendations of AAPM Radiation Therapy Committee Task Group 55",* Med. Phys., 1998, **vol. 25**, p. 2093-2115.
7. Devic, S., et al, *"Precise radiochromic film dosimetry using a flat-bed document scanner",* Med. Phys., 2005, **vol. 32**, p. 2245-2253.
8. Van Dyk, J., et al., *"Commissioning and quality assurance of treatment planning computers"*, Int. J. Radiat. Oncol. Biol. Phys., 1993. vol. 26, p. 261-273.
9. Ding, G.X., Duggan, D.M., Coffey, C.W., Shokrani, P., and Cygler, J.E., *"First macro Monte Carlo based commercial dose calculation module for electron beam treatment planning—new issues for clinical consideration"* Phys. Med. Biol., 2006, vol. **51**, p. 2781–2799.

10. Pla, M., Podgorsak, E.B., Pla, C, Freemann, C.R., *"Determination of secondary collimator shape in electron arc therapy"*, Phys. Med. Biol., 1993, vol. 38, p. 999-1006.
11. Angelis, C.D., et al., *"Electron arc therapy treatment planning verification with alanine/EPR dosimetry"*, Applied Radiation and Isotopes, 2000, vol. 52, p. 1203-1207.

Appendix A

The protocol that we developed for the extraction of dose profile and PDDs from Gafchromic© EBT films involves taking three scans of the unexposed film strip and three scans of the expose film strip (see Chapter 4), with the resulting six files saved in TIF file format. In this section, we describe a code written in MatLab© and used in the first step of the determination of dose profiles from the TIF files. In this first step the three TIF files for unexposed (resp. exposed) film strips are read, averaged and a Wiener filter is applied. The code is named "PROFILE_STEP1" and is illustrated below, where each MatLab© instruction is preceded or followed by a comment in italics that describes what the instruction does.

PROFILE_STEP1

```
% Reads the UNEXPOSED images for different number of successive scans
a1=imread('unexp_P1.tif');                % Reads the 1st unexposed film image
b1=double(a1(:,:,1));
a2=imread('unexp_P2.tif');                % Reads the 2nd unexposed film image
b2=double(a2(:,:,1));
a3=imread('unexp_P3.tif');                % Reads the 3rd unexposed film image
b3=double(a3(:,:,1));

% Computes the mean of the three UNEXPOSED images and takes their Wiener filter
Im_unexp=(b1+b2+b3)/3;
Im_unexp=wiener2(Im_unexp, [5,5]);

%  m_unexp ===> vertical size, n_unexp ===> horizontal size
[m_unexp n_unexp]=size(Im_unexp)

clear b*;
clear a*;

% Reads the EXPOSED images for different number of succesive scans
a1=imread('exp_P80_001.tif');             % Reads the 1st exposed film image
b1=double(a1(:,:,1));
a2=imread('exp_P80_002.tif');             % Reads the 2nd exposed film image
b2=double(a2(:,:,1));
a3=imread('exp_P80_003.tif');             % Reads the 3rd exposed film image
b3=double(a3(:,:,1));
```

```
% Computes the mean of the three unexposed images and takes their Wiener filter
 Im_exp=(b1+b2+b3)/3;
Im_exp=wiener2(Im_exp, [5,5]);

%  m_exp ===> vertical size(lines),  n_exp ===> horizontal size (columns)
[m_exp n_exp]=size(Im_exp)

clear b*;
clear a*;
```

Appendix B

In this appendix, we present the code “PROFILE_STEP2”, also written in MatLab©, which reads the averaged images resulting from the code “PROFILE_STEP1” and calculates the dose profile along a specified direction.

PROFILE_STEP2

```
% First shrinks the averaged exposed film image because it was scanned in full.

Im1_exp=Im_exp(1:1270,454:645);          % Narrows the area around the exposed film
[m_exp n_exp]=size(Im1_exp);
Im1_unexp=Im_unexp(1:1270,454:645);      % Narrows the area around the unexposed film
[m_unexp n_unexp]=size(Im1_unexp) ;

% Displays the narrowed film image
imagesc(Im1_exp);
axis image;


% Now tries to localize the marked area on the film giving coordinates of the Linac  crosshair.
% Click once on the horizontal mark on the film and press "ENTER"
 [xcc,ycc,zcc]=impixel;
ycc_ref=ycc
% Click once on the vertictal mark on the film and press "ENTER"
[xcc,ycc,zcc]=impixel;   % Click once on the vertical mark on the film and press "ENTER"
xcc_ref=xcc

% Opens the output file “profile.txt” in which calculations results are saved.
fid=fopen('profile.txt', 'wt');
fprintf(fid,' \n')
fprintf(fid,'   x (cm)      x (mm)   Optical dens.  St. dev. in OD \n')
fprintf(fid,'   ~~~~~~     ~~~~~~   ~~~~~~~~~~~~~  ~~~~~~~~~~~~~~~ \n')

clear roi_unexp*
clear roi_exp*

pxl_dark=250;                    % Dark signal
std_pxl_dark=2.2;                % Standard deviation in the dark signal


% The film is divided into 221 voxels, each of size 5x5 pixels (1mm x 1mm). The central
% voxel (Linac crosshair) extends along x-axis from xcc_ref-2 to xcc_ref+2; and along the
```

```
% y-axis from ycc_ref-2 to ycc_ref+2, for a total 5x5 pixels. There are 110 voxels on the under
% and 110 voxels on the above of the central voxel.

ii=0;
yref_under=ycc_ref+2            % Lower border of the central voxel
for i=-110:110                  % each integer unit corresponds to a mm or nbpxl_mm pixels.
   ii=ii+1;
   yvoxel_under=yref_under-i*5;          % pixel size of each voxel is 5
   yvoxel_abov=yvoxel_under-4;           % pixel size of each voxel is 5

% USE NEXT TWO LINE FOR READING OD OVER 1mm x 1mm AREA ON FILM
   roi_unexp=Im1_unexp(yvoxel_abov:yvoxel_under,xcc_ref-2:xcc_ref+2);
   roi_exp=Im1_exp(yvoxel_abov:yvoxel_under,xcc_ref-2:xcc_ref+2);

% USE NEXT TWO LINE FOR READING OD OVER 5mm x 5mm AREA ON FILM
%   roi_unexp=Im1_unexp(yvoxel_abov:yvoxel_under,xcc_ref-12:xcc_ref+12);
%   roi_exp=Im1_exp(yvoxel_abov:yvoxel_under,xcc_ref-12:xcc_ref+12);

% USE NEXT TWO LINE FOR READING OD OVER 10mm x 10mm AREA ON FILM
%   roi_unexp=Im1_unexp(yvoxel_abov:yvoxel_under,xcc_ref-24:xcc_ref+25);
%   roi_exp=Im1_exp(yvoxel_abov:yvoxel_under,xcc_ref-24:xcc_ref+25);

   x(ii)=i;                             % coordinate of the profile
   pxl_unexp=mean2(roi_unexp);          % Transmission scanner reading for UNEXPOSED
   std_pxl_unexp=std2(roi_unexp);       % Standard deviation in the UNEXPOSED transmision
   pxl_exp=mean2(roi_exp);              % Transmission scanner reading for EXPOSED film
   std_pxl_exp=std2(roi_exp);           % Standard deviation in the UNEXPOSED transmision
   od(ii)=log10((pxl_unexp-pxl_dark)/(pxl_exp-pxl_dark));
   c1=( std_pxl_unexp^2+std_pxl_dark^2 )/( (pxl_unexp-pxl_dark)^2 );
   c2=( std_pxl_exp^2+std_pxl_dark^2 )/( (pxl_exp-pxl_dark)^2 );
   std_od(ii)=realsqrt(c1+c2)/log(10);
   x(ii),od(ii),std_od(ii),dose,std_dose);
   fprintf(fid, '%10.3E %10.3E  %11.4E    %11.4E \n', x(ii)/10.0, x(ii),od(ii),std_od(ii));
end

fclose(fid)
```